INTEGRATED OPTICAL-FREQUENCY MIXERS

A DISSERTATION
SUBMITTED TO THE DEPARTMENT OF APPLIED PHYSICS
AND THE COMMITTEE ON GRADUATE STUDIES
OF STANFORD UNIVERSITY
IN PARTIAL FULFILLMENT OF THE REQUIREMENTS
FOR THE DEGREE OF
DOCTOR OF PHILOSOPHY

Jonathan R. Kurz
November 2003

I certify that I have read this dissertation and that in my opinion it is fully adequate, in scope and quality, as a dissertation for the degree of Doctor of Philosophy.

Martin M. Fejer
(Principal Adviser)

I certify that I have read this dissertation and that in my opinion it is fully adequate, in scope and quality, as a dissertation for the degree of Doctor of Philosophy.

Robert L. Byer

I certify that I have read this dissertation and that in my opinion it is fully adequate, in scope and quality, as a dissertation for the degree of Doctor of Philosophy.

David A. B. Miller

Approved for the University Committee on Graduate Studies:

Abstract

Optical frequency (OF) mixers based on periodically poled lithium niobate (PPLN) waveguides are among the most efficient nonlinear optical devices available today. An attractive technology for communications applications, OF mixers have been used to demonstrate many important all-optical signal-processing functions including wavelength conversion, dispersion compensation by spectral inversion, and 160 Gbit/s optical time-division multiplexing.

Integrated-optic structures extend the functionality of OF mixers even further. This thesis develops a useful new set of components compatible with PPLN waveguides that includes couplers, small radius bends, mode sorters, and asymmetric quasi-phasematching (QPM) gratings. These components are used to demonstrate two novel solutions to a recurring problem for nonlinear optical devices: how to distinguish and spatially separate the interacting waves. Integrated OF mixers can separate the output waves from the residual input waves either through a waveguide interferometer or by multiplexing modes. This separation enables bi-directional wavelength conversion, or spectral inversion without offset.

The advanced fabrication techniques developed for integrated OF mixers also enable a new type of bulk nonlinear optical device based on fine transverse patterning of QPM gratings. Control over the spatial amplitude and phase of the nonlinear output leads to a variety of familiar effects from physical optics. These include diffraction from grating "slits," beam steering, and focusing of the nonlinear output through a QPM lens.

Acknowledgements

A great deal of good fortune and help from other people are needed to complete a dissertation; I have had more than my fair share of both. In training to become a scientist, one could not hope for a better role model than my advisor, Professor Martin M. Fejer. His abiding interest in solving problems, combined with his beautifully clear and precise analyses, never fails to show the way forward through challenging projects. I am grateful for the high standards he sets for the research group, and for the freedom I have had in choosing new research directions. I would like to thank Professors Robert L. Byer and David A. B. Miller for their careful reading of this thesis, and for the valuable interactions we have had inside and outside of classes. I am also indebted to the Stanford Graduate Fellowships program for full support during my first three years of graduate work.

The greatest strength of the Byer-Fejer group is its ability to attract excellent researchers. Without the support and enthusiasm of Eric Gustafson and Roger Route during my first project (an interferometer for measuring "creep" in wires), I might have ended up elsewhere. I was fortunate to learn the arts of PPLN waveguide fabrication and testing from Krishnan Parameswaran, an incredibly generous and patient teacher. The vast improvements to the waveguide fabrication model made by Rostislav Roussev and Xiuping Xie have been essential to this thesis. David Hum and Andrew Schober helped measure and analyze many of the QPM physical optics devices, while Takashi Saida and Jie Huang aided in the design and testing of several mode multiplexing devices. Many other Byer-Fejer group students, post-docs, and visiting scientists have contributed to my research and education over the past six years; I hope that I have managed to contribute to some of their successes as well.

In fabricating devices, I have depended on Timothy Brand in the Ginzton Crystal Shop for dicing and polishing, and on Thomas Carver from the Ginzton Microfabrication Lab for SiO_2 deposition. Paul Jerabek and Mahnaz Mansourpour from the Stanford Nanofabrication Facility have kept me supplied with masks and lithography tools. I could not have constructed several pieces of equipment without help from Lawrence Randall and Karlheinz Merkle from the Ginzton and Varian machine shops. Kellie Koucky, Tamara Reynolds, and Vivian Drew have held the Byer-Fejer group together over the years, while it has always been a pleasure to visit the Applied Physics Department because of Paula Perron and Claire Nicholas.

Despite being on the East Coast, my parents and sister have supported me in every possible way throughout my graduate career. They never doubted the value of a doctoral degree, or that I would be able to complete mine; I dedicate this work to them. Finally, I wish to thank Sonya Elder for being my foundation and inspiration during these last few months.

Contents

List of Tables

List of Figures

Chapter 1

Introduction

1.1 Overview

Optical-frequency (OF) mixers based on periodically-poled-lithium-niobate (PPLN) waveguides have made remarkable advances during their first fifteen years of development. Techniques for forming quasi-phasematching gratings and combining them with low-loss waveguides have matured and spread to other ferroelectric oxides. Frequency conversion efficiencies have risen by more than a factor of 10^4 since the initial demonstrations of blue and green light generation [2, 3]. The normalized efficiencies of state-of-the-art OF mixers now exceed 3000%/W, or 100%/W·cm^2, making them some of the most efficient nonlinear optical devices available today [4].

The variety of applications of OF mixers has also increased. While blue light generation is still important [5], PPLN waveguides now provide coherent sources ranging from the ultraviolet [6] through the mid-infrared [7, 8]. Recent work has focused heavily on developing signal-processing devices for optical communications [9, 10, 11]. As described in the following section, OF mixers can serve as wavelength converters, spectral inverters, or gated mixers for wavelength and time-division multiplexed systems. Outside of optical communications, OF mixers are widely applied to studies in spectroscopy [12], fundamental nonlinear optics [13, 14, 15, 16, 17], ultrafast optics [18, 19, 20], and quantum optics [21, 22]. Interest in OF mixers has been sustained by dozens of research groups around the world, and by a number of small and large

companies.

Integrated OF mixers represent the next generation of PPLN waveguide devices. New optical signal-processing applications require more complexity and sophistication, along with high efficiency. Integrated-optic structures extend the functionality of OF mixers, making it possible to manipulate signals with greater flexibility, speed, and dexterity. While this work focuses on devices for optical fiber communications, integrated OF mixers will benefit other applications, as well.

This dissertation develops a toolbox of new components for PPLN waveguides, and demonstrates their use in several types of novel mixers. As described in this chapter, integrated OF mixers build upon mature technology that already produces extremely versatile devices. Section 1.3 introduces an important problem: how to distinguish and spatially separate the interacting waves. Two different OF mixer solutions are presented in Chapters 4 and 5.

Chapter 2 of this dissertation reviews the basic theory of quasi-phasematched (QPM) waveguide interactions. Chapter 3 details how the fabrication of integrated OF mixers has led to a more precise and reproducible process. In Chapter 4, newly developed designs for directional couplers, small-radius bends, and Y-junctions are combined into integrated OF mixers based on interferometer structures. A novel set OF mixers that manipulate higher-order waveguide modes is presented in Chapter 5. Integrated OF mixer fabrication techniques have also led to interesting bulk devices that can manipulate the spatial amplitude and phase of the nonlinear output; these "QPM Physical Optics" devices are described in Chapter 6. Finally, Chapter 7 concludes this dissertation.

1.2 Standard OF Mixers

Optical-frequency mixers are the optical analogue of the radio-frequency (RF) mixers commonly used in electronics. RF mixers enable useful functions such as heterodyne detection or modulation by mixing a (weak) voltage signal with a stronger local oscillator to produce a frequency-shifted output (Figure 1.1). OF mixers perform these same functions on signals from lasers, which might represent data in an optical

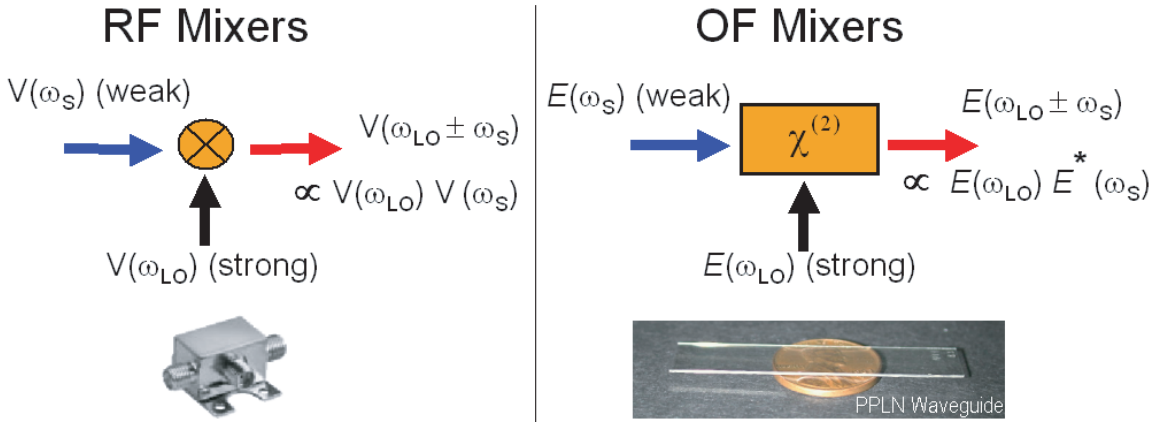

Figure 1.1: The analogy between RF and OF mixers.

communications system. OF mixers produce a frequency-shifted output proportional to the product of the input electric fields. In OF mixers, phase conjugation of the input signal is built into the mixing process.

Whereas RF mixers rely on the strong nonlinearities available from diodes and transistors, OF mixers such as PPLN waveguides are based on the second-order nonlinear susceptibility $\chi^{(2)}$. The linear susceptibility $\chi^{(1)}$ is responsible for a material's refractive index, while higher-order susceptibility terms correspond to a nonlinear polarization response:

$$P_{NL} = \chi^{(2)} E_1 E_2 + \chi^{(3)} E_1 E_2 E_3 + \ldots \tag{1.1}$$

Three-wave mixing devices such as OF mixers use the second-order nonlinearity to produce outputs at the sum or difference frequency of the inputs E_1 and E_2. Since optical nonlinearities are relatively weak compared to electronic nonlinearities, efficient OF mixing requires distributed mixers with interaction lengths much longer than the wavelengths involved.

Accumulating mixer output efficiently over such a long interaction length entails a method of phasematching the interacting waves. The relative phases of the interacting waves usually vary with propagation distance z because dispersion creates a mismatch between their propagation constants: $\Delta k' = k_3 - k_2 - k_1$. Each time the

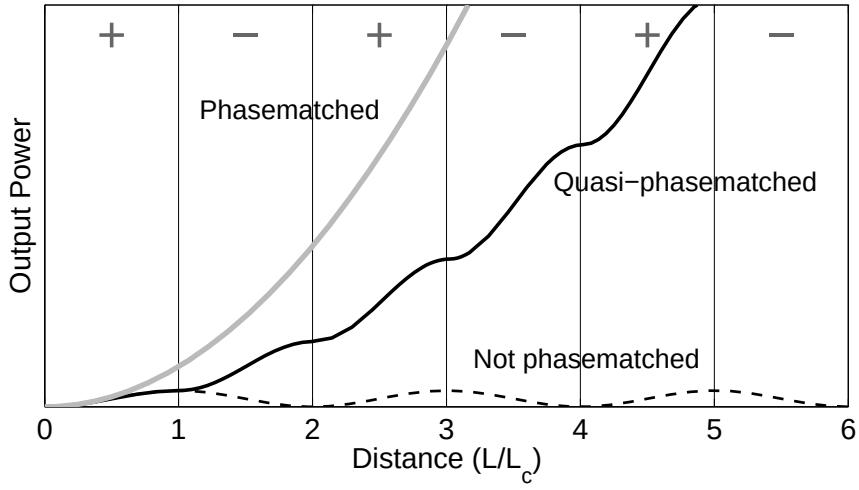

Figure 1.2: OF mixer output versus propagation distance showing three cases: phase velocity mismatch, phasematching, and quasi-phasematching. The plus and minus signs correspond to the nonlinear coefficient.

relative phase $\Delta k' z$ increases by π, the direction of energy flow reverses, limiting the maximum useful interaction length to $L_c = \pi/\Delta k'$, or one coherence length. Without phasematching, the mixer output generated over one coherence length converts back to the input wavelengths during the next coherence length, as depicted in the dashed curve in Figure 1.2. If the interacting waves are perfectly phasematched (gray solid curve), however, the mixer output simply grows with propagation distance. Quasi-phasematching (QPM) compensates for phase mismatch by changing the sign of the nonlinear coefficient every coherence length (black solid curve). This periodic reversal preserves the direction of energy flow from the input waves to the output waves, ensuring that the mixer output increases monotonically with propagation distance [23, 24, 25].

QPM gratings multiply the effective interaction length L in OF mixers by 10^3 or more, since a typical grating period $\Lambda_g = 2L_c$ is 15 μm and QPM gratings in PPLN can be many centimeters long. Long interaction lengths are vital to OF mixers, as their efficiency generally scales with L^2 (or L^4 in the case of cascaded three-wave mixers). Waveguides also play an important role in this efficiency scaling by maintaining

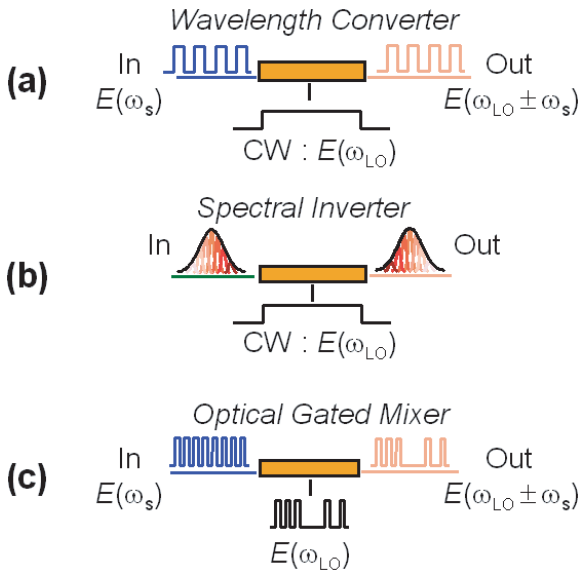

Figure 1.3: Modes of operation for OF mixers.

tight confinement of the optical fields over the entire interaction region. Waveguides typically improve mixing efficiency by two or three orders of magnitude over bulk interactions with tightly focused beams. OF mixers based on PPLN waveguides operate with 1.5-μm pump powers on the order of 100 mW, an amount readily available from erbium-doped fiber amplifiers.

In addition to high efficiency, standard OF mixers have many other attractive properties for communications applications. These include high speed ($>$ 1 THz of modulation bandwidth), large wavelength conversion bandwidths ($>$ 70 nm), large dynamic range and linear response (tested to $>$ 50 dB), and negligible spontaneous emission (parametric fluorescence) noise. These features have led to many demonstrations of all-optical signal-processing functions. Figure 1.3 arranges these functions into three general categories. Depending on its inputs, the same OF mixer device can be used either as a wavelength converter, a spectral inverter, or a gated mixer.

With a continuous-wave (CW) local oscillator, an OF mixer produces a wavelength-shifted replica of the input signal (Figure 1.3a). This device can be used to shift wavelength-division multiplexed (WDM) signals within the 1550-nm-band [26, 27, 28],

or to convert signals between the 1.3-μm and 1.5-μm communications bands [29, 30]. Multiple channels can be converted simultaneously with equal efficiency [31]. OF mixers are transparent to data format, can up- and down-convert with equal efficiencies, and have been tested at speeds up to 160 Gbit/s [32]. In a recent system demonstration, 103 channels of 10 Gbit/s signals spaced by 25 GHz were converted from the C to L communication bands with good performance [33].

OF mixers can also be used as mid-span spectral inverters to compensate for dispersion in communications links [34]. Group velocity dispersion can cause short optical pulses travelling through a fiber span to broaden so much that they overlap in time, degrading the signal quality. The phase conjugation property of an OF mixer (Figure 1.3b) can reverse the chirp of a pulse at the midpoint of a span, converting wavelengths with a slower group velocity to wavelengths with a faster group velocity, and vice-versa. This inversion allows the delayed spectral components to catch up in a second half of the fiber span, recompressing the pulses and recovering the original signal quality. Similar schemes have used the phase conjugation property of OF mixers to compensate for third-order optical nonlinearities (such as self- and cross-phase modulation) in fiber links [35].

Finally, OF mixers can perform many optical signal processing functions as gated mixers (Figure 1.3c). These functions use a pulsed local oscillator, and depend on the mixer output being the product of the inputs. Gated mixers can be used as cross-correlators for optical sampling systems [36] or in phase-locked loops. With a high speed optical clock as the local oscillator, gated OF mixers have been used in 160 Gbit/s time-division multiplexing (TDM) [1]. More complex TDM functions such as time-slot interchange [37] and all-optical header recognition [38] have also been demonstrated. Related applications based upon sum-frequency mixing instead of difference-frequency mixing in OF mixers include optical switching, and matched filtering for code-division multiple access [39].

Cascaded $\chi^{(2)}$ interactions have become the preferred mixing scheme for OF mixers in most communications applications. In cascaded $\chi^{(2)}$ mixing (sometimes denoted by $\chi^{(2)} : \chi^{(2)}$), two three-wave mixing processes happen simultaneously or in succession, mimicking a four-wave mixing process [40, 41]. The effective $\chi^{(3)}$ achieved in this way

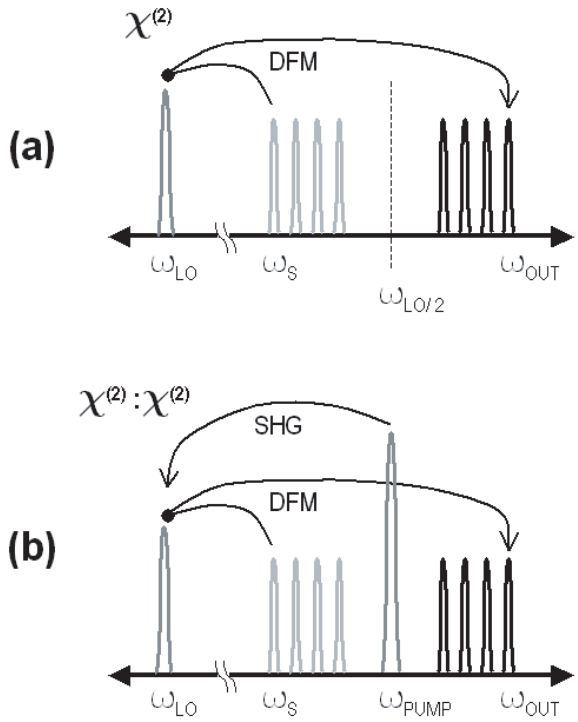

Figure 1.4: Intra-band wavelength conversion of four signals by $\chi^{(2)}$ and cascaded $\chi^{(2)}$ mixing (a and b). Input signals and pump are shown in gray, while the wavelength-shifted output is black.

using PPLN is 10^4 to 10^5 times higher than that of silica glass. Figure 1.4 illustrates schematically how either one or two $\chi^{(2)}$ interactions can be used in communications-band wavelength conversion by difference-frequency mixing (DFM). In Figure 1.4a, DFM between 1550-nm-band signals (ω_s) with a strong local oscillator at 775 nm (ω_{LO}) produces wavelength-converted output signals ($\omega_{OUT} = \omega_{LO} - \omega_s$) that are mirrored about the 1550-nm point ($\omega_{LO}/2$). In the cascaded scheme shown in Figure 1.4b, second-harmonic generation (SHG) of a strong pump at 1550 nm produces the 775-nm local oscillator for DFM, yielding the same output signals. In current devices, 0-dB wavelength conversion is possible with approximately 30 mW of 775-nm pump power, or 100 mW of 1550-nm pump power; with more pump power, conversion gain is possible.

The major advantage of the cascaded scheme over a single three-wave mixing process lies in the use of a 1550-nm pump. The output power, reliability, and availability of 1550-nm wavelength lasers and amplifiers have increased greatly over the past decade, while their cost has dropped somewhat. 1550-nm-band pump and signals eliminate the difficulties encountered in simultaneously launching a signal and local oscillator at vastly different wavelengths (since ω_{LO} is generated inside the device). With standard components, pump and signals can be combined in fiber and launched together; standard OF mixers have adiabatically tapered inputs and outputs that are mode matched for single-mode fiber coupling.

1.3 Integrated OF Mixers

All of the various functions described in Section 1.2 are based upon standard OF mixers, in which the nonlinear mixing occurs in a single, straight waveguide. Adding parallel mixing sections or interconnecting multiple waveguides using integrated-optic structures can extend the functionality of OF mixers. If the standard OF mixer is analogous to a single optical diode, integrated OF mixers form simple optical circuits with multiple diodes. A variety of useful new circuits can be fabricated using basic components such as directional couplers, Y-junctions, and small radius bends. More specialized tools for integrated OF mixers include asymmetric QPM gratings and

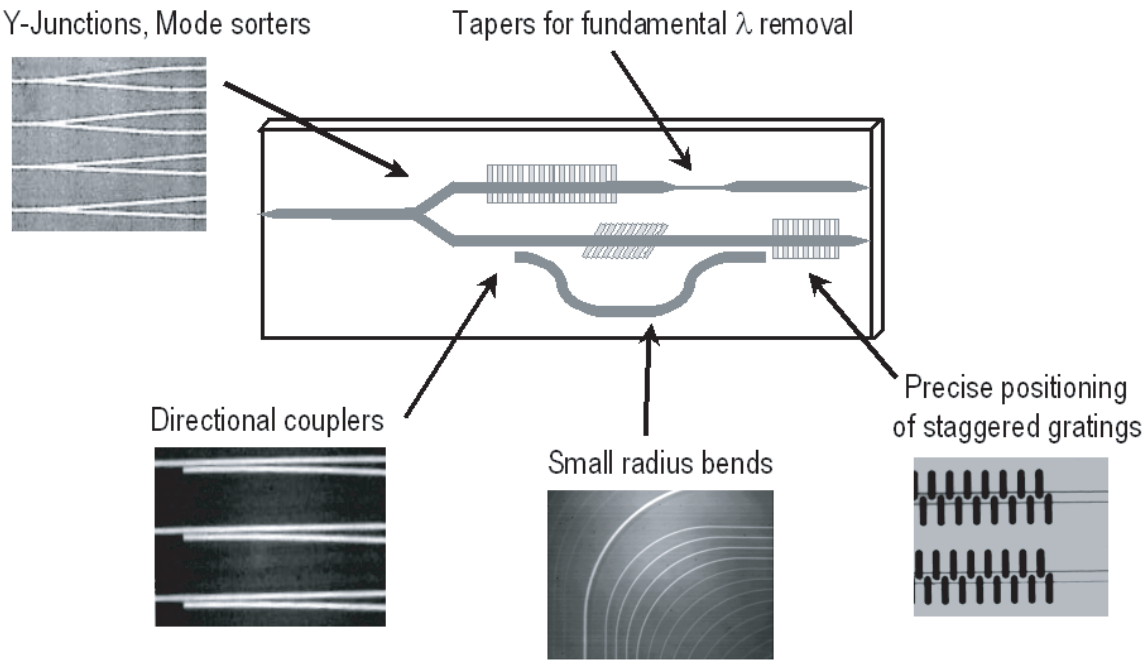

Figure 1.5: Schematic integrated OF mixer, including micrographs of fabricated components.

mode sorters. Examples of some of these structures, along with micrographs of actual components, are shown in the schematic device in Figure 1.5. Chapters 4 and 5 describe the development and use of these components in novel mixer devices.

Although integrated optical components have had over two decades of development in lithium niobate waveguides [42], they still present new challenges for PPLN OF mixers, which are optimized primarily for nonlinear optical performance. New components must be compatible with existing designs for high efficiency OF mixers, which constrain several of the processing parameters. Some integrated OF mixers require improved techniques for fine transverse patterning of QPM gratings, and for precise alignment of these structures to waveguides. Chapter 3 describes the challenges of fabricating increasingly complex devices.

There are already some examples of OF mixer integration. Directional couplers have been used in interferometers with intensity-dependent switching [43], as wavelength filters in integrated squeezing devices [44], and as wavelength combiners for

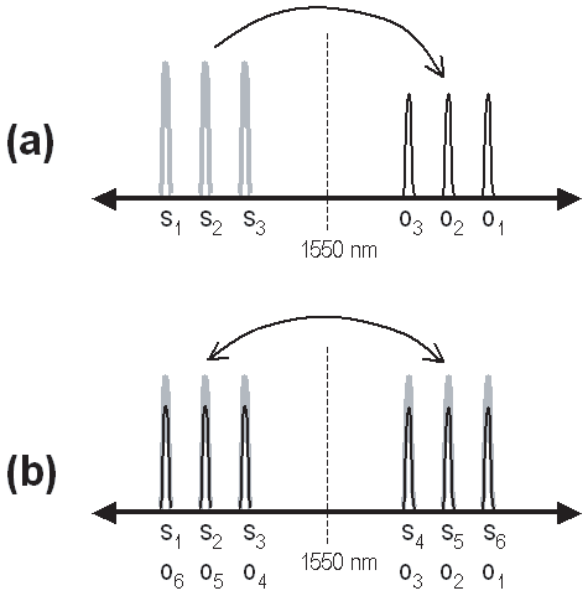

Figure 1.6: Standard 1550-nm-band wavelength conversion (a) and bi-directional wavelength conversion (b) with input signals s and outputs o. In (b), the inputs and outputs have the same wavelengths, making them impossible to distinguish or spatially separate in a single-mode device.

difference-frequency mixers [45]. QPM mixing stages for SHG and cascaded DFM have been combined with Er:$LiNbO_3$ waveguide lasers [46, 47]. Thermo-optic switches have also been incorporated in QPM mixers as phase-shifters [48]. This dissertation establishes a variety of new passive components for integrated OF mixers, with a focus on solving the problem of distinguishability.

1.4 Distinguishability and Spatial Separation

Distinguishing and spatially separating the interacting waves in nonlinear optical devices can be difficult. A particularly difficult case is difference-frequency mixing (DFM) or parametric amplification in which the signal and idler wavelengths are degenerate (identical), or nearly degenerate. This problem affects standard OF mixers in all three operational modes.

In standard wavelength converters (Figure 1.6a), several input channels (s_1, s_2, s_3)

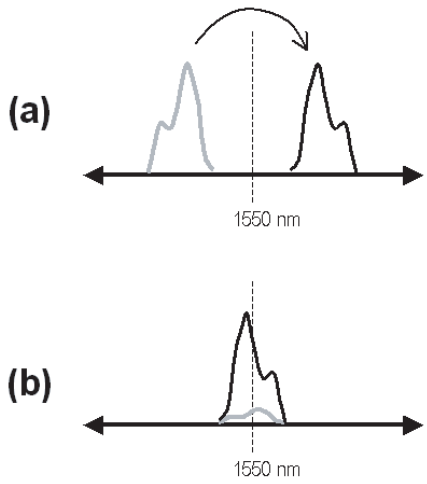

Figure 1.7: Spectral inversion with and without offset. In standard OF mixers, a frequency offset prevents input and output spectra (gray and black) from overlapping and interfering (a). This offset is unnecessary in integrated OF mixers that prevent cross-talk by attenuating the residual input relative to the mixer output (b).

mix with a 775-nm local oscillator to produce output channels shifted across the 1550-nm-band (o_1, o_2, o_3). These output channels can be filtered from the input channels using a bandpass filter that separates wavelengths above and below 1550 nm. Problems arise in bi-directional wavelength conversion (Figure 1.6b), which interchanges input channels on both sides of the 1550-nm-band. Here the input and output channels (shown in gray and black) have the same wavelengths. It would be difficult to distinguish, let alone spatially separate the outputs from the residual inputs in this case. Consequently, standard OF mixers tend to operate at half of their total spectral capacity, since each wavelength channel must be designated exclusively as input or output to eliminate interference.

The problem of distinguishing and spatially separating the mixer output from the residual input places similar limitations on standard spectral inverters and gated OF mixers. In standard spectral inverter devices, the input and output spectra must be offset in frequency to avoid overlap and interference (Figure 1.7a). Mid-span spectral inversion without frequency offset (Figure 1.7b) would be preferable since the uniformity of the dispersion compensation improves as the (combined input and output)

spectrum narrows. To avoid crosstalk in spectral inversion without offset, the residual inputs would have to be attenuated relative to the mixer output (Figure 1.7b). In practical applications, an attenuation of 20 or 30 dB might be necessary. Gated mixing without frequency offset would also be desirable in time-division multiplexing or de-multiplexing; frequency conversion is an unnecessary side effect of these functions in standard OF mixers. However, operation at the DFM degeneracy point – which is also the location of the pump in standard, cascaded $\chi^{(2)}$ OF mixers – is especially challenging.

A standard solution to the distinguishability and spatial separation problem is to use interacting waves with orthogonal polarizations (type II phase matching). For example, input waves launched with ordinary polarization can produce mixer output with extraordinary polarization; the two can be separated with a polarizing beam splitter. Unfortunately, this approach is incompatible with annealed proton-exchanged (APE) PPLN waveguides, which support only TM modes. Since type II phasematching uses smaller nonlinear coefficients, it is also less efficient than QPM with the diagonal d_{33} coefficient [49].

This thesis presents two new methods for managing the input and output signals in OF mixers. Section 4.4 demonstrates an integrated OF mixer that uses interferometer structures to spatially separate the desired output from the residual inputs. This device, an OF balanced mixer, uses a Mach-Zehnder interferometer with Y-junctions and π-phase-shifted QPM gratings. A second way to distinguish the input and output waves is to use odd and even waveguide modes. These modes can be filtered using integrated-optic structures. Chapter 5 describes components for high efficiency mixing and separation of higher-order waveguide modes, and presents an odd-to-even mode wavelength converter suitable for bi-directional wavelength conversion or spectral inversion without offset (Section 5.6).

Chapter 2

Theory of Guided-Wave Quasi-Phasematched Interactions

This chapter summarizes the basic theory of quasi-phasematched three-wave mixing in waveguides. A simple set of equations describes the propagation of waveguide modes coupled together by the second-order nonlinear susceptibility, $\chi^{(2)}$. These equations can be adapted to the special cases of second-harmonic generation (SHG), sum-frequency generation (SFG), and difference-frequency mixing (DFM). They also describe the cascaded three-wave mixing ($\chi^{(2)}$:$\chi^{(2)}$) interactions frequently used in 1550-nm-band OF mixers. Many textbooks on nonlinear optics [50, 51, 52] and waveguide theory [53, 42] provide a more thorough introduction to the concepts introduced in this chapter.

2.1 Coupled Mode Equations

Adding the induced nonlinear polarization $\mathbf{P_{NL}}$ to Maxwell's equations results in the nonlinear version of the familiar wave equation

$$\nabla^2\mathbf{E} = \mu_0\sigma\frac{\partial\mathbf{E}}{\partial t} + \mu_0\epsilon_0\epsilon\frac{\partial^2\mathbf{E}}{\partial t^2} + \mu_0\frac{\partial^2\mathbf{P_{NL}}}{\partial t^2}. \tag{2.1}$$

For waveguide interactions, we can assume that the electric field contains modes of the form

$$E_i(x,y,z,t) = \mathrm{Re}\Big\{\gamma_i \tilde{E}_i(x,y) A_i(z,t) \exp[j(\omega_i t - k_i z)]\Big\}. \tag{2.2}$$

This form separates out the real mode shape $\tilde{E}_i(x,y)$ and the slowly-varying complex amplitude $A_i(z,t)$ for a frequency component ω_i. $\tilde{E}_i$ is normalized so that

$$\int_{-\infty}^{\infty}\int_{-\infty}^{\infty} \tilde{E}_i{}^2(x,y)dxdy = 1, \tag{2.3}$$

and

$$\gamma_i \equiv \sqrt{\frac{2}{c\,\epsilon_0\, n_{eff,i}}}, \tag{2.4}$$

where the denominator includes the speed of light in vacuum, c, the permittivity of free space, ϵ_0, and the waveguide effective index $n_{eff,i}$ at frequency ω_i. This normalization makes the optical power equal to the magnitude squared of the envelope function, $\mathrm{P_i} = |A_i(z,t)|^2$. For simplicity, we omit additional field mode indices l, m on $\tilde{E}_{i,l,m}$ until they are needed to indicate higher-order waveguide modes.

For three-wave mixing interactions, the frequencies of interest will be related by

$$\omega_3 = \omega_1 + \omega_2, \tag{2.5}$$

as required by energy conservation. Due to the second-order nonlinear susceptibility, the nonlinear polarization has frequency components that are quadratic in the electric field:

$$P_{NL,3} = 2\epsilon_0 d E_1 E_2 \tag{2.6}$$

$$P_{NL,2} = 2\epsilon_0 d E_3 E_1^* \tag{2.7}$$

$$P_{NL,1} = 2\epsilon_0 d E_3 E_2^*, \tag{2.8}$$

where E_1, E_2, and E_3 are the field amplitudes at frequencies ω_1, ω_2, and ω_3. In general, the nonlinear coefficient d is spatially non-uniform. In this section we consider only

transverse variations in the nonlinear coefficient using the form $d(x,y) = d_0\bar{d}(x,y)$, where d_0 is the bulk nonlinear coefficient. Since annealed proton-exchanged waveguides only support the TM (transverse magnetic) polarization, we need only consider the component of the nonlinear susceptibility tensor corresponding to three TM-polarized fields. For the special case of second-harmonic generation (SHG), $\omega_3 = 2\omega_1$, and equation (2.6) is

$$P_{NL,3} = \epsilon_0 d E_1^2. \tag{2.9}$$

The coupled mode equations describing the evolution of the electric fields result from substituting the field (2.2) and nonlinear polarization components into (2.1), and assuming that the field amplitudes change slowly along z relative to the much larger optical carrier frequencies. The essence of this slowly varying envelope approximation is that $\frac{d^2E_i}{dz^2} \ll k_i \frac{dE_i}{dz}$, and can be ignored. The resulting first-order coupled differential equations for the field amplitudes are

$$\frac{dA_3}{dz} = -j\kappa_3 d(z) A_1 A_2 \exp(j\Delta k' z) - \frac{\alpha_3}{2} A_3 \tag{2.10}$$

$$\frac{dA_2}{dz} = -j\kappa_2 d(z) A_1^* A_3 \exp(-j\Delta k' z) - \frac{\alpha_2}{2} A_2 \tag{2.11}$$

$$\frac{dA_1}{dz} = -j\kappa_1 d(z) A_2^* A_3 \exp(-j\Delta k' z) - \frac{\alpha_1}{2} A_1. \tag{2.12}$$

The phase velocity mismatch is

$$\Delta k' = k_3 - k_2 - k_1 = 2\pi\left(\frac{n_3}{\lambda_3} - \frac{n_2}{\lambda_2} - \frac{n_1}{\lambda_1}\right), \tag{2.13}$$

where n_1, n_2 and n_3 are the effective indices at frequencies ω_1, ω_2, and ω_3. The power loss coefficients are

$$\alpha_i = \frac{\mu_0 \sigma_i c}{2}, \tag{2.14}$$

where σ is an effective conductivity that accounts for waveguide losses. The coupling coefficients are

$$\kappa_i = \sqrt{\frac{8\pi^2 d_0^2}{n_1 n_2 n_3 c \epsilon_0 \lambda_i^2}}\,\theta \tag{2.15}$$

where θ is the transverse overlap integral of the interacting modes with the nonlinear coefficient:

$$\theta = \int_{-\infty}^{\infty}\int_{-\infty}^{\infty} \bar{d}(x,y)\tilde{E}_1(x,y)\tilde{E}_2(x,y)\tilde{E}_3{}^*(x,y)\; dx\; dy \tag{2.16}$$

This overlap must be maximized for high efficiency nonlinear mixing. We can also describe the degree of overlap as an effective area $A_{eff} = 1/\theta^2$.

2.2 Quasi-Phasematched Three-Wave Mixing

2.2.1 Quasi-Phasematching

As mentioned in Section 1.2, the quasi-phasematching (QPM) technique compensates for phase velocity mismatch by modulating the nonlinear coefficient d along the propagation direction with period Λ_g [23, 24, 25]. We now define d to include this additional variation through $d(x,y,z) = d_0\bar{d}(x,y)g(x,y,z)$. The function g also accounts for transverse variations in the QPM grating amplitude and phase (Section 5.2), and may be complex. Expanding in a Fourier series,

$$g(x,y,z) = \sum_m G_m(x,y)\exp(-j2\pi mz/\Lambda_g), \tag{2.17}$$

with Fourier coefficients given by

$$G_m(x,y) = \frac{1}{\Lambda_g}\int_{-\Lambda_g/2}^{\Lambda_g/2} g(x,y,z)\exp(j2\pi mz/\Lambda_g). \tag{2.18}$$

For quasi-phasematching, the efficiency overlap integral becomes

$$\theta_m = \int_{-\infty}^{\infty}\int_{-\infty}^{\infty} \bar{d}(x,y)G_m(x,y)\tilde{E}_1(x,y)\tilde{E}_2(x,y)\tilde{E}_3{}^*(x,y)\; dx\; dy. \tag{2.19}$$

We adapt the coupled mode equations to the QPM case by inserting this form of $d(x,y,z)$ into (2.10) – (2.12), and assuming that the device length $L \gg \Lambda_g$:

$$\frac{dA_3}{dz} = -j\kappa_3 A_1 A_2 \exp(j\Delta kz) - \frac{\alpha_3}{2}A_3 \tag{2.20}$$

$$\frac{dA_2}{dz} = -j\kappa_2 A_1^* A_3 \exp(-j\Delta kz) - \frac{\alpha_2}{2} A_2 \tag{2.21}$$

$$\frac{dA_1}{dz} = -j\kappa_1 A_2^* A_3 \exp(-j\Delta kz) - \frac{\alpha_1}{2} A_1 \tag{2.22}$$

$$\kappa_i = \sqrt{\frac{8\pi^2 d_{eff}^2}{n_1 n_2 n_3 c\epsilon_0 \lambda_i^2}}\ \theta_m. \tag{2.23}$$

Here the phase mismatch becomes

$$\Delta k \equiv \Delta k' - K_{QPM} = k_3 - k_2 - k_1 - K_{QPM}, \tag{2.24}$$

with the grating k-vector

$$K_{QPM} = \frac{2\pi m}{\Lambda_g}. \tag{2.25}$$

The appropriate choice of Λ_g will satisfy the phasematching condition, $\Delta k = 0$, for a given interaction. Efficient mixing occurs at or near phasematching, when the nonlinear output grows monotonically. In the case of QPM, the effective nonlinearity in the coupling coefficient κ_i is scaled by the Fourier amplitude of the grating

$$d_{eff} = d_0 G_m = \frac{2d_0}{m\pi} \sin(m\pi D), \tag{2.26}$$

where the final expression includes the Fourier coefficient G_m for a typical form of $d(z)$, a periodic sign reversal with duty cycle D. For first-order QPM ($m = 1$), the optimal duty cycle is 50% and

$$d_{eff} = \frac{2}{\pi} d_0. \tag{2.27}$$

This reduction in the effective nonlinear coefficient is obvious in Figure 1.2. The generated output power, proportional to d_{eff}^2, is $(\frac{2}{\pi})^2$ times smaller for QPM than for the perfect phasematching.

2.2.2 Second-Harmonic Generation

The coupled mode equations can be simplified to yield analytical solutions in many important cases. In second-harmonic generation (SHG), there are only two interacting

waves, and $\omega_3 = 2\omega_1$. Ignoring propagations losses, and assuming that the pump wave is not depleted (the low conversion efficiency limit), the coupled mode equations are simply

$$\frac{dA_3}{dz} = -\frac{1}{2} j\kappa_3 A_1^2 \exp(-j\Delta k z) \tag{2.28}$$

$$\frac{dA_1}{dz} = 0. \tag{2.29}$$

The extra factor of $\frac{1}{2}$ in (2.28) originates in the form of the nonlinear polarization given in (2.9) versus the one in (2.6). Integrating $A_3(z)$ and taking its magnitude squared yields the following solution for the second-harmonic (SH) output power as a function of the input pump power, $P_1(0)$:

$$P_3(L) = \eta_{nor} L^2 [P_1(0)]^2 \mathrm{sinc}^2(\Delta k L/2) \tag{2.30}$$

or

$$\eta_{SHG} = \frac{P_3(L)}{[P_1(0)]^2} = \eta_{nor} L^2 \tag{2.31}$$

at phasematching, when $\Delta k = 0$. The length-normalized efficiency $\eta_{nor} = \frac{1}{4}\kappa_3^2 = \kappa_1^2$ and has units of $(\mathrm{W}^{-1} \cdot \mathrm{m}^{-2})$. State-of-the-art devices in annealed proton-exchanged (APE) PPLN waveguides at 1.5 μm have normalized efficiencies approaching $100\%/\mathrm{W}\cdot\mathrm{cm}^2$ and can be made several centimeters long, resulting in efficiencies greater than 3000%/W. The low conversion efficiency limit, in which $\eta_{nor} L^2 P_1 < 0.2$, generally corresponds to pump power levels below 10 mW. Measurements of SHG efficiency as a function of phase mismatch produce tuning curves with a sinc^2 shape in ideal devices.

2.2.3 Sum-Frequency Generation

Experiments described in Chapter 5 combine SHG with sum-frequency generation (SFG). In the same low conversion limit, the coupled mode equations with two pumps $P_1 \approx P_2$ are

$$\frac{dA_3}{dz} = -j\kappa_3 A_1 A_2 \exp(-j\Delta k z) \tag{2.32}$$

$$\frac{dA_1}{dz} = 0, \quad \frac{dA_2}{dz} = 0. \tag{2.33}$$

They yield the result

$$P_3(L) = 4\eta_{nor}L^2P_1(0)P_2(0)\text{sinc}^2(\Delta kL/2). \tag{2.34}$$

Comparing (2.34) with (2.30) shows that the SFG conversion efficiency η_{SFG} is four times larger than η_{SHG} when the pump powers are equal in both cases. This is not surprising since doubling the total pump power doubles the conversion efficiency of $\chi^{(2)}$ processes. In a rather different case of SFG, an analytic solution to the coupled mode equations is also possible when $P_2 \gg P_1$, and depletion of the signal P_1 is taken into account; in this case the SFG output and the residual signal evolve as $\sin^2$ and $\cos^2$ [51].

2.2.4 Difference-Frequency Mixing

Most OF mixers for communications applications utilize near-degenerate difference-frequency mixing (DFM) processes, with signal and idler (input and output) in the 1550-nm-band, and a pump (local oscillator) near 775 nm. Accordingly, we relabel $(\omega_3, \omega_2, \omega_1)$ as $(\omega_{LO}, \omega_S, \omega_{OUT})$. With this notation, the coupled mode equations are

$$\frac{dA_{LO}}{dz} = -j\kappa_{LO}A_SA_{OUT}\exp(j\Delta kz) - \frac{\alpha_{LO}}{2}A_{LO} \tag{2.35}$$

$$\frac{dA_S}{dz} = -j\kappa_SA^*_{OUT}A_{LO}\exp(-j\Delta kz) - \frac{\alpha_S}{2}A_S \tag{2.36}$$

$$\frac{dA_{OUT}}{dz} = -j\kappa_{OUT}A^*_SA_{LO}\exp(-j\Delta kz) - \frac{\alpha_{OUT}}{2}A_{OUT} \tag{2.37}$$

The solutions to these equations in the absence of propagation losses and pump depletion ($\frac{dA_{LO}}{dz} = 0$) are

$$A_S(L) = A_S(0)\cosh(gL) \tag{2.38}$$

$$A_{OUT}(L) = \frac{j}{g}\kappa_{OUT}\exp(-\Delta kL/2)A_{LO}A^*_S(0)\sinh(gL) \tag{2.39}$$

where the gain coefficient g is defined as

$$g = \sqrt{\kappa_S \kappa_{OUT} P_{LO} - \frac{(\Delta k)^2}{4}}, \tag{2.40}$$

where P_{LO} is the local oscillator power (near 775-nm). For $\omega_S \approx \omega_{OUT}$,

$$\eta_{nor} \approx \kappa_S \kappa_{OUT}, \tag{2.41}$$

the same normalized efficiency as in the SHG case. Note that A_S and A_{OUT} both grow with distance (parametric amplification), and that both phase conjugation and a linear response are built into equation (2.39). For phasematched DFM in the limit of low conversion efficiency ($\eta_{nor} L^2 P_{LO} < 0.2$), the DFM efficiency

$$\eta_{DFM} = \frac{P_{OUT}(L)}{P_S(0)} \approx \eta_{nor} L^2 P_{LO}, \tag{2.42}$$

similar to the SHG case.

2.2.5 Cascaded SHG and DFM

Cascading SHG and DFM has become a preferred mode of operation for OF mixers, as described in Section 1.2. The second-harmonic wave generated from a strong 1550-nm pump becomes the local oscillator needed for 1550-nm-band DFM. In most cases, the two mixing processes occur simultaneously in the same device, and can be described using four coupled mode equations. Keeping the notation from Section 2.2.4, we add a pump wave ω_P such that $\omega_P \approx \omega_S \approx \omega_{OUT}$ and $\omega_{LO} = 2\omega_P$. Simplifying the coupling constants so that $\kappa \equiv \kappa_P \approx \kappa_S \approx \kappa_{OUT}$ (and $\kappa_{LO} = 2\kappa_P$), the coupled mode equations for SHG:DFM are

$$\frac{dA_P}{dz} = -j\kappa A_{LO} A_P^* \exp(j\Delta k_{SHG} z) - \frac{\alpha_P}{2} A_P \tag{2.43}$$

$$\frac{dA_{LO}}{dz} = -j\kappa A_P A_P \exp(j\Delta k_{SHG} z) - 2j\kappa A_S A_{OUT} \exp(j\Delta k_{DFM} z) - \frac{\alpha_{LO}}{2} A_{LO} \tag{2.44}$$

$$\frac{dA_S}{dz} = -j\kappa A^*_{OUT} A_{LO} \exp(-j\Delta k_{DFM} z) - \frac{\alpha_S}{2} A_S \tag{2.45}$$

$$\frac{dA_{OUT}}{dz} = -j\kappa A^*_{S} A_{LO} \exp(-j\Delta k_{DFM} z) - \frac{\alpha_{OUT}}{2} A_{OUT}. \tag{2.46}$$

The phase mismatch terms for the two processes are defined by $\Delta k_{SHG} = k_{LO} - 2k_P$ and $\Delta k_{DFM} = k_{LO} - k_S - k_{OUT}$. In general, these equations must be solved by numerical integration; most mixing processes require significant pump depletion to generate a strong local oscillator for high conversion efficiency, and losses cannot be ignored in realistic simulations. It is still useful, however, to derive the simplest possible analytic solution by again ignoring losses and pump depletion:

$$\eta_{SHG:DFM} = \frac{P_{OUT}(L)}{P_S(0)} \approx \frac{1}{4}\eta^2_{nor} L^4 P^2_P. \tag{2.47}$$

The higher powers of P_P, L, and η_{nor} in this result are exactly as expected from substituting a local oscillator produced by SHG into a DFM process (equations (2.31) and (2.42)), and heighten the importance of device length and normalized efficiency in cascaded processes. The factor of $\frac{1}{4}$ accounts for the uneven distribution of DFM efficiency across the device length. Most of the DFM occurs near the output end of the device, after P_{LO} has grown – quadratically with propagation length – to appreciable levels. In practice, it is possible to reach 0-dB conversion efficiency with $P_P < 200$ mW in standard OF mixers in APE PPLN waveguides.

2.2.6 Cascaded SFG and DFM

Cascaded SFG and DFM can be a convenient alternative to cascaded SHG:DFM when two pump sources are available. Instead of pumping an OF mixer with a single 1550-nm source at the DFM degeneracy point, two pumps can be placed at the edges of the 1550-nm-band. This scheme facilitates operation at or near the degeneracy point because it eliminates parasitic mixing between the pump and signals (by SFG or SHG), which was not considered in Section 2.2.5. In practice, signals must be excluded from a "guard band" around each pump wavelength that is defined by the narrow (typically ≤ 0.5 nm) SFG bandwidth. The odd-even mode mixer in Section

5.6 enables operation at degeneracy using cascaded SFG:DFM and a solution to the distinguishability problem. Cascaded SFG:DFM processes can also be used to convert an arbitrary input frequency to an arbitrary output frequency by first summing to the degeneracy point with one pump, and then difference-frequency mixing with the other.

With two pump fields, there are five coupled mode equations:

$$\frac{dA_{P1}}{dz} = -j\kappa A_{LO}A_{P2}^{*}\exp(j\Delta k_{SFG}z) - \frac{\alpha_{P1}}{2}A_{P1} \tag{2.48}$$

$$\frac{dA_{P2}}{dz} = -j\kappa A_{LO}A_{P1}^{*}\exp(j\Delta k_{SFG}z) - \frac{\alpha_{P2}}{2}A_{P2} \tag{2.49}$$

$$\frac{dA_{LO}}{dz} = -2j\kappa A_{P1}A_{P2}\exp(j\Delta k_{SFG}z) - 2j\kappa A_{S}A_{OUT}\exp(j\Delta k_{DFM}z) - \frac{\alpha_{LO}}{2}A_{LO} \tag{2.50}$$

$$\frac{dA_{S}}{dz} = -j\kappa A_{OUT}^{*}A_{LO}\exp(-j\Delta k_{DFM}z) - \frac{\alpha_{S}}{2}A_{S} \tag{2.51}$$

$$\frac{dA_{OUT}}{dz} = -j\kappa A_{S}^{*}A_{LO}\exp(-j\Delta k_{DFM}z) - \frac{\alpha_{OUT}}{2}A_{OUT}. \tag{2.52}$$

The phase mismatch terms are $\Delta k_{SFG} = k_{LO} - k_{P1} - k_{P2}$ and $\Delta k_{DFM} = k_{LO} - k_{S} - k_{OUT}$. Ignoring losses and depletion of either pump, the conversion efficiency is a factor of four larger than in the SHG:DFM case:

$$\eta_{SFG:DFM} = \frac{P_{OUT}(L)}{P_{S}(0)} \approx \eta_{nor}^{2}L^{4}P_{P1}P_{P2}. \tag{2.53}$$

This increase can be realized in cases where it is easier to double the number of pumps than to double the power of a single pump. Accommodating a second pump is easy when all the wavelengths are combined in optical fiber.

Chapter 3

Fabrication of Integrated OF Mixers in PPLN waveguides

3.1 Introduction

Compared to standard OF mixers, integrated OF mixers present an additional set of fabrication challenges. While all QPM mixing devices tend to have tight fabrication tolerances set by the phasematching bandwidth, integrated optics structures such as interferometers can reduce these tolerances much further. Increasingly complicated device geometries require precise fabrication steps and precise alignment between steps. Ultimately, the yield and reproducibility of the process determine the degree to which device designs can be characterized, and multiple devices can be integrated together. This chapter provides an overview of integrated OF mixer fabrication, focusing on recent process developments that allow the production of PPLN waveguides with higher precision, yield, and reproducibility than ever before. It also discusses the gains made by creating a wafer-scale batch process. These improvements have led to the novel devices described in subsequent chapters.

Lithium niobate (and other members of its ferroelectric oxide family) are attractive nonlinear optical materials. They have a relatively large nonlinear coefficient (d_{33} = 27 pm/V for congruent $LiNbO_3$) and a transparency range spanning the ultraviolet to the mid-infrared (≈325-4500 nm for congruent $LiNbO_3$). In addition, stable sources

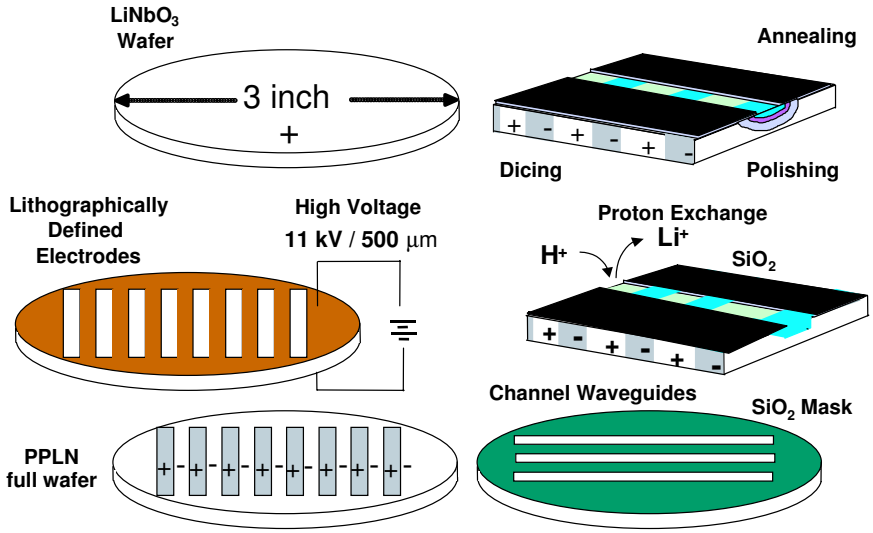

Figure 3.1: Processing steps in OF mixer fabrication.

of high quality material exist due to the large scale production of $LiNbO_3$ wafers (tons per year) for optical modulators [54] and surface-acoustic-wave RF filters [55].

There are two major steps in fabricating integrated OF mixers: creating QPM gratings by electric-field periodic poling, and making waveguides by annealed proton exchange. These steps are summarized (counter-clockwise from the top left) in Figure 3.1. During poling, a large but carefully controlled electric field is applied to a wafer through lithographically patterned electrodes. This field changes the orientation of crystal domains, locally reversing the sign of the nonlinear coefficient to create a QPM grating structure. This technique, developed in the early 1990s in $LiNbO_3$ [56, 57], was rapidly adopted, improved, and extended to a variety of other ferroelectric crystals. It provides a solid foundation for the development of the state-of-the-art periodically-poled structures described in this thesis. Proton-exchanged waveguides are formed by diffusing lithium ions of out the surface of the substrate and replacing them with hydrogen ions from an acid bath; this process increases the extraordinary index of refraction. Channel waveguides are formed using a lithographically patterned layer of SiO_2 as a mask. The waveguides are later annealed to reduce propagation losses and increase nonlinear response. Annealed proton exchanged (APE) waveguides were first

developed in the early 1980's [58, 59], but an adequate model for OF mixer design – describing both linear and nonlinear optical properties – was not available until the early 1990's [60]. Refinement of this model during the past four years [61] has accelerated the development of integrated OF mixers.

3.2 Periodically Poled Lithium Niobate

To fabricate PPLN for integrated OF mixers, we have made small improvements upon previously reported recipes for poling 3-inch-diameter, 500-μm-thick wafers [62, 63]. The improved process enables poling of smaller features than ever before, with little variation from wafer to wafer. We use optical grade z-cut $LiNbO_3$ wafers from Crystal Technologies, Inc., and pattern Clariant AZ4620 photoresist using a standard process and exposure tool. Even with this relatively thick resist ($\approx 6\mu$m), we can pattern features smaller than 1.5 μm reliably. After curing at 150° C, the patterned AZ4620 has enough dielectric strength to insulate the wafer during electric-field poling. The openings in the photoresist, contacted with a liquid electrolyte solution, become the poling electrodes.

The use of narrow or segmented electrodes represents an important departure from previous processes. Whereas in previous OF mixers millimeter-wide gratings covered multiple waveguide devices, in integrated OF mixers different gratings for every waveguide are often essential. With narrow, 35-μm-wide (measured perpendicular to the k-vector) grating stripes that cover a single waveguide, adjacent waveguides can have different grating periods or phases. Devices like the OF balanced mixer (Section 4.4) require this flexibility. Furthermore, segmented electrodes *improve* domain fidelity, by preventing the lateral spread of "run-together" or merged domains. Segmentation also increases the density of domain nuclei at the onset of poling, since nuclei occur at one or both ends of each electrode. Instead of spreading laterally over hundreds of microns, each domain grows from a nearby nucleus, resulting in more homogenous poling with a constant duty cycle [64]. Figure 3.2 shows good fidelity using segmented electrodes (top) under poling conditions that cause standard gratings to merge completely (bottom). The electrode width (2.0 μm) and grating period (8.0 μm) – the

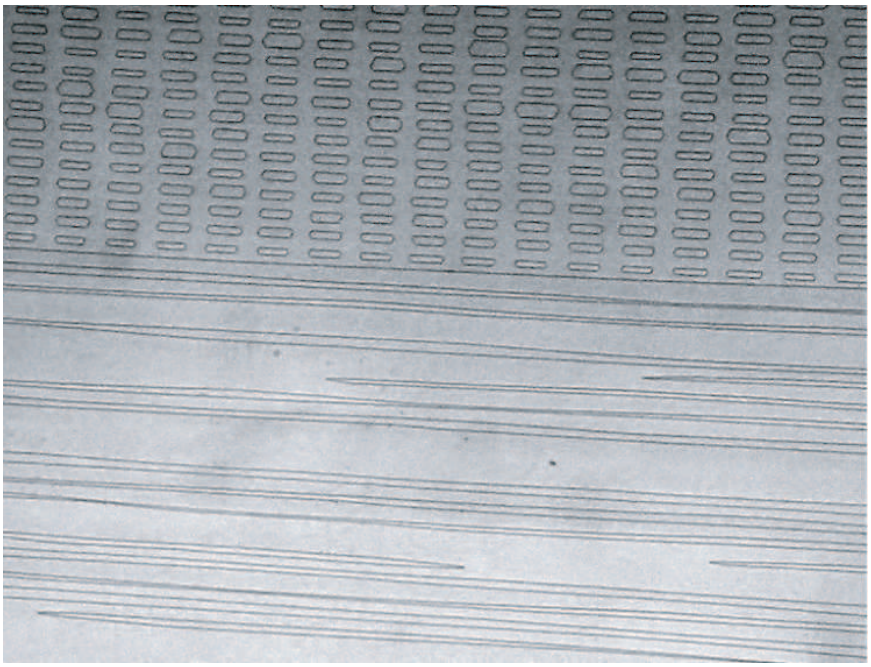

Figure 3.2: Good quality poling using segmented electrodes (top) under poling conditions that cause standard gratings to merge completely (bottom).

same for both sections – are deliberately mismatched in this case.

Several updates to the traditional acrylic poling fixture (Figure 3.3) have made the process more reproducible. Catastrophic dielectric breakdowns and wafer cracking have been linked, in part, to piezoelectric stresses induced in the wafer during poling. Switching from viton to softer (40-60 durometer) silicone-rubber O-rings, and using a torque wrench to set the clamping tension below 0.4 N/m has made breakdowns rare for 500-μm-thick wafers. Silicone-rubber O-rings also have higher electrical resistance. The O-ring diameter has been increased to make full use of 3" wafers, allowing QPM gratings as long as 65 mm. Using a similar poling fixture design for 4" wafers, 85-mm-long gratings have been fabricated with excellent fidelity, as shown in Figure 3.4. Clamping tension is even more critical for 4" wafers, which are typically 0.7-mm-thick.

The electrolyte solution is now standardized (500g LiCl per 660 mL water) just below its saturation point to prevent crystals from coming out of solution. Filtering with grade #4 paper removes contaminants that appear in some bottles of LiCl.

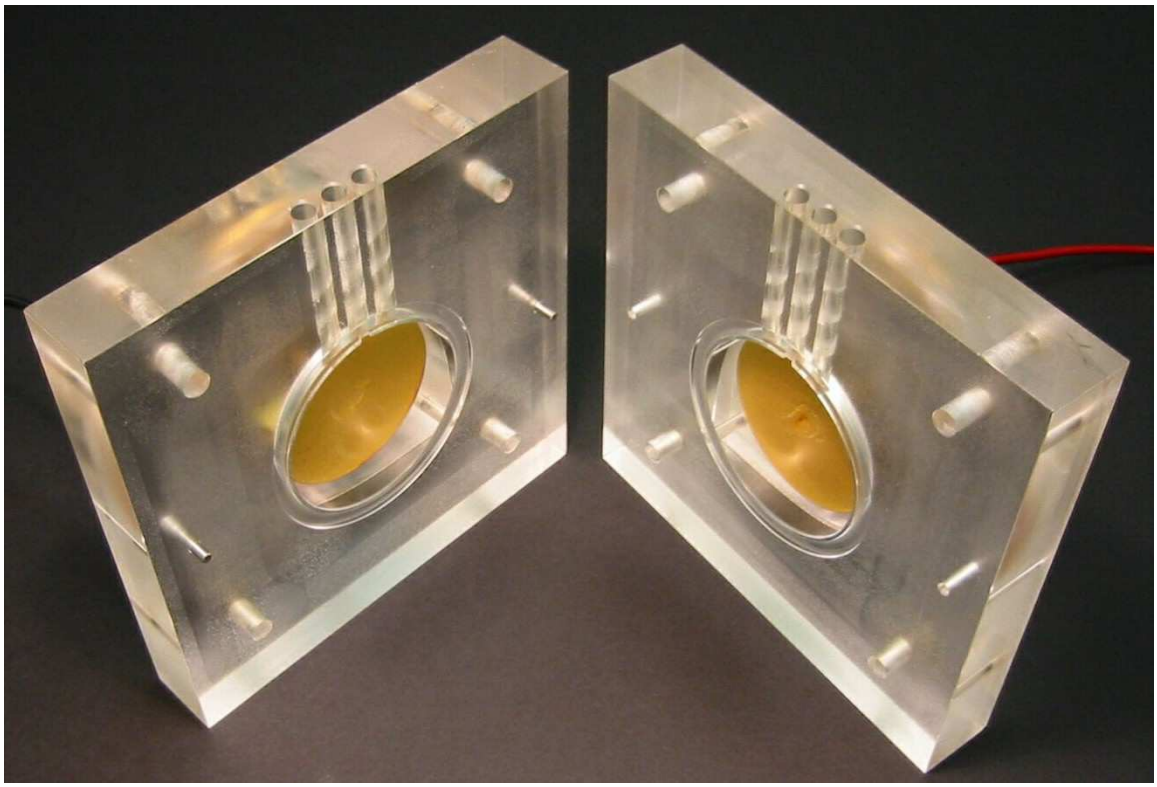

Figure 3.3: Acrylic poling fixture for electric field poling.

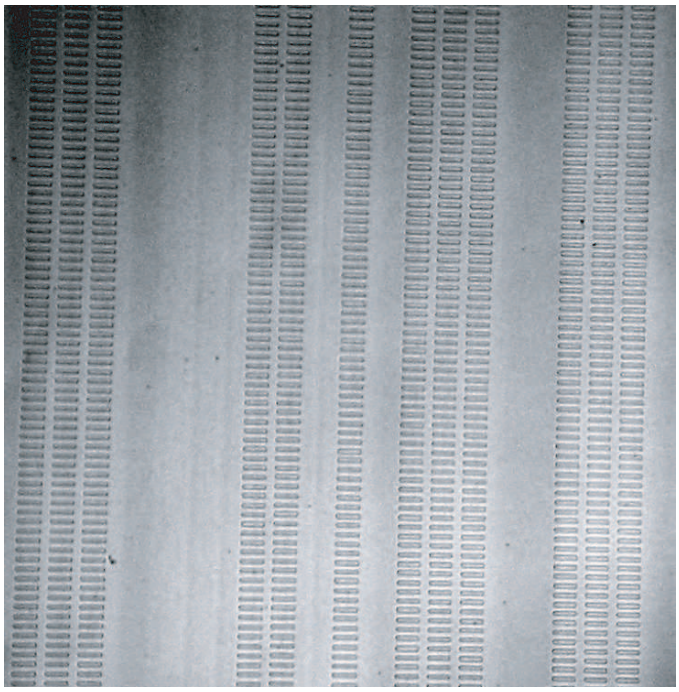

Figure 3.4: High quality 14.75-μm-period gratings (35-μm wide) in a 4", 0.7-mm-thick wafer.

Particles or bubbles, particularly near the wafer surface, can affect poling fidelity by altering the local electric field. It is helpful to load the electrolyte solution through Tygon tubing to avoid creating bubbles. A small cut in the inner o-ring groove atop the wafer allows bubbles that cling to the wafer surface to escape through the filling holes.

Minimizing the time between loading the electrolyte solution and the poling also reduces the chances of failure by delamination of the photoresist. The entire process of clamping a wafer, filling the fixture with electrolyte solution, applying the poling voltage, and unloading the wafer now takes less than 10 minutes. Since the effects of the metal contacts inside the poling fixture on the poling process are not completely understood, it seems wise to prevent their gradual corrosion. These contacts must withstand repeated exposure to lithium chloride and occasionally conduct over 20 mA of current: a challenging environment. A thick (.001") gold coating and a strict rinsing regimen between poling sessions has nearly stopped the corrosion process for stainless steel electrodes.

Our best results come from poling at a constant applied field of 21.8 kV/mm, slightly above the coercive field necessary for domain inversion. This value is within the optimal range described by Miller [65] for "self-terminating" poling, i.e., poling conditions that force the domain growth to slow down by negative feedback when a 50% grating duty cycle has been reached. Some recent work has used poling fields as high as 22.3 kV/mm, and a poling spike as high as 23-24 kV/mm [66] in order to increase the nucleation density. Since the domain-wall velocity increases exponentially with field, this small change results in a faster poling process that immediately reaches the electrical current limit of the high voltage amplifier. It can also slightly reduce the overall uniformity of the poling, making it harder to achieve an ideal 50% duty cycle. A slower, non-current-limited poling process without a poling spike seems preferable, particularly when segmented electrodes enhance nucleation.

Figure 3.5 shows experimental traces of poling current (thin black trace) and voltage (thick gray trace, no scale) from four different wafers, the top two having the same mask pattern and processing conditions. The poling waveform is programmed on a SRS DS345 waveform generator and amplified with a TREK 2020 high voltage

amplifier to a peak level of 21.8 kV/mm. The gradual ramps and the dwells at 90% of the coercive field are set in accordance with earlier work, except for the post-poling dwell segment, which is increased by a factor of five, to 500 msec. This increase helps stabilize smaller, more densely-packed domains which have a greater tendency to "flip back" to their original orientation when the poling field is turned off.

The total amount of charge required to pole a wafer is given by

$$Q = \int I_p(t)dt = 2P_sA_p \tag{3.1}$$

where $P_s = 78\mu\text{C/cm}^2$ is the spontaneous polarization of $LiNbO_3$, A_p is the domain inverted area, and the factor of two accounts for the polarity reversal. For a 50%-duty-cycle grating, A_p equals one-half of the "total poled area" commonly calculated by our mask writing software. $I_p(t)$, the poling current drawn by the entire wafer, is a complicated function of the domain growth dynamics, the electrode pattern, and the applied field. The current traces in Figure 3.5 exemplify the variety of $I_p(t)$ behaviors possible for different electrode geometries, while the similarities between the first two traces demonstrate the wafer-to-wafer reproducibility of the poling process.

The total area to be poled sets the duration of the poling waveform. For a constant I_p, the correct poling time τ is simply $2P_sA_p/I_p$. In the current-limited poling process, I_p clamps at the amplifier current limit (21.5 mA) until the domain growth self-terminates. When poling below this limit, it is harder to predict τ in advance for a new mask pattern. However, an exact value is unnecessary because of the strong self-termination effect, and assuming an average current of 7 mA works in practice. If the selected τ is too short, additional shots of the poling waveform can be applied until the poling finishes. The poling quality does not degrade (and may in fact improve [67]) when the poling occurs in multiple short bursts.

3.3 The Standard Long Doubler Device

In the late-1990's, a highly successful 1550-nm-band OF mixer design emerged from annealed proton-exchanged (APE) PPLN waveguide technology. This standard OF

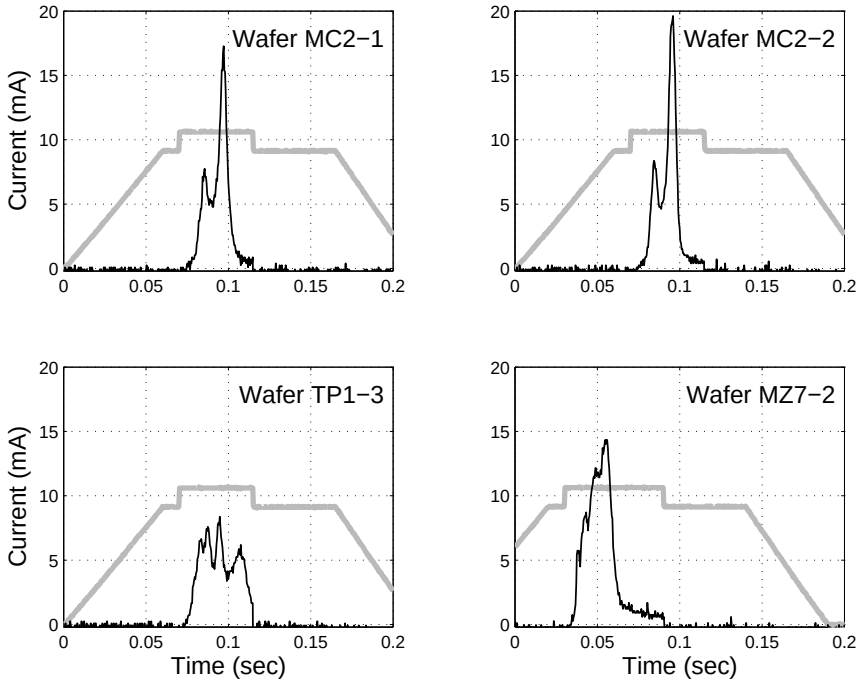

Figure 3.5: Measured poling current (black) and voltage (gray, scale not shown) traces for four different wafers. The top two traces, which have the same mask pattern and poling conditions, demonstrate the wafer-to-wafer reproducibility of the poling process. The bottom two wafers show the variability of $I_p(t)$ for different mask patterns.

mixer device has been used for all of the optical signal processing functions described in Section 1.2. Still, we refer to this device as the "standard long doubler" because its most basic function is frequency-doubling of 1550-nm light. Integrated OF mixers build upon the successful features of the standard long doubler.

The high efficiency of the long doubler design can be attributed to three key developments, which are described in more detail elsewhere [68, 66]. The first is an optimization of APE waveguides for high mixing efficiency and low losses. Before thermal annealing, PE waveguides have a relatively large step-index profile ($\Delta n_e \approx 0.09$ at 1550 nm), but have high propagation losses and low nonlinearity. During annealing the protons diffuse deeper into the substrate, smoothing and reducing the height of the index profile. While this diffusion reduces mode confinement and overlap (which determine efficiency), lower proton concentrations (C) also increase nonlinearity and reduce propagation losses, typically to below 0.2 dB/cm. These changes come from a transition between two phases of $H_xLi_{1-x}NbO_3$ as x decreases. The phase boundary usually sets the optimal peak concentration for an APE waveguide. The fact that the proton diffusion coefficient D is concentration-dependent complicates the waveguide modelling. Separate studies in planar waveguides were needed to characterize $D(C)$ and $n(C, \lambda)$, the refractive index as a function of proton concentration and wavelength [60]. These models have propelled the development of efficient, low-loss OF mixers, and are indispensable in designing integrated-optic structures.

A second essential feature of the standard long doubler is a "dimensionally non-critical" phasematching design [69, 70]. Even small variations in waveguide geometry can alter the QPM condition ($\Delta k = 0$), reducing mixing efficiency. In a full-length mixer with a 5-cm interaction length, the waveguide width might need to be controlled to within ± 10 nm, or much less than 1%. This is a formidable challenge given that 100 nm is a standard mask tolerance, and that the exposure uniformity tolerance in lithography tools is often 5%. Waveguide geometries that make the phasematching condition insensitive to waveguide width, to first order, can significantly reduce these tolerances. In a non-critical phasematching design, $\frac{d(\Delta k)}{dw} = 0$, where w is the waveguide width. Fortunately non-critical designs exist for APE waveguides, and the

non-critical waveguide width ($\approx 13\mu$m in typical devices) happens to provide relatively good mode confinement and overlap. In the standard design, the waveguides are proton exchanged to an initial depth of 0.81-0.83 μm and annealed for 23 hours at 330° C. These same parameters are used in all of the waveguide devices described in this thesis.

Adiabatic tapers that facilitate lowest-order TM_{00} mode launching are a third key technology in standard long doublers [66], which use only TM_{00} mode mixing. Coupling light into the TM_{00} mode of a 13-μm, non-critical width waveguide is delicate because of the small mode size and the presence of three higher-order modes. A 4-μm-width waveguide has a single mode much better suited in size and shape for fiber or free-space coupling. Adiabatic tapers (typically 1-mm long) between the 4-μm and 13-μm widths combine effective launching and efficient mixing, and are now a standard part of every OF mixer.

3.4 Waveguide Fabrication

The standard long doubler device is the starting point for integrated OF-mixer designs. This choice constrains the fabrication parameter space to the standard exchange depth (0.81-0.83 μm) and annealing (23 hours at 330° C), but still leaves room for the development of integrated optics structures. Before this development occurred, however, several improvements were needed.

In order to adopt a "standard" set of fabrication parameters, these parameters had to be characterized with higher precision than ever before. This led to a series of temperature calibrations for the PE bath and the annealing oven, and refined techniques for measuring the initial exchange depth of a sample. With a low-temperature annealing step that homogenizes the $H_xLi_{1-x}NbO_3$ phase, it is possible to measure the exchange depth (or more precisely, the total number of protons) to within 0.5% [71], using either a prism coupler measurement [72] or an infrared absorption measurement that is proportional to the OH^- concentration [73, 74]. Critical feature sizes, like the optimal width for fiber mode-matching, were retested and updated. With a better exposure tool and photoresist recipe, the waveguide lithography now produces SiO_2

features that more closely match the programmed mask design.

Both the proton exchange (PE) bath and the annealing oven were revamped in an effort to improve waveguide uniformity and device reproducibility. Uniformity is critical for maintaining QPM over a long interaction length. From our fabrication model we calculate that for the standard long doubler, the average acid temperature during proton exchange must not vary by more than 0.025 K across the device. During annealing this tolerance is 0.030 K. Furthermore, without reproducibility in the absolute temperatures, designing sensitive structures such as π-phase shifters or 50% directional couplers is futile.

Previous versions of the PE bath suffered from temperature variations due to evaporation of the benzoic acid and large thermal gradients from incomplete insulation. An asymmetric sample fixture that caused irregularities in the flow of molten acid around the sample may have also been at fault. The latest version of the PE bath has improved sealing and insulation to prevent thermal gradients. Long-term stability is better because of a larger silicone oil bath (8 liters) with greater thermal mass. A 2000-mL beaker of molten acid, large enough to exchange whole 4" wafers, sits nearly submerged in the oil bath. Larger acid volumes became a necessity to accommodate longer samples without significant temperature gradients. During exchange, whole wafers are held in a fixture that exposes most of the wafer surface for maximal acid flow. Smaller pieces can be held in a separate basket system.

A new ring stand system (Figure 3.6) supports the beaker of acid in the silicone oil bath while stirring the oil with a 4" propeller. A powerful magnet actuates the stirring through the base insulation, and this force is transferred to a stir bar inside the acid beaker via another magnet. Improved mixing reduces temperature gradients within the oil below 2 K (now regularly monitored with multiple RTDs (resistance temperature devices)), and within the acid bath to $\approx$ 10 mK. Heating the oil from within using a submerged 800 W resistive heater instead of an external hotplate improves the temperature servo performance.

The annealing furnace has been expanded to a 5" diameter to handle whole 3" and 4" wafers. A new sample boat was designed for simpler, more reproducible loading procedure. As with the PE bath, increasing the thermal mass improves long term

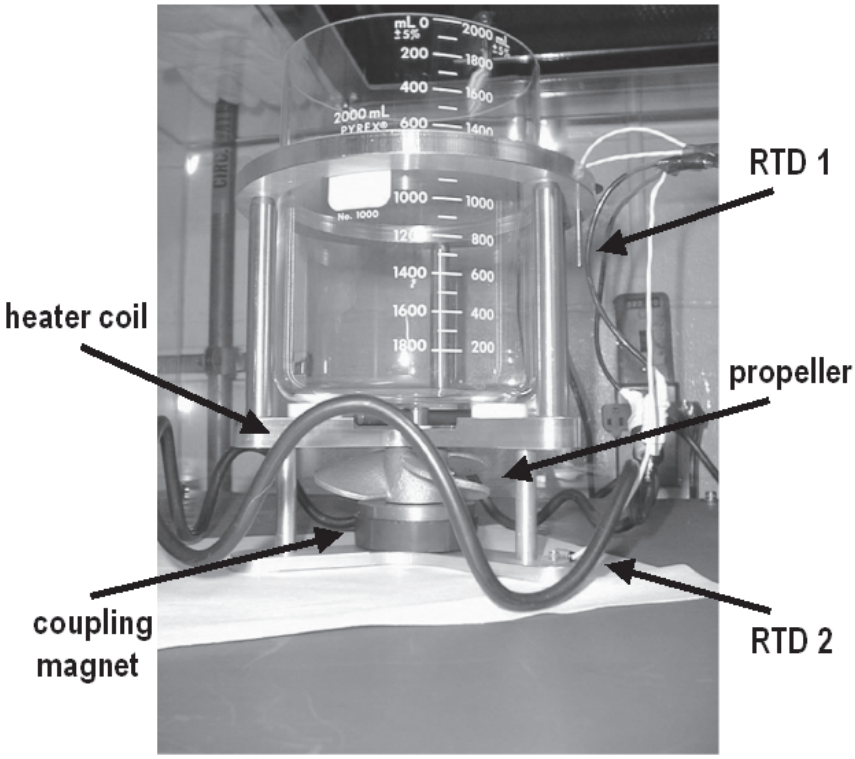

Figure 3.6: Ring stand system and beaker for proton exchange in benzoic acid. The apparatus shown is submerged in a larger silicone oil bath.

stability and ensures that the sample loading is a small perturbation to the oven temperature. The metal sample boat also provides a final buffer against temperature gradients by short-circuiting them with high conductivity. While switching from copper to aluminum reduces this conductivity by a factor of two, it has also reduces corrosion, leaving a flatter surface for more uniform wafer contact.

3.5 Full-Wafer Batch Processing

The development of a full-wafer batch process for PPLN OF mixers has been one of the most significant contributions of this thesis. From the perspective of time savings alone, a batch process is invaluable. Turning a $LiNbO_3$ wafer into a finished OF mixer device takes 15-20 hours of active fabrication time, which must be spread over of a minimum of 5 days because of 60 additional interim hours (during the photoresist baking, proton exchange, and annealing). Moreover, an experiment sometimes requires more than one copy of a device, and a project might need multiple iterations of a mask design. The result can be a disproportionate emphasis on fabrication rather than device design or testing. To save time and energy for these more creative aspects of research, the fabrication time per device must managed by processing multiple devices in parallel. The increasing size and complexity of integrated OF mixers result in fewer devices per chip and lower yield rates, heightening the need for a batch process.

The most time-consuming patterning steps (the poling lithography, the poling itself, and the waveguide lithography) can be done on whole cassettes of wafers at a time in a batch process. Each additional wafer adds marginally to the total processing time, even when processing wafers from different mask sets. The most critical step in developing this process was the switch from baking photoresist-covered wafers individually on hotplates to baking cassettes of wafers in large ovens.

$LiNbO_3$ wafers must be electrically discharged after baking to prevent the buildup of pyroelectric charge from the temperature dependence of the spontaneous polarization [75]. Charge buildup as a wafer cools down can cause extraneous poling (microdomains) or arcing through the photoresist pattern, and it attracts particles. Discharge plates made from silicon wafers alleviate these problems. Figure 3.7c shows

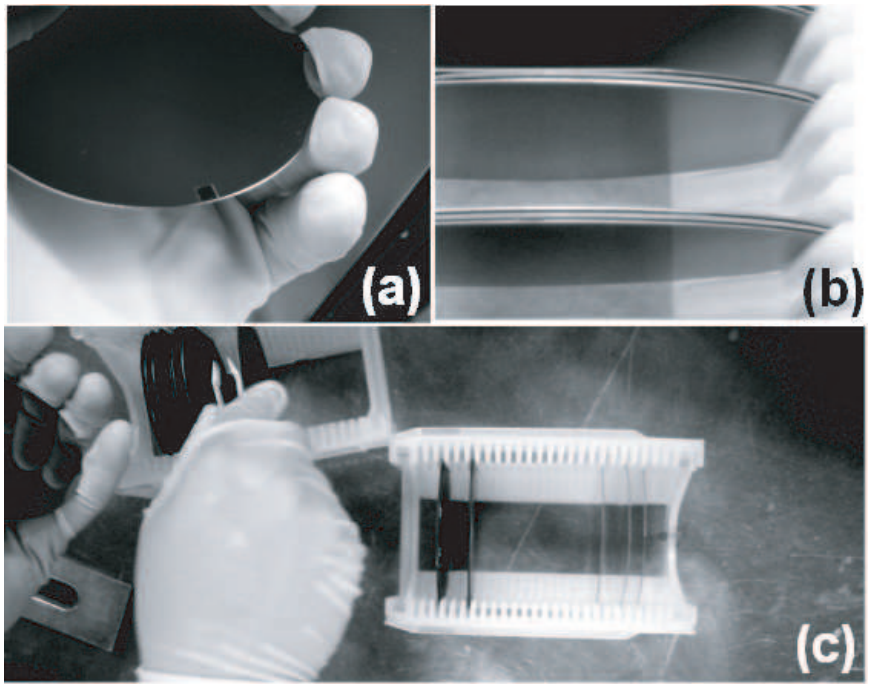

Figure 3.7: Using silicon discharge plates after baking a cassette of wafers.

how each wafer in a cassette is sandwiched (Figure 3.7b) between discharge plates after baking. This system makes it possible to do a standard "soft-bake" before exposure, and "post-bake" after development. At the wafer edges (Figure 3.7a), glass standoffs (200-μm-thick, and 3 mm $\times$ 3 mm) separate the silicon and $LiNbO_3$ wafers, preventing adhesion. Placing the loaded cassette inside a teflon box regulates the cooling process. Previously, wafers were baked on a hotplate and discharged with a metal plate or a chrome mask. In general, the hotplate process tends to be less reproducible than using an oven, but its major drawback is a lack of scalability, since most hotplates can only fit one wafer at a time.

A full-wafer batch process also makes wafer handling and cleaning easier. Detergent cleaning before and after the proton exchange – a relatively easy step for a whole wafer, but not for small pieces – may have been a factor in reducing propagation losses. Cleaning and handling steps can also be omitted by performing the "dirtiest" fabrication steps, dicing and polishing, last.

The entire fabrication process has reached an impressive level of standardization, beginning with the mask layout software. MATLAB^{TM} code is still used to create mask files in the CIF format [76]. However, there is now a library of mask functions and subfunctions for creating everything from straight waveguides to raised cosine bends to complete devices with QPM gratings. This accelerates mask design and avoids duplication of work between designers. Writing the waveguide and poling masks simultaneously prevents registration errors and automatically keeps track of the total poling area on the wafer. Typical waveguide masks also include dicing markers and lines that help when using outside foundries. Choosing a standard chip size can streamline the dicing, polishing, and optical testing by reducing the number of customized sample fixtures.

Alignment markers are critical for fabricating integrated OF mixers, which can require micron-scale alignment between poling and waveguide features. Figure 3.8d shows a group of standard alignment structures. The simplest markers are small grating sections that can be viewed through openings in the (dark-field) waveguide mask during lithography (Figure 3.8a). These alignment windows are helpful for coarse alignment, especially when grouped in progressively smaller sets. Finer alignment

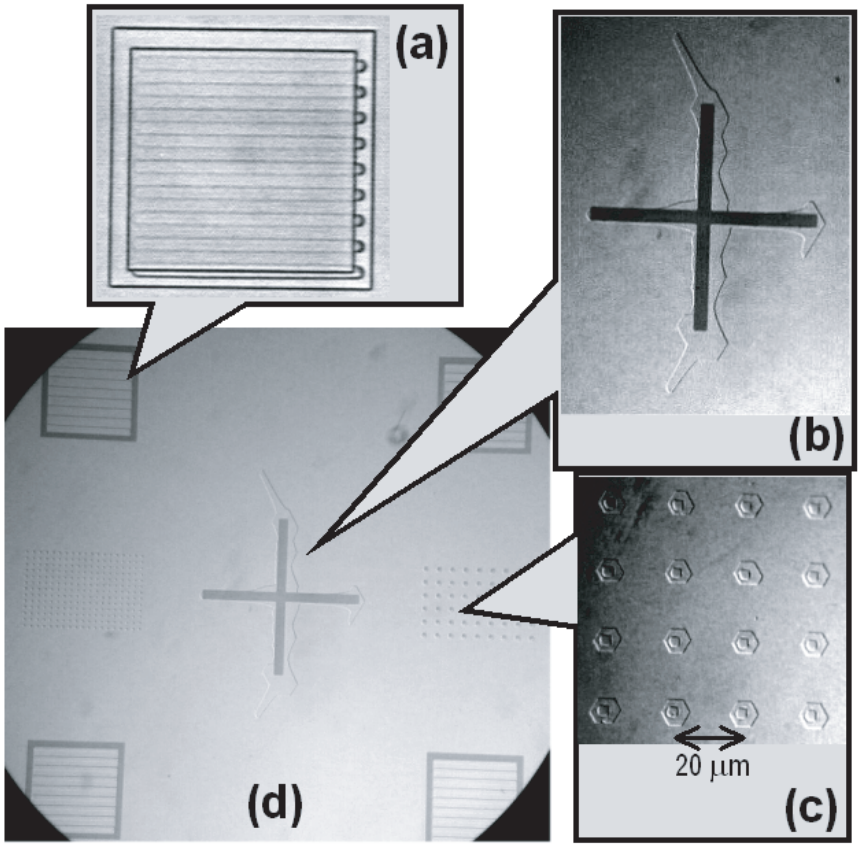

Figure 3.8: A group of poling-to-waveguide alignment structures (d). Features (a), (b), and (c) provide increasing levels of precision.

($\pm 5\mu$m) can be done with traditional cross-hair structures (Figure 3.8b), although the crystalline symmetry of $LiNbO_3$ prevents features with sharp 90° angles. A Y-shaped structure can be poled more accurately, but does not match the axes of the alignment stage. Rather than relying on the fidelity of an individual poling feature, the best alignment markers are arrays of tiny inverted domains, each no more than a few square microns in area. These domains can be registered to corresponding arrays on the waveguide mask with increasing precision as the feature sizes shrink. Figure 3.8c shows square waveguide markers (formed by PE) aligned within hexagon-shaped domains with micron-scale accuracy. Pairs of alignment marks on either side of the mask assure angular alignment better than 100 μrad. Compared to the poling-to-waveguide alignment, alignment of the QPM gratings to the crystalline axes of an unprocessed wafer is less critical. The large $(-y)$ flat of a z-cut wafer can be located through a window in the poling mask. Using this window, the mask can be centered on the wafer to within 500 μm, and oriented with 10 mrad precision.

Before waveguide lithography, the poling features for alignment must be revealed with a hydrofluoric acid etch that attacks $-z$ domains of $LiNbO_3$ 1000 times faster than $+z$ domains. These alignment marks must be in clear focus through the microscope system of the mask exposure tool. For precise alignment, poling markers must be etched onto the waveguide surface of the wafer, rather than the back face. The central region where the waveguides are located can be protected using a double layer of electrical tape and careful application of acid. Before alignment considerations became paramount, etching the entire back face provided both the necessary alignment precision and a routine check on the quality of the periodic poling. This quality check now seems unnecessary and possibly detrimental, since reflections from the structure on the bottom surface during lithography can cause waveguide non-uniformities.

Poling markers also help organize the batch process, providing a convenient method for labelling wafers. A 5-mm × 10-mm section of periodic poling at the edge of every wafer identifies its mask design with a series of letters or numbers visible to the naked eye when illuminated at a grazing angle. This feature prevents errors in mask selection and wafer orientation. The waveguide processing has recently shifted from the $+z$ to the $-z$ face in order to reduce waveguide propagation losses, raising the

potential for confusion. Waveguide losses seem to be 0.05-0.10 dB/cm higher on the $+z$ face, perhaps due to lower polishing quality, or surface damage/contamination from the poling process.

3.6 Improving Waveguide Uniformity

Future improvements to the fabrication process should focus on waveguide uniformity. While the current process is adequate for making standard long doubler devices on 3" substrates, adjustments may be necessary for 4" substrates. Improving waveguide uniformity might also reduce our dependence on the standard non-critical width design, allowing more exploration of the fabrication parameter space. Even in our best devices, minute variations in Δk are revealed by slightly irregular tuning curves.

Whether these variations come from the proton exchange, the annealing, the lithography, or some other sources is unknown. However, several areas are worth investigating. The proton exchange and annealing processes could be better characterized through more in situ temperature profiling with a differential thermocouple. Temperature gradients during heat-up and cool-down may be important in the annealing. While more stirring in the PE bath might flatten its temperature profile, the geometry of the sample fixture may be a limiting factor; so far acid flow seems to have little effect on the exchange rate. Some waveguide non-uniformity is created by the lithography process, due to uneven illumination and contact between the mask and wafer. Stitching errors that cause waveguide width variations and changes in feature size between masks have also been documented. The transparency of $LiNbO_3$ also leads to unwanted reflections within the wafer during exposure. Patterning on the wafer chuck and slight index variations at domain boundaries in PPLN can translate into waveguide width changes. Anti-reflection coatings and photoresists with dye, specially developed for transparent substrates, could be beneficial.

Chapter 4

Integrated OF Mixer Components and Devices

This chapter reviews the development of integrated optical components that are compatible with standard OF mixers. Basic building blocks such as waveguide couplers, junctions, and bends are combined into novel integrated OF mixers. Two examples include an OF balanced mixer and a quasi-group-velocity-matching device.

4.1 Directional Couplers

Many integrated optical circuits require the transfer of optical power from one waveguide to another. This transfer can be accomplished by placing two parallel waveguides close enough together that their modes begin to overlap. The two coupled waveguides will exchange optical power as they propagate over a characteristic distance, L_c. This coupling length can be predicted from basic coupled-mode theory [77]. A waveguide interferometer might use a pair of directional couplers with a 50% coupling ratio as beam splitters. Other coupling ratios can be achieved by adjusting either the strength of the coupling (to change L_c) or the interaction length.

Wavelength-selective filters and combiners can be implemented using directional couplers with a wavelength-dependent coupling ratio. Such a device allows two different wavelengths to be combined in a single waveguide on-chip, avoiding the difficulty

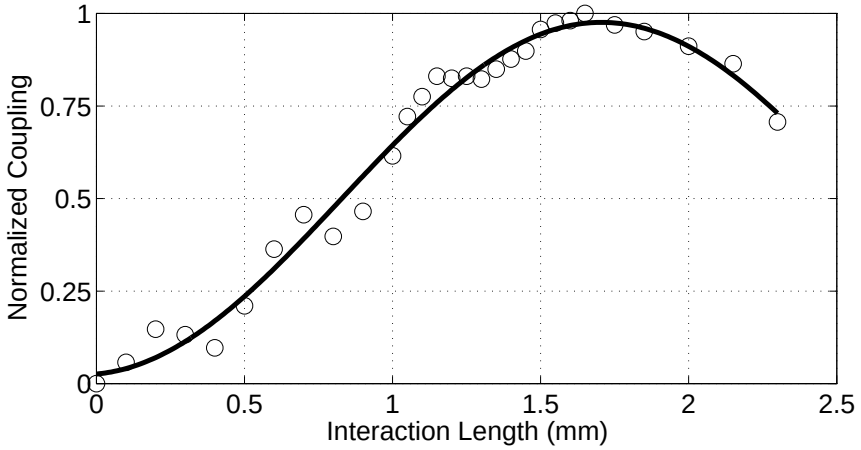

Figure 4.1: Measured coupling versus interaction length for 8-μm waveguides with a 3-μm edge-to-edge separation.

of simultaneously mode matching both waves at the input. This scheme has been demonstrated for DFM with signal and local oscillator waves at 1550 nm and 775 nm [45].

Directional coupler designs for integrated OF mixers have been refined since this proof-of-principle demonstration. Several generations of directional couplers with various waveguide widths and edge-to-edge separations have been explored. A typical measurement of L_c involves fabricating a set of devices with different interaction lengths, and measuring the amount of coupling for each. The devices usually have separate output ports for the coupled and uncoupled waves.

Figure 4.1 shows the expected sinusoidal dependence of the coupling on the interaction length. Each circle represents a unique device from the same $LiNbO_3$ chip, and the coupling ratio is normalized so that unity represents 100% coupling. For this design – based on 8-μm waveguides with a 3-μm edge-to-edge separation – L_c is 1.7 mm at 1550 nm. Some incidental coupling occurs as the waveguides slowly separate after the interaction region. This effect increases the effective interaction length by 0.05 mm, shifting the sinusoidal response along the abscissa.

When using a 100% directional coupler as a FH/SH (first-harmonic/second-harmonic) filter, the SH coupling must be minimized. SH coupling ratios as large as 15% are

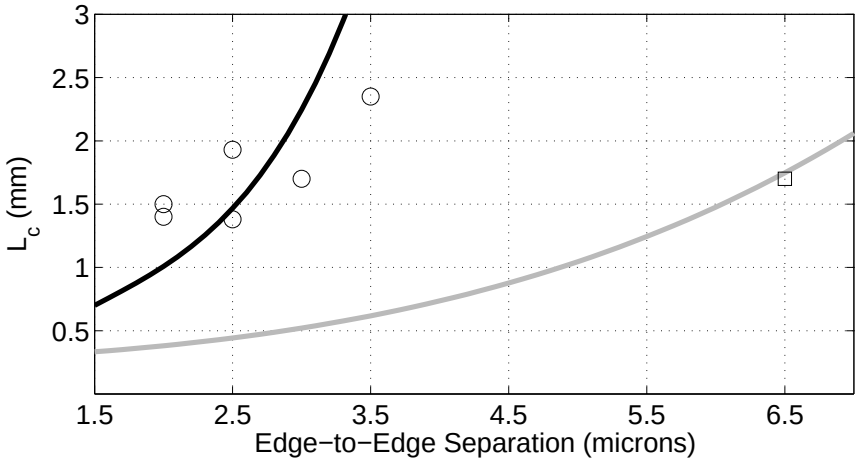

Figure 4.2: Measurements (open markers) and calculations (solid lines) of the 100% coupling length (L_c) versus edge-to-edge separation. The black curve and circular markers correspond to designs using 8-μm-wide waveguides, while the gray curve and square marker correspond to designs using 3-μm-wide waveguides.

measurable in devices similar to those in Reference [66]. Those couplers had 8-μm waveguide widths and a 2-μm edge-to-edge separation. To reduce unwanted SH coupling, the edge-to-edge separation was increased in subsequent coupler designs. This reduces the SH coupling more than the FH coupling because of the tighter confinement of the SH modes, but at the expense of a longer L_c. Experimentally we find that the SH coupling can be reduced below 1% by using a 3-μm edge-to-edge separation and 8-μm waveguides. A somewhat different design (6.5-μm edge-to-edge separation and 4-μm waveguides) can also suppress SH coupling without increasing L_c [71]. In this design larger FH modes (which are closer to cut-off) necessitate a larger edge-to-edge separation.

Careful measurements of L_c validate an improved waveguide fabrication model [61]. Figure 4.2 shows calculations (black line) correctly predicting the dependence of the FH coupling length, $L_{c,FH}$, on the edge-to-edge separation for 8-μm waveguides. Each marker represents a series of measurements like the one in Figure 4.1. A calculation for 4-μm-width couplers (gray line) was used to select a 4-μm/6.5-μm design to match $L_{c,FH}$, 1.7 mm, of the 8-μm/3-μm design. The model also estimates that

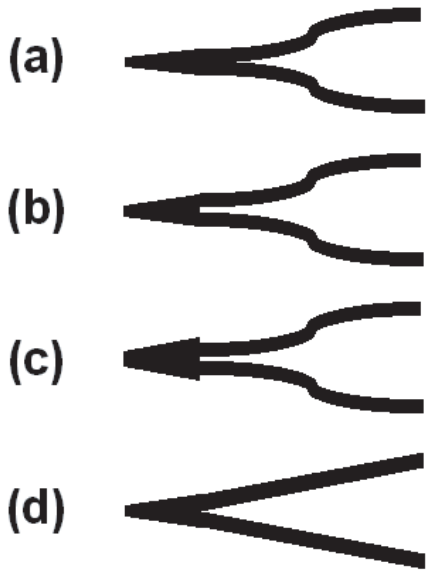

Figure 4.3: Schematic Y-junction designs. Designs (a)-(c) are made from adiabatic tapers and sinusoidal bends, while design (d) uses straight waveguide arms. The branching point defines a sharp corner in (a) and (d), but the feature is smoothed by proton exchange and annealing.

increasing the separation from 2 μm to 3 μm for 8-μm couplers reduces the ratio $\frac{L_{c,SH}}{L_{c,FH}}$ by roughly a factor of 10. SH coupling between higher-order waveguide modes – which can become significant for some designs – can be calculated as well.

While the design of directional couplers is straightforward, in practice, precise coupling ratios are difficult to achieve; this is reflected by the scatter of points in Figure 4.1. In any design, L_c depends critically on the edge-to-edge separation, which can be hard to fabricate with the necessary precision for high-contrast interferometers. Y-junctions are a better choice than directional couplers when trying to achieve an exact 50% splitting ratio.

4.2 Y-junctions

By symmetry, a Y-junction divides power equally into two output branches. Y-junction designs have been studied for a wide variety of material systems [78, 79, 80].

In these systems and in integrated OF mixers, the aim is to minimize both the junction length and its propagation losses.

Simple Y-junctions composed of two raised cosine-shaped bends emanating from an adiabatically tapered waveguide (Figure 4.3a) have proven to be relatively compact with negligible (< 0.1 dB) junction losses at 1550 nm. The adiabatic tapers are crucial because the structure is necessarily two-moded at the branching point [77]. Initial concerns about fabricating the sharp corner where the branch begins – which can be a problem in some non-diffused waveguide systems [81] – led to an investigation of some more blunt designs (Figure 4.3b and c). Both experiments and simulations using Beam Propagation Methods (BPM) [82] show that these designs tend to increase losses because of abrupt changes in the waveguide profile. In APE waveguides, proton diffusion turns a sharp lithographically-defined corner into a gradual transition that adds less than 0.05 dB of loss.

In contrast to directional couplers, Y-junctions are remarkably tolerant to waveguide width variations. For example, a design like the one in Figure 4.3a could be made either using 7-μm and 3.5-μm input and outputs, or using 10-μm and 5-μm input and outputs, without changing the junction losses. Using the mode measurement techniques developed for asymmetric Y-junctions (Section 5.5), we find that even larger designs (e.g., 16-μm/8-μm) eventually suffer from losses due to unwanted coupling into higher-order waveguide modes. In general, it has been helpful to consider the symmetric Y-junction as a special case of the asymmetric Y-junction.

A typical instance of the design in Figure 4.3a might have a total length of 1.5 mm (a 0.5-mm taper and 1-mm bends) and a 50-μm edge-to-edge separation at the output. This design has been used in high contrast interferometers (Section 4.5). A tighter, more efficient bend design (e.g., with a constant slope) could reduce the device length, but not by much; a 1-mm raised cosine bend has a minimum radius of 8 mm, which approaches the lower bound set by waveguide bending losses. These parameters are comparable to a simple Y-shaped design (Figure 4.3d) with a fixed opening angle of 2.8°. Note that the schematic drawings in Figure 4.3 have a compressed aspect ratio for clarity.

4.3 Small-Radius Bends

Small-radius bends are often essential for connecting integrated optical components. Multiple device inputs or outputs require lateral separations of at least 50 μm, while more than 250 μm is necessary for multiple fiber pigtails. The minimum bend radius also limits the minimum device length in Y-junctions and directional couplers. With compact, low-loss bends it is possible to fabricate U-turns, ring resonators, or the quasi-group velocity matching structure described in Section 4.5. We have investigated bending loss versus radius with experiments and modelling in order to design devices.

Analytic expressions for bending loss versus radius exist for a few basic waveguide geometries such as circular fibers, symmetric and asymmetric slabs [83, 84, 77]. The first-order behavior in each case is that the losses increase exponentially with decreasing bend radius ($\alpha \propto \exp(-R)$). Physically, bending losses result from power radiated from the waveguide toward the outside of a bend. In a bend, the waveguide modes shift toward increasing radius, where they can couple more strongly to radiation modes. This picture can be incorporated into an "equivalent straight waveguide" model [85, 86] that approximates the bend using a tilted refractive index profile of the form

$$n_{eq}(x, R) \approx n_0(x)\,[1 + x/R]\,. \tag{4.1}$$

This model can be used to simplify BPM and mode solver calculations that estimate bending losses and the minimum bending radius [82].

Figure 4.4 compares a BPM calculation (solid line) with loss measurements on a series of bent waveguide of varying radius (open markers) at 1550 nm. The model accurately predicts that for 8-μm-wide waveguides, which have relatively small FH modes, propagation losses increase dramatically for radii below 3-4 mm. The model tends to overestimate bending losses, possibly due to inadequate meshing. The waveguides under test had raised-cosine S-bends with amplitudes of 2.0 mm and 2.5 mm (circle and square markers). Experiments show that larger (e.g., 13-μm-width) waveguides can guide power through tighter bends, but with significant higher-order mode conversion.

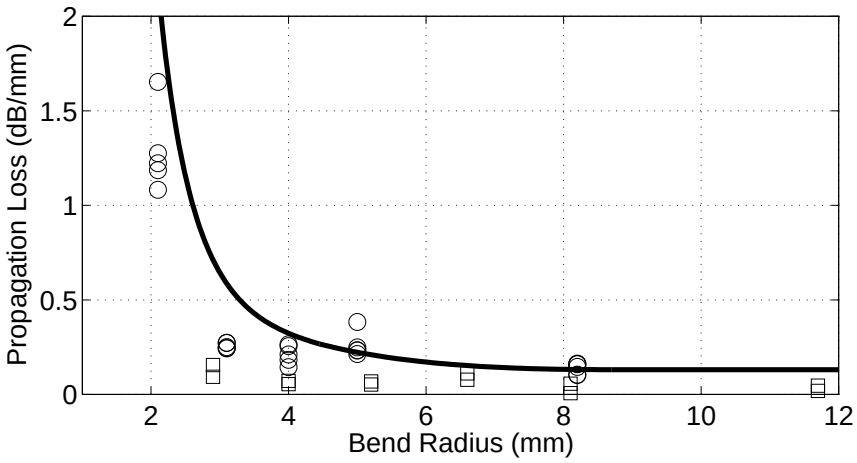

Figure 4.4: Calculated and measured propagation losses versus bending radius in 8-μm waveguides at 1550 nm.

A 4-mm bend radius is small enough for a majority of integrated OF mixer applications. In extreme cases, such as U-turns or ring resonators, smaller radii might be needed to fit multiple devices on centimeter-wide chips. Ongoing work to reduce the minimum bend radius is focusing on ways to tailor the refractive index profile for greater mode confinement through a bend. Possibilities include trying to lower the index at the outside edge of a waveguide bend by etching a half-ridge waveguide structure, or by raising the index at the inside edge by using a laterally-graded proton exchange profile. Waveguide bends will also be useful as "ω-removers" that discard the FH wavelength while keeping the SH (at 2ω), since bending losses increase dramatically with wavelength and mode size.

4.4 The Optical-Frequency Balanced Mixer

With suitable designs for waveguide couplers, junctions, and bends, it is possible to create novel integrated OF mixers based on interferometer structures. The OF balanced mixer [87] is one important example. The balanced mixer solves the distinguishability and spatial separation problem (Section 1.4) using a waveguide interferometer to separate the mixer output from the residual pump and signal. This

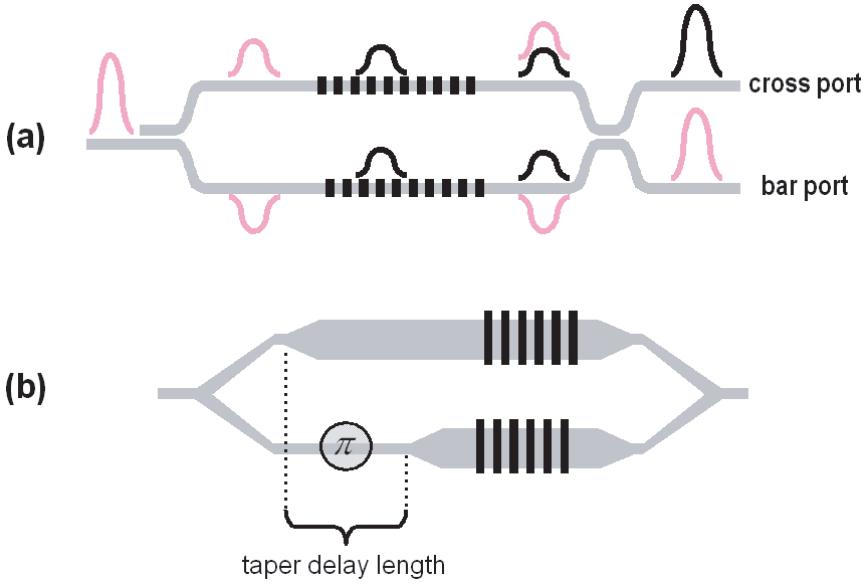

Figure 4.5: (a) OF balanced mixer structure using directional couplers. The input (pump and signal) waves (gray) exit through the bar port, while a π-phase shift between the gratings in each arm biases the mixer output (black) for cross port transmission. (b) Schematic drawing of the demonstration device using Y-junctions; the taper delay length adjusts the relative phase (ideally π) between the arms.

separation enables bi-directional wavelength conversion and spectral inversion without wavelength offset in all QPM signal-processing devices.

In contrast to noncollinear and two-dimensional QPM schemes [88], the OF balanced mixer spatially separates the nonlinear output while using a collinear interaction section for high efficiency. The OF mixer achieves this separation in a single stage, without resorting to intermediate filtering [89]. The analogous functions have been demonstrated in four-wave mixing devices using a parametric loop mirror configuration with asymmetrically placed dispersive elements [90].

The OF balanced mixer is the optical analogue of the RF balanced mixer [91]. An appropriately biased interferometer structure suppresses the residual signal and pump waves, while the flexibility of QPM allows the mixer output to be biased independently. Figure 4.5a illustrates this idea in a Mach-Zehnder configuration with two 50% directional couplers and two output ports. The interferometer is biased so that

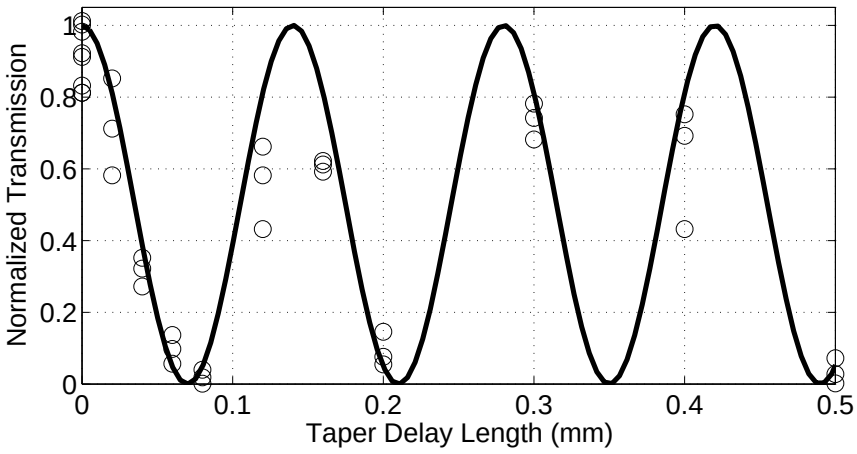

Figure 4.6: Measured transmission versus taper delay length in a series of balanced mixer devices.

the input signal and pump waves (gray) are transmitted through the bar port. The mixing that occurs in the periodically poled sections (represented by gratings) has no effect on the phase of the input waves in the phase-matched, non-pump-depleted case. The phase of the mixer output generated in each arm (black), however, is set by the phases of the input waves and by the phase of the grating. A π-phase shift between the two gratings aligns the phases of the output in each arm. With this bias, the mixer output exits through the cross port, conveniently separated from the residual input. The efficiency penalty for using two parallel interaction sections – each containing one half of the input signal and pump – is that the OF balanced mixer requires twice as much pump power as a standard device for the same level of performance.

For a proof-of-principle demonstration of the balanced mixer function, we fabricated devices using Y-junctions instead of directional couplers (Figure 4.5b) to ensure a 50% splitting ratio. In this case an additional π-phase shift is required in one arm to discard the pump and signal at the output; the residual inputs end up in an unguided antisymmetric radiation mode at the output port, while the mixed output appears as the TM_{00} mode at the (single-moded) output port. Transmission measurements use a butt-coupled single-mode fiber as an output coupler to filter the weak device

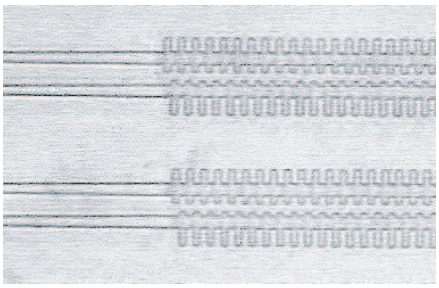

Figure 4.7: Alignment of π-phase shifted 35-μm-wide gratings and 12-μm-wide waveguides in two balanced mixer devices.

transmission at π-phase bias from the rejected input.

To create the π-phase shift, we exploited the difference in effective index between a narrow and a wide waveguide. In each interferometer arm, the QPM mixing section is 12-μm wide, as in the standard long doubler. The 3.5-μm-wide branches of the Y-junction connect to these mixing sections through an adiabatic taper. Delaying the onset of this taper produces a relative phase shift between the interferometer arms (Figure 4.5b). Since this phase shift is not dynamically adjustable, we fabricated many balanced mixer devices with various taper delay lengths to explore a full range of interferometer bias points. Absolute transmission measurements for devices with taper delay lengths ranging from 0 to 500 μm yield the normalized interferometer contrast curve shown in Figure 4.6. Each data point represents a unique device. From these measurements, it appears that the taper delay length needed for a π-phase shift is ≈ 70 μm.

Figure 4.7 shows π-phase-shifted gratings (35-μm-wide, 14.75-μm-period) aligned to 12-μm-wide waveguides; both the poling and waveguides are destructively etched for visibility. Their fabrication and alignment depended on some of the improved techniques described in Chapter 3.

In this proof-of-principle demonstration of the balanced mixer, the interaction sections were shortened to loosen fabrication tolerances at the expense of lower mixing efficiency. Only the length-normalized efficiency was important for these initial

devices, since the goal was to establish their novel functionality. The 23-mm-long devices had interferometer arms with only 12-mm-long periodically-poled sections, and were ≈2500 times less efficient than a standard OF mixer for cascaded SHG and DFM because of the fourth-power length scaling described in Section 2.2.5. The normalized efficiency, 52%/W·cm^2, was equivalent to that of standard APE OF mixers.

The measured contrast – the amount of residual pump and signal rejection – was greater than 13 dB in the initial balanced mixer devices. More recently, interferometer structures with greater than 20 dB of contrast (Section 4.5) have been created, following improvements in the fabrication process. Note that the interferometric sensitivity of the balanced mixer places even more stringent tolerances on the waveguide fabrication than the quasi-phasematching does. Given the current state of commercially available Mach-Zehnder modulators, using a DC bias it should be possible to achieve up to 30 dB of contrast [54]. An alternative, non-interferometric scheme for accomplishing the same function with considerably looser fabrication tolerances is described in Section 5.6.

4.5 Quasi-Group Velocity Matching

An interferometer-like structure based on directional couplers and small radius bends can be used for another completely different application: raising the speed limits of OF mixers. While OF mixers are among the fastest optical signal processing devices available today, they have speed limits set by group velocity mismatch [92] between the interacting FH and SH waves. Standard OF mixers are based on DFM between a FH wave (a 1550-nm signal) and a SH (775-nm) local oscillator. With a CW local oscillator, over 1 THz of conversion bandwidth is available. In a gated mixer, however, the SH local oscillator (or clock) consists of short optical pulses. At high enough speeds, the device fails when the envelopes of the FH and SH pulses "walk off" each other into neighboring time slots as they propagate through the device. Thus group velocity mismatch limits the maximum interaction length for short pulses, resulting in reduced efficiency. For 100 Gbit/s pulses in a PPLN OF mixer, the maximum

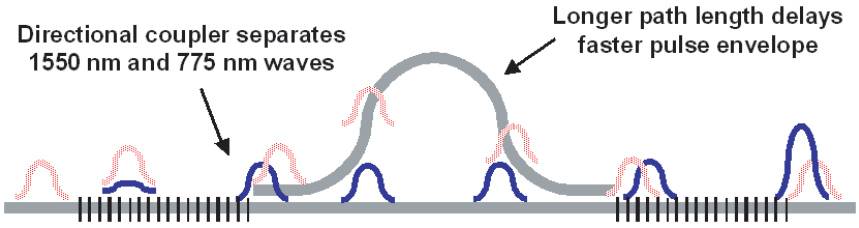

Figure 4.8: GVM compensation scheme: after one SHG interaction length (gratings), a large bend is used to delay the input FH wave (gray) which has a faster group velocity relative to SH. The pulses are resynchronized and interact a second time, augmenting the SH pulse.

interaction length is $\approx$ 3 cm, about half that of a standard device. Although a 3-cm QPM grating can still provide sufficient conversion efficiency (down to pJ pulse energies), we aim to obviate this speed/efficiency trade-off entirely with a quasi-group-velocity-matched structure.

The group velocity mismatch (GVM) compensation scheme uses directional couplers and a small radius bend to re-synchronize the pulse envelopes of a faster FH pulse and a slower SH pulse (Figure 4.8). After a first conversion section (shown as a grating), the leading FH pulse (gray) is selectively coupled into a parallel waveguide, delayed by a large bend, and then coupled back to overlap with the SH pulse (black), augmenting it in the second conversion section. This structure doubles the effective interaction length for the pulses. Consequently, a SHG device would require four times less peak power, and a cascaded SHG:DFM device would require 16 times less peak power. Higher efficiencies could be obtained without sacrificing bandwidth by iterating the structure. A single compensation stage would be appropriate for 100 Gbit/s pulses in a standard-length OF mixer; this device would require a U-shaped bend with a 3-mm amplitude, given a 4-mm radius of curvature.

We are close to demonstrating a single-stage quasi-group-velocity-matched device for 100 fs pulses, having developed all the necessary components. These include low-loss small radius bends, directional couplers that selectively couple FH from SH waves, and the precise positioning of QPM grating adjacent to the couplers. The relative phase of the two grating sections, essential for correct operation, can be

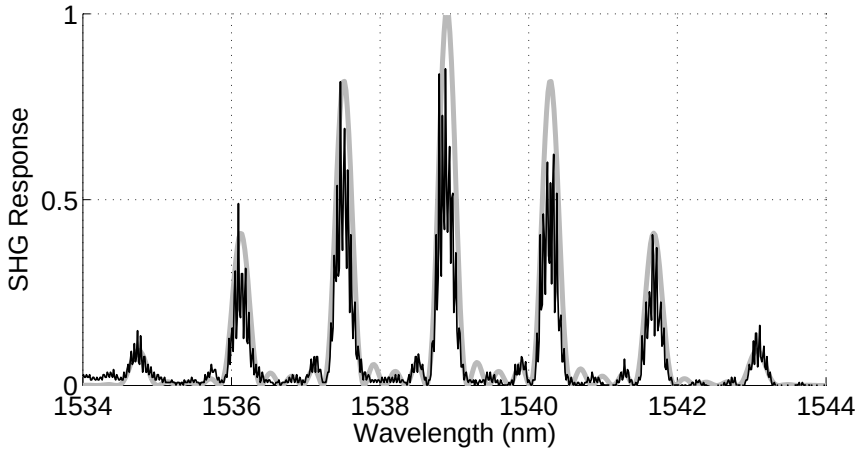

Figure 4.9: Measured and calculated SHG response of a device with segmented QPM gratings; the periodicity yields a precise value for $\delta\nu$.

adjusted by tuning the device temperature (and the phasematching wavelength) in a proof-of-principle device. In a more advanced device, this tuning could be done electro-optically.

The groundwork for this project has included a precise measurement of the group velocity mismatch parameter, $\delta\nu = 1/v_\omega - 1/v_{2\omega}$. SHG tuning curves of devices with segmented (along the z-direction) QPM gratings provide a convenient measure of $\delta\nu$ in the frequency domain. Segmentation with millimeter-scale periodicity Λ_s adds low spatial-frequency components to K_{QPM} that modulate the SHG wavelength-response on a nanometer scale. The frequency spacing Δf of the SHG tuning curve peaks relates to the group velocity mismatch by $\delta\nu = 1/(\Delta f\, \Lambda_s\, n_{eff})$. Segmented or phase-reversed QPM gratings have been used to modify the frequency response of DFM devices [31], and (from a time-domain perspective) to shape ultra-fast pulses using group velocity walkoff [93].

Figure 4.9 shows the SHG response (black line) for a typical device with 2-mm QPM grating segments separated by 6 mm ($\Lambda_s = 8$ mm). From the 1.39-nm modulation period of this tuning curve, we infer that $\delta\nu \approx 0.354$ ps/mm at 1540 nm. The calculated tuning curve (gray) is based on this value, which is slightly larger than the bulk value 0.30 ps/mm, as expected. Although Fabry-Perot effects add high

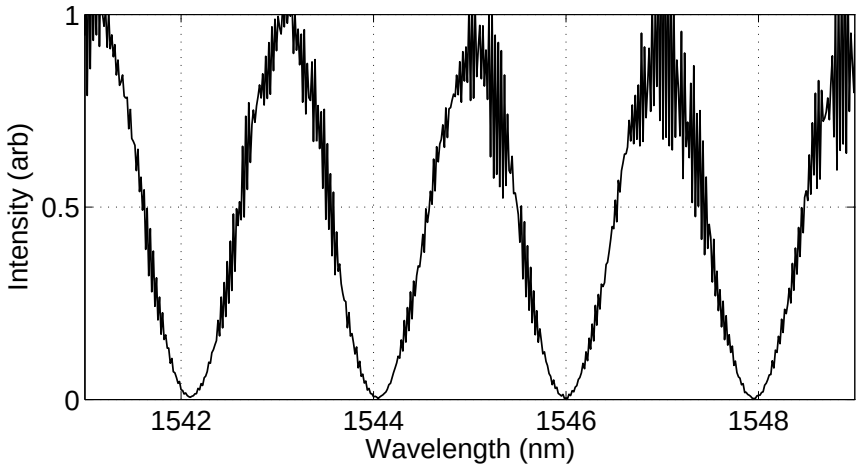

Figure 4.10: Measured transmission of a 20-dB-contrast Mach-Zehnder interferometer with a 0.55-mm path-length difference between its arms.

frequency fringes to the measured SHG response, $\delta\nu$ depends only on the overall periodicity. Testing the same device with ultrashort pulses would result in a pulse train that could be characterized in the time-domain using a cross-correlator.

In another preliminary test, we used a massively unbalanced Mach Zehnder interferometer to verify that large path length differences can be fabricated with high precision. The device structure is similar to that of the quasi-GVM device itself except that Y-junctions replace the directional couplers. The result is a high contrast ($>$ 20 dB) interferometer whose path length difference – programmed to be 0.55 mm in this case – allows the bias point to be adjusted between 0 and 2π by tuning the input wavelength by only 1.98 nm (Figure 4.10). The fringe period shown in these transmission versus wavelength measurements, combined with a calculation of n_{eff}, exactly match the designed path length difference. The n_{eff} value can also be checked against the 10 pm (50 GHz) Fabry-Perot fringe spacing (not resolvable in this figure). This successful measurement, along with the accurate value for $\delta\nu$, make us confident that we can demonstrate quasi-group velocity matching in the near future.

4.6 Future Components and Devices

A variety of additional integrated OF mixer components and devices are under development; this section presents a few examples. Electro-optic QPM waveguides devices are being fabricated by coating standard devices with a 2000$\mathring{A}$ layer of spin-on glass and depositing gold electrodes. The electro-optic effect can be used to tune the phase-matching wavelength [94, 95], or to create sharp index steps at domain boundaries in bulk or planar waveguide devices. Using asymmetric gratings (Section 5.3) and mode sorters (Section 5.4), electro-optic switches based on TM_{00} to TM_{10} mode conversion would be possible.

Fine control over the size, position, and alignment of periodic poling makes it possible to amplitude modulate QPM gratings. Deliberate misalignment of narrow gratings and waveguides can reduce the efficiency overlap integral (2.16) in a controlled fashion. Domain widths smaller than the waveguide width would have the same effect. With precision fabrication, a desired amplitude profile could be programmed. This type of amplitude modulation is orthogonal to schemes using duty-cycle variations, and could complement newly developed phase modulation techniques [96]. Amplitude modulation is essential for creating flat-topped tuning curves without side-lobes.

Gated mixers have been used for optical TDM of eight 20 Gbit/s channels onto a single 160 Gbit/s channel [1]. The operation of these devices, which use standard OF mixers, is shown schematically using four channels in Figure 4.11. Each signal channel mixes with a different phase of a clock/pump pulse in four separate, straight waveguides. The short duty cycle of the clock pulses allows the mixer outputs to be combined onto a single channel at four times the original clock speed. Silica-on-silicon planar lightwave circuits (portions shown in dashed rectangles) are used to divide, distribute, and recombine the optical clock and signals. These circuits are butt-coupled to both ends of a standard OF mixer device (shown within the solid rectangle).

Integrated OF mixers will enable novel TDM functions without the use of additional silica-on-silicon waveguide circuitry. A gated mixer that performs optical WDM-to-TDM conversion is under development. GVM pulse shaping techniques can

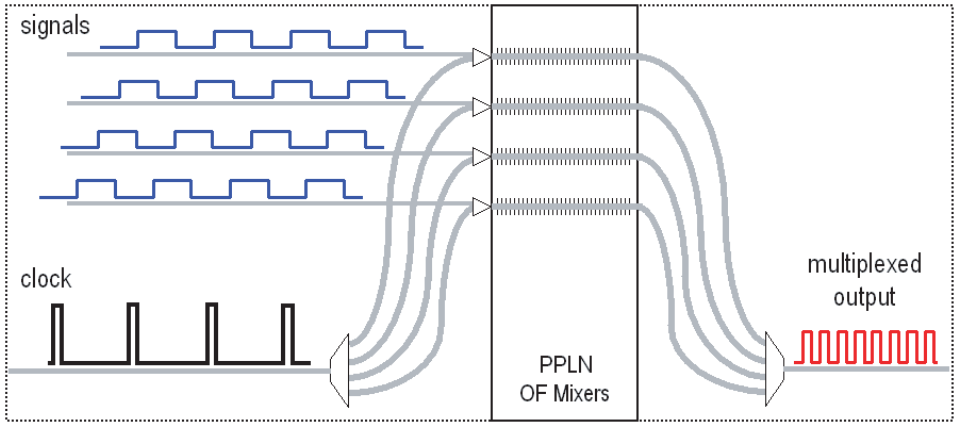

Figure 4.11: Schematic operation of the optical TDM device described in Reference [1]. Four signal channels mix with four phases of a clock/pump in standard PPLN waveguides (contained within the solid rectangle). The short duty cycle of the optical clock allows the mixer outputs to be combined onto a single channel at four times the original clock speed. The division, distribution, and recombination of the pump and signals occur in silica-on-silicon planar lightwave circuits (within the dashed rectangles).

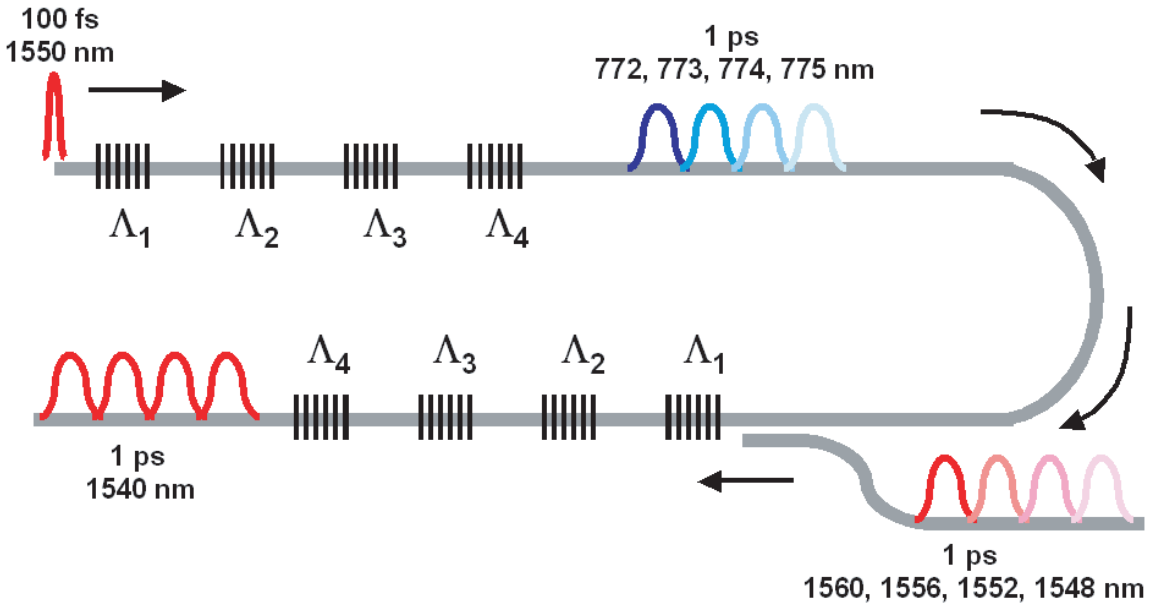

Figure 4.12: Schematic operation of an optical WDM-to-TDM converter based on GVM pulse shaping techniques.

be used to synthesize a multi-color SH pulse train by SHG (Figure 4.12) that can serve as a multi-phase clock for such a device. A 100-fs FH pulse would have enough bandwidth to create a train of ps-pulses at the SH with slightly different wavelengths, using a set of gratings with slightly shifted Λ_g. Such a pulse train would be useful for multiplexing WDM signals onto a single wavelength channel by DFM between the appropriate signal and clock wavelengths. In Figure 4.12 the generated clock pulses are combined with the input WDM signals using a U-turn bend and a wavelength-selective directional coupler. The TDM output channel has four times the repetition rate of the original WDM signals. The same device would function as a TDM-to-WDM demultiplexer if the input signal consisted of a single-color FH pulse train. All of the timing in WDM-TDM converters can be set lithographically once $\delta\nu$ is known. These optical TDM schemes are potentially much more efficient than one shown in Figure 4.11, because the pump power is no longer split among all the channels.

Chapter 5

Mode Multiplexing in Integrated OF Mixers

5.1 Introduction

Higher-order waveguide modes provide a new solution to the problem of distinguishing and spatially separating the interacting waves in OF mixers (introduced in Section 1.4). In a standard waveguide OF mixer, all the interacting waves propagate in the lowest-order, TM_{00} mode. Mixing in a quasi-phasematching (QPM) grating section produces a wavelength-converted output E_{OUT}, which can be separated from the pump and residual inputs (E_P and E_S) by spectral filtering (Figure 5.1a). In bi-directional wavelength conversion or spectral inversion without offset, however, the input and output contain the same wavelengths, making them impossible to distinguish, let alone separate spatially. Generating output waves in higher-order waveguide modes can solve this problem. As shown in Figure 5.1b, TM_{00} mode input waves E_P and E_S can mix to produce a TM_{10} mode output wave, E_{OUT}. The mixer output can then be separated from the residual input by filtering the two modes using integrated-optic structures or a single-mode fiber.

This mode multiplexing scheme rests on two new integrated OF mixer components. Angled and staggered QPM gratings are needed for efficient mixing between fundamental and higher-order modes. Secondly, asymmetric Y-junctions can be used

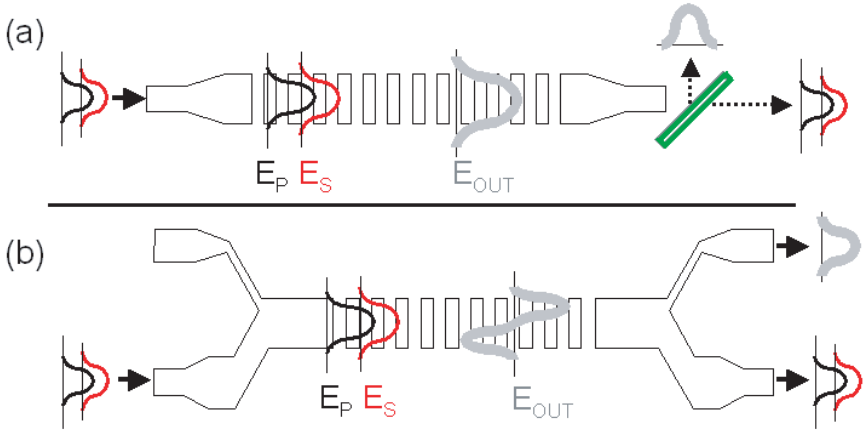

Figure 5.1: Conventional QPM waveguide mixing and filtering (a) versus odd-even mode mixing and sorting (b).

as mode sorters and converters. Conveniently, the output junction in Figure 5.1b not only filters out the TM_{10} mode, but also converts it into a more useful TM_{00} mode. This chapter presents the development of these components and examples of their use in higher-order mode QPM mixing devices. Section 5.6 describes an odd-to-even mode wavelength converter suitable for bi-directional wavelength conversion or spectral inversion without offset. These devices are the first examples of a new class of OF mixers that utilize higher-order waveguide modes for signal processing [97].

5.2 Higher-Order Mode QPM Mixing

Although fundamental modes generally provide the best mode overlap and mixing efficiency, higher-order modes have always occupied a place in waveguide nonlinear optics. Before the advent of QPM mixers, higher-order mode interactions were used to satisfy the phasematching requirement [98]. More recently, engineering the depth dependence of the nonlinear coefficient has improved mode overlap efficiency in thin-film waveguides [99] and in QPM channel waveguides with nonuniform domain inversion [60]. Here we demonstrate high-precision QPM structures with transverse patterning optimized for efficient mixing between higher-order width modes.

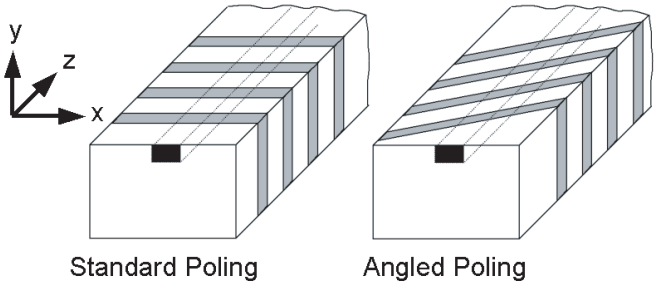

Figure 5.2: Coordinate system and geometry for standard and angled QPM gratings and waveguides.

Switching from fundamental modes to higher-order modes in an OF mixer can alter the mixing efficiency dramatically. At the same time, the QPM grating period changes little since the material dispersion outweighs the waveguide dispersion. The nonlinear mixing efficiency η is proportional to the spatial overlap integral of the nonlinear coefficient, the phasematched Fourier component of the QPM grating, and the normalized field modes introduced in equation (2.2).

$$\eta \propto \left| \int_{-\infty}^{\infty} \int_{-\infty}^{\infty} \bar{d}(x,y)\, G_m(x,y) \tilde{E}_{1,jk}(x,y) \tilde{E}_{2,lm}(x,y) \tilde{E}^*_{3,np}(x,y)\, dx\, dy \right|^2, \qquad (5.1)$$

where we have rewritten equation (2.19) to include lettered subscripts on the field modes that denote width and depth mode numbers. In this coordinate system, (x, y) are the waveguide width and depth directions, transverse to the propagation direction, z. For the common case of SHG using a TM_{00} mode first-harmonic (FH) wave, $E_{1,00} = E_{2,00}$ in relation (5.1). To simplify the notation, we refer to this mode as FH_{00}. In the next section, we demonstrate odd and even mode SHG of FH_{00}, producing both the fundamental and the first higher-order width modes of the second-harmonic (SH) wave: $E_{3,00}$ and $E_{3,10}$, or simply, SH_{00} and SH_{10}.

QPM grating fabrication techniques, such as electric-field poling of ferroelectrics, often yield structures in which the nonlinear coefficient and G_m are constant over the extent of the waveguide. With these standard gratings, odd SH modes cannot be produced from even FH modes due to the symmetry of the coupling coefficient in

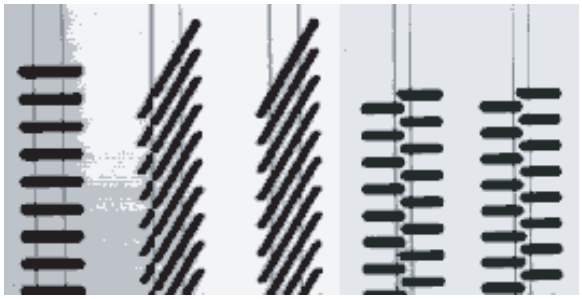

Figure 5.3: Standard, 60°-angled, and staggered QPM gratings (15-μm-period, 35 and 50 μm in width) aligned to waveguides and etched for visibility.

relation (5.1); two even modes mixing with an odd mode under an even d and G_m have a null efficiency overlap integral. For standard channel waveguides – and all waveguides with symmetric and antisymmetric width modes – SHG of FH_{00} cannot produce SH_{10} unless the symmetry in x is broken.

Modified QPM gratings can alter the symmetry of $G_m(x)$, enabling mixing of odd and even width modes [100]. Angled gratings that are tilted with respect to the waveguides (Figure 5.2) give the Fourier amplitude G_m an x-dependent phase $\phi = 2\pi x \tan\theta/\Lambda_g$, where θ is the grating angle with respect to x, and Λ_g is the QPM period. As a result, G_m is neither even nor odd, and both types of modes can be generated. Staggered gratings – nearly interleaved gratings with a π-phase shift at the center of the waveguide – make G_m fully antisymmetric in x [101], and are optimal for producing the two-lobed TM_{10} mode. Note that while altering the symmetry of G_m can assure nonzero efficiency for odd-even mode mixing, this efficiency is still proportional to the mode overlap. In general, using higher-order modes rather than the fundamental modes in symmetric waveguides degrades mode overlap because of the additional minima in the field modes.

5.3 SHG with Angled and Staggered Gratings

Using the standard process, we fabricated OF mixers with angled and staggered gratings for generation of SH_{10} from FH_{00}. Gratings angled at 60° to x are easily

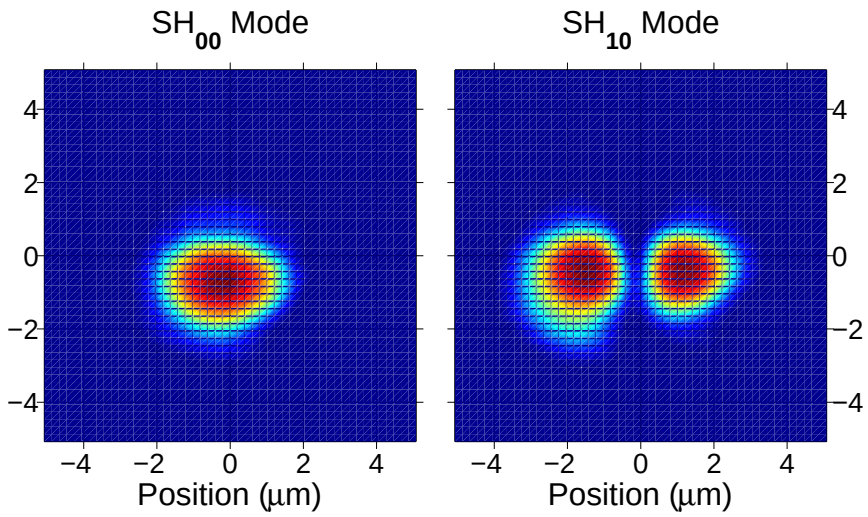

Figure 5.4: CCD camera images of SH_{00} and SH_{10} modes.

produced because of the hexagonal domain structure of congruent lithium niobate. Using narrow (as measured perpendicular to the k-vector) stripes, we also fabricated nearly ideal staggered gratings by accounting for the domain spreading along x during poling. Figure 5.3 shows standard, angled, and staggered gratings (15-μm period, 35 and 50-μm in width) precisely aligned to waveguides and etched for visibility. The etching enlarges and rounds the edges of the inverted domains slightly. These devices were similar to standard OF mixers, but had QPM periods of 14.75 – 16.75 μm, and waveguide widths ranging from 8 to 20 μm. For each waveguide width, we found the appropriate grating period for doubling 1550-nm light using our waveguide fabrication model [61] and mode solver to calculate the effective indices of all the modes. The mode solutions also include the field mode shapes, which can be used to predict the mixing efficiency for each design from (5.1).

SHG measurements using 20 mW of FH_{00} power demonstrate efficient generation of both the SH_{00} and SH_{10} modes. CCD images of both modes in 8-μm waveguides (with different QPM periods) are shown in Figure 5.4; in the shading scheme used, the highest and lowest intensity points appear black. Normalized conversion efficiencies as high as 400%/W and 220%/W for the SH_{00} and SH_{10} modes, respectively, were

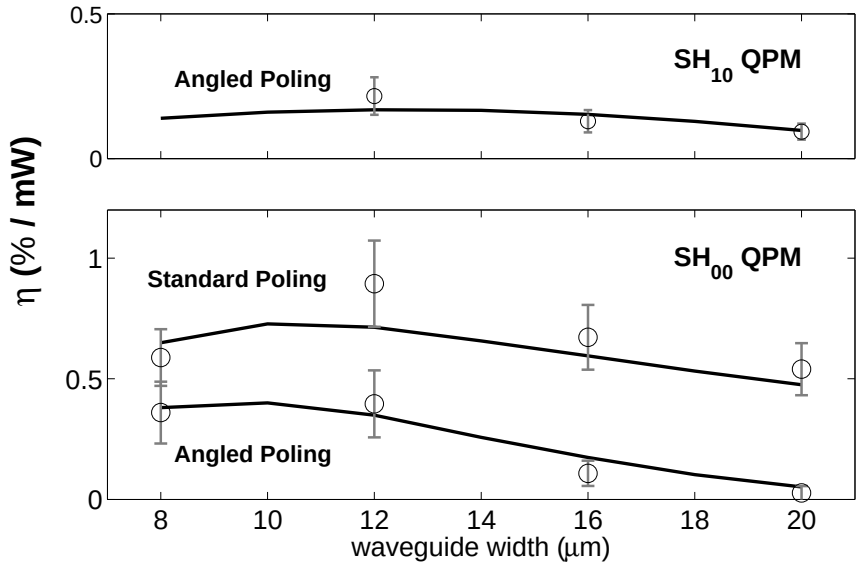

Figure 5.5: Measured (circles) and calculated (lines) SHG efficiencies for SH_{00} and SH_{10} modes for 60°-angled and standard poling, for a range of waveguide widths.

measured in devices with 4-cm-long angled gratings. With standard gratings, only the SH_{00} mode could be produced (900%/W efficiency), as expected. Figure 5.5 compiles measurements (represented by open circles) of the SHG efficiency for both modes (using 60°-angled and standard gratings) for a wide range of waveguide widths. The calculated efficiencies (solid lines) are consistent with the measured values for both modes for all the waveguide widths tested.

The staggered grating devices, which have the most stringent alignment tolerances between the periodic poling and the waveguides, showed approximately half the expected SH_{10} mode generation. Mode overlap calculations indicate that this reduction is consistent with a misalignment in x (assuming perfect angular alignment and device geometry) of ≈ 1.0 μm. A vernier-like system of deliberate misalignments could compensate for fabrication errors in future devices. Non-zero generation of the SH_{00} mode also indicated poling-waveguide misalignment, since staggered grating devices should only generate odd modes. Figure 5.6 compares calculated SHG efficiencies for all three poling types, for the range of waveguides fabricated in this study. An ideal staggered poling device should have roughly twice the SH_{10} efficiency of a 60°-angled

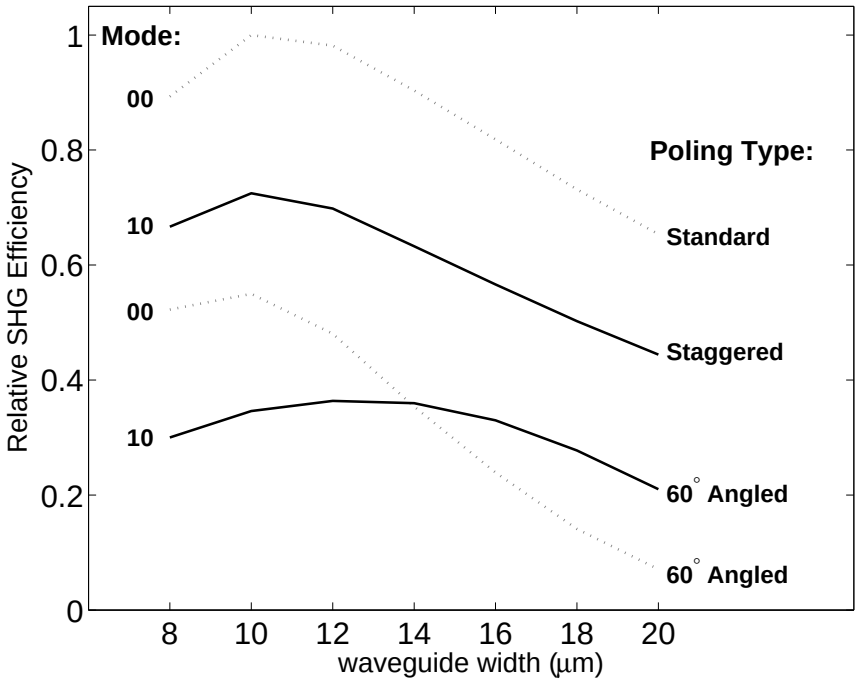

Figure 5.6: Calculations of the expected relative SHG efficiencies of standard, 60°-angled, and staggered poling for a range of waveguide widths. SHG of SH_{10} (from FH_{00}) with ideal staggered gratings should have $\approx 70\%$ of the efficiency of the standard SH_{00} process.

Table 5.1: The calculated mixing efficiency and grating period for various SHG interactions between higher-order FH and SH modes in a 12-μm-wide waveguide.

	FH	FH	SH	Λ_g (μm)	η_{standard}	η_{angled}	$\eta_{\text{staggered}}$
a	00	00	00	14.78	100	43.8	–
b	00	00	10	15.53	–	39.1	71.3
c	00	00	20	16.42	0.4	10.3	–
d	00	10	00	14.20	–	16.2	28.5
e	00	10	10	14.89	47.8	0.9	–
f	00	10	20	15.70	–	17.6	19.6
g	10	10	00	13.66	19.3	0.0	–
h	10	10	10	14.29	–	34.4	52.3
i	10	10	20	15.05	49.6	8.3	–
j	10	20	30	15.29	26.9	5.8	–
k	20	20	40	15.53	24.3	9.5	–

poling device, and $\approx 70\%$ of the SH_{00} efficiency of a standard poling device. These results show that odd-even mode mixing can have efficiencies comparable to standard 00-mode mixing.

Angled and staggered gratings permit QPM interactions between odd and even modes of waveguides symmetric in x. PPLN waveguide modes are not symmetric in y, however. The annealed proton exchange process creates asymmetric depth profiles for the refractive index and the nonlinear coefficient $d(y)$ [102, 60]. Consequently, SHG of SH_{01} modes (higher order in depth) is possible with a FH_{00} input [103, 104]. In similar fashion, modified gratings could complement PPLN waveguides with x-asymmetry for efficient generation of asymmetric width modes.

Control over the symmetry of G_m with modified gratings adds flexibility in choosing which waveguide modes will interact in an OF mixer. Table 5.1 lists the calculated SHG/SFG efficiency and grating period for various interactions between higher-order modes in a 12-μm-wide waveguide. The efficiencies – shown for standard, angled, and staggered QPM gratings – are normalized to the standard long doubler process (a). While some combinations are forbidden by symmetry, many have efficiencies comparable to the TM_{00} mode process.

In most cases, Table 5.1 underestimates the maximum mixing efficiency, which is a strong function of the waveguide width (e.g., see Figure 5.6) as well as the wavelengths involved. However, despite these missing variables, the table still suggests the variety of additional odd-even mode combinations enabled by angled and staggered QPM gratings. The overlap integral can also be adjusted by changing the grating angle; any angle between 0° and 90° is possible using bent waveguides. Fortunately, in many cases 60° turns out to be nearly optimal.

Processes a and b were investigated in this section, while a, e and i – which require similar grating periods – are used in mode content measurements (Section 5.5). Together, a-i include all possible interactions between the first two FH modes and the first three SH modes. The last two combinations, j and k belong in the same "family" as a, e and i. All of the processes in this family are relatively efficient, use symmetric gratings, and have similar QPM periods because the FH and SH mode numbers are incremented in parallel.

5.4 Mode Sorters and Converters

This section introduces mode sorting and converting structures for integrated OF mixers. Mode multiplexing devices like the one in Figure 5.1 depend not only on efficient mixing between higher-order modes, but also on efficient manipulation of these modes using linear optical components like asymmetric Y-junctions.

Asymmetric Y-junctions consist of two waveguides that have unequal widths at their branching point. Launching into the narrow "odd port" of an asymmetric Y-junction converts a TM_{00} mode into a TM_{10} mode, while launching into the wider "even port" leaves the mode unchanged (Figure 5.7). Viewed in the opposite propagation direction, the junction acts as a TM_{00}-mode/TM_{10}-mode sorter; both propagation directions offer valuable functionality. The sorting behavior occurs when the branches separate gradually enough that their modes evolve adiabatically, remaining local normal modes throughout the structure. The modes of the larger and smaller input branches evolve into the first and second modes of the combined junction, respectively. As the modes evolve, the hierarchy of their effective indices remains fixed.

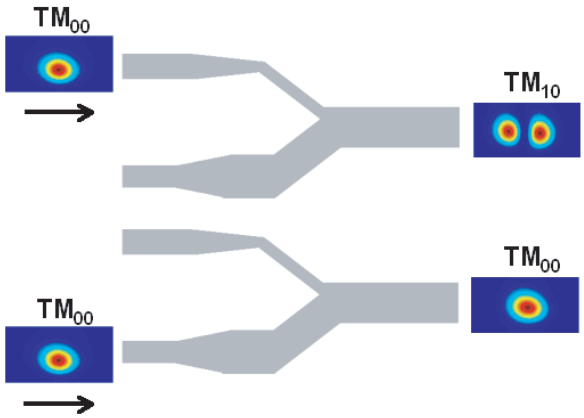

Figure 5.7: Mode sorting behavior in an asymmetric Y-junction. Launching into the narrower (odd) port converts the TM_{00} mode into a TM_{10} mode, while launching into the wider (even) port leaves the TM_{00} mode unchanged.

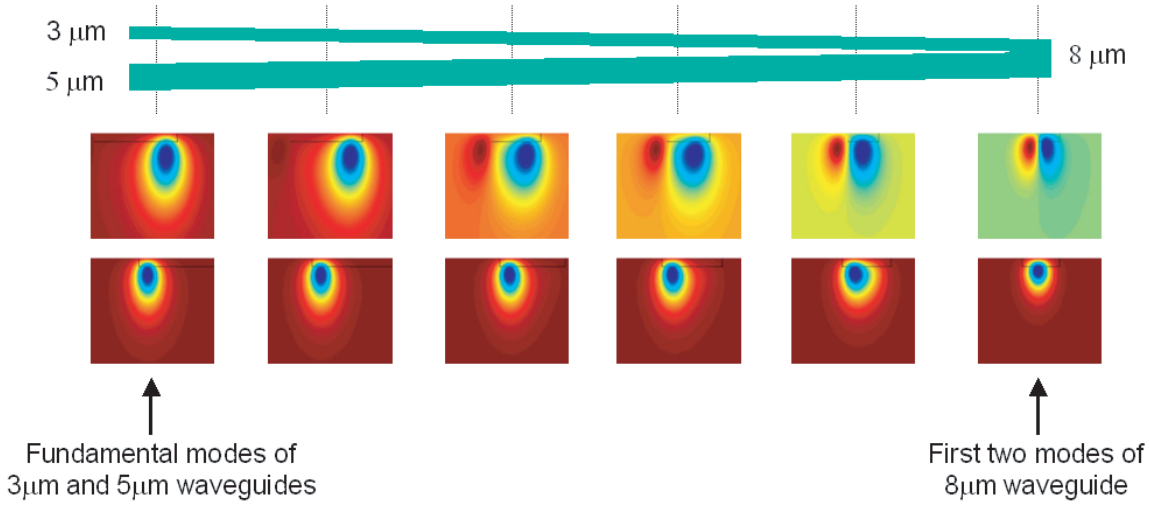

Figure 5.8: Mode evolution in an asymmetric Y-junction formed by 3-μm and 5-μm waveguides that join in an 8-μm waveguide. Calculated mode shapes are shown for two-dimensional slices of the structure taken at the indicated locations.

The mode converting properties of asymmetric Y-junctions have been known for decades [105, 106]. Most recently, asymmetric Y-junctions have been used to make high contrast optical switches in polymer [107] and lithium niobate waveguides [108]. These active devices, sometimes referred to as "digital optical switches," [109] use the electro-optic effect to modulate the junction asymmetry and steer optical power through the device. Static devices with a fixed junction asymmetry are suitable for mode multiplexing in integrated OF mixers.

We have developed asymmetric Y-junctions that are compatible with standard OF mixers and can sort TM_{00} and TM_{10} modes with over 30 dB of contrast. The junctions maintain this high contrast across the 1550-nm-band and do not add measurably to propagation losses. Annealed proton-exchanged (APE) waveguides are well-suited to adiabatic designs because most processing steps (SiO_2 etching, proton exchange, and annealing) tend to smooth the final refractive index profile. Current junction designs are based upon two unequal waveguides whose edge-to-edge separation decreases linearly from 20 μm to zero. In a typical design for FH_{10}/FH_{00} mode sorting, the waveguide widths are 5 μm and 3 μm. The smaller waveguide is single-moded, but close to cut-off. The larger waveguide barely supports two modes. The junctions occur over 3-4 mm in current designs, making them short enough for integration with standard OF mixers (which can be over 60-mm-long). Simulations suggest that this length can be reduced by 20% or more with better designs.

Asymmetric Y-junctions are properly analyzed using local normal modes [42]. We can find the local normal modes at any point in a branching waveguide structure by taking two-dimensional cross sections of the refractive index distribution and using our standard mode solver. Figure 5.8 shows a top view of 3-μm and 5-μm waveguides joining to form an 8-μm waveguide, along with mode solver results for the indicated cross-sections at 1550 nm. The calculated mode shapes (viewed in the x, y-plane) reveal a striking mode evolution. The FH_{00} mode of the 3-μm waveguide (upper set) develops a second lobe, becoming the FH_{10} mode of the 8-μm waveguide. The FH_{00} mode, smaller because it is farther from cut-off, remains an FH_{00} mode throughout the structure (lower set). For high contrast mode sorting, coupling between these modes must be prevented.

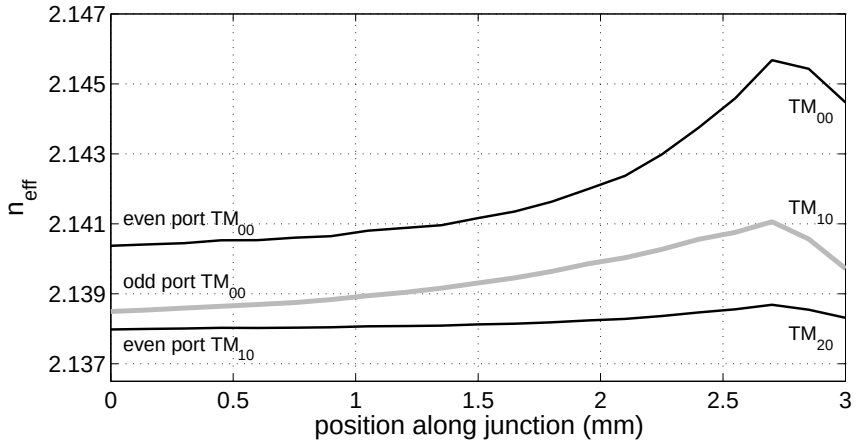

Figure 5.9: Local normal mode calculations of n_{eff} for three modes versus position in an asymmetric Y-junction.

The mode solver results also track the effective indices of the modes through an asymmetric Y-junction. Figure 5.9 shows the evolution of n_{eff} that accompanies the mode shape changes illustrated in Figure 5.8. At the left, the waveguides are essentially uncoupled, and n_{eff} of the fundamental mode of the narrower waveguide (gray colored trace) falls between the effective indices for the lowest two modes of the wider waveguide (black colored traces). As the waveguide separation decreases, the effective indices of the coupled waveguide structure shift without crossing. At the right of the figure, they represent the first three modes of the 8-μm waveguide. Thus the original n_{eff} ordering determines the final mode shapes, so that FH_{00} at the narrow (odd) port becomes FH_{10}. At the wider (even) port, FH_{00} is unchanged, and FH_{10} becomes FH_{20}, although the latter is close to cut-off. There is a deep analogy here to energy levels in quantum mechanical systems. Mathematically, descriptions of mode evolution in asymmetric Y-junctions and in coupled asymmetric potential wells have the same form because of the similarity between the electromagnetic wave equation and Schrödinger's equation [110, 111].

Tracking the effective indices leads to simple design criteria for high contrast asymmetric Y-junctions. Knowing that phase velocity mismatch between two coupled modes reduces their exchange of power, maximizing the spacing between modes Δn_{eff}

should minimize their coupling. Indeed, the 3-μm/5-μm design maximizes Δn_{eff} between the branches while keeping them both nearly single-moded. If the 5-μm branch were much larger, its second mode would displace FH_{00} of the 3-μm branch, changing the mode ordering. From our experience with symmetric Y-junctions, we chose designs without width discontinuities, so that the output branch width is the sum of the input branch widths. Experimentally, we find good performance for a range of waveguide widths around the 3-μm/5-μm design point.

To calculate the expected amount of mode coupling for a particular asymmetric Y-junction design, we need more than the effective index picture. Local normal mode theory [53] shows that the coupling coefficient κ for two modes a and b depends on the mode overlap as well as the rate of change of the waveguide structure:

$$\kappa_{a,b} \propto \frac{1}{(k_a - k_b)} \int_{-\infty}^{\infty} \int_{-\infty}^{\infty} \frac{\partial n^2}{\partial z} \tilde{E}_a^* \, \tilde{E}_b \, dx \, dy. \tag{5.2}$$

The phase velocity mismatch Δk appears both here and in the corresponding coupled mode equations, showing the importance of creating a large Δn_{eff}. $\kappa_{a,b}(z)$ can be approximated using a series of two-dimensional slices of the junction structure; the APE diffusion model supplies $n(x, y)$ at each slice, while the mode solver provides $E_i(x, y)$ and k_i. Numerical integration of $\kappa_{a,b}(z)$ yields an estimate of the mode coupling.

While this local normal mode calculation is somewhat slow and cumbersome in its current form, it still provides valuable comparisons with experimental results. Mode content measurements (Section 5.5) for a variety of designs show that the asymmetric junction contrast improves rapidly with device length. For example, scaling the 3-μm/5-μm design by a factor of 5 improves the mode sorting contrast from 10 dB to 30 dB; in the best designs, the edge-to-edge separation between branches decreases no faster than 5μm/mm. Local normal mode calculations like the one in Figure 5.10 show that modest increases in device length dramatically reduce the amount of mode coupling for typical designs. Refinement of these calculations will lead to their use as a design tool for optimizing mode contrast versus junction length. BPM simulations have been helpful in demonstrating the basic mode sorting behavior, but have not

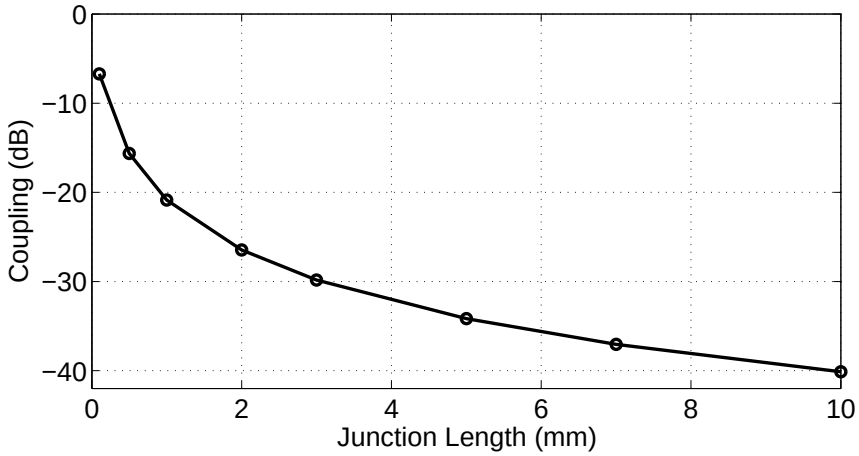

Figure 5.10: Local normal mode calculation of mode coupling in a typical asymmetric Y-junction as the design length is scaled. Modest increases in device length greatly improve the mode sorting contrast.

yielded precise information in cases where the total coupling is small.

What makes APE waveguides especially well-suited to asymmetric Y-junction design is the ability to create large changes in n_{eff} by changing the waveguide width. Wide and narrow waveguides can have peak Δn values that differ by more than a factor of two because of the nonlinear proton diffusion (Section 3.3). The resulting Δn_{eff} can be as large as ≈ 0.008, or approximately 3.5%. In contrast, Δn is independent of waveguide width in material systems such as silica-on-silicon waveguides or ridge waveguides in semiconductors, making it harder to adjust n_{eff} and the total number of modes in a structure.

5.5 Mode Content Measurements

One challenge faced in characterizing asymmetric Y-junction designs is measuring mode content (TM_{00} versus TM_{10}). To measure greater than 30 dB of contrast in high quality junctions, we need mode content measurements with a resolution better than 0.1%. Imaging the modal interference at the waveguide output may not provide such precise information without some knowledge of the mode shapes or their relative

phase. We have developed a simple but sensitive technique for measuring waveguide mode content at the first-harmonic (FH) wavelength using QPM mixing between FH_{00} and FH_{10}. With these two modes, three different SHG and SFG processes are possible:

$$SH_{00} = \eta_{00} (FH_{00})^2 \tag{5.3}$$

$$SH_{10} = 4\eta_{10} FH_{00} FH_{10} \tag{5.4}$$

$$SH_{20} = \eta_{20} (FH_{10})^2. \tag{5.5}$$

These equations relate the SH and FH mode power and the conversion efficiency (labelled by SH mode) for each process. The factor of four in (5.4) was derived in (2.34). The efficiency ratio ($\eta_{20} : \eta_{00} : 4\eta_{10}$), obtained by both calculation and experiment, is $(0.22 : 0.43 : 1.00)$, where unity corresponds to $120\%/\text{W}\cdot\text{cm}^2$. Dividing the first or third equations by the second, we see that measuring the relative second-harmonic (SH) power produced by each process in the same device yields a direct, *linear* measurement of the ratio FH_{00}/FH_{10}. The measurement is linear in the sense that the mode power ratio is simply proportional to the ratio of two SHG/SFG tuning-curve peaks. Choosing three different SH output modes has several advantages: it makes the processes easily distinguishable, it allows the use of standard rather than angled QPM gratings, and it results in similar QPM periods for all three interactions.

Figure 5.11 shows the measured (open markers) and calculated (thicker line) phasematching wavelengths for all three processes, for five different waveguide widths and the same QPM period (15.15 μm). Our waveguide fabrication model [61] successfully predicts the absolute phasematching wavelength as well as the shapes of these curves. The 17-μm width is convenient for mode content measurements because it yields three distinct SHG/SFG tuning curves within a span of only 5 nm, short enough to ensure constant coupling and power levels from a tunable diode laser input source.

In a series of experiments, we characterized various asymmetric Y-junction designs by launching 1 mW of FH power through the odd and even input ports into a 40-mm-long mixing section, and measuring the SH output. The gray and black tuning curves in Figure 5.12, which correspond to launching through the odd and even ports,

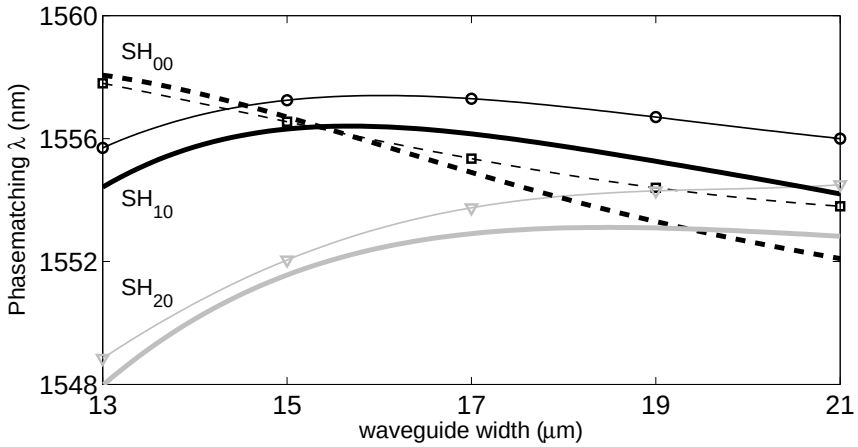

Figure 5.11: Measured (open markers) and calculated (thicker lines) phasematching wavelengths versus waveguide width for all three SHG/SFG processes; the QPM period is fixed at 15.15 μm.

contain SH_{20}, SH_{00}, and SH_{10} peaks at roughly 1542, 1543, and 1545 nm due to a 15.0-μm QPM period. Relatively large SH_{20} or SH_{00} peaks indicate high purity FH_{10} and FH_{00} mode launching, while a relatively large SH_{10} peak corresponds to a more equal mixture of FH modes, and therefore a lower contrast junction.

Figure 5.12a reveals FH_{00}/FH_{10} ratios of 11 dB and (negative) 10 dB for even and odd port launching in a typical, first-generation device. This contrast was vastly improved (Figure 5.12b) by stretching out the design by a factor of five to make the junction more adiabatic. As seen in the enlarged scale in Figure 5.12c, the SH_{10} peak at 1545 nm is nearly lost in the wings of the other SH peaks, corresponding to a contrast of at least 27 dB and 32 dB for the even and odd ports. Note that the peak spacing, and thus the dynamic range of this technique, could be readily increased by changing the waveguide design. Symmetric Y-junction measurements (Figure 5.12d) show, as expected, that both ports launch an equal mode mixture ($FH_{00}/FH_{10} = 1$); they also provide an independent check on the SH efficiency calibration (superimposed square markers).

It is unclear what limits the mode contrast in the best devices to 30-35 dB. Above the 25-dB level, large variations are seen in nominally identical devices, possibly

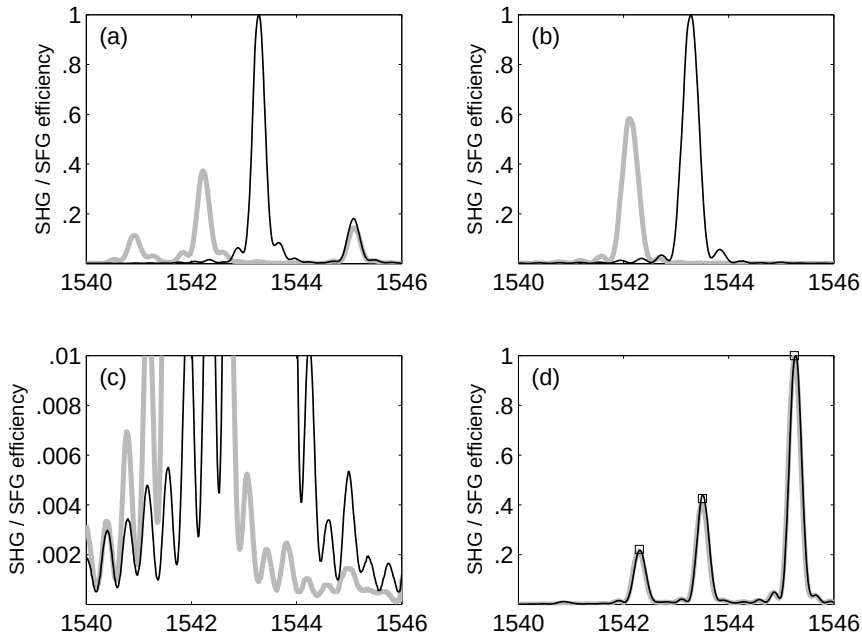

Figure 5.12: SHG/SFG tuning curves for odd (gray) and even (black) port launching. The 1545-nm peak indicates a FH_{00} and FH_{10} mixture (a), and a low contrast asymmetric Y-junction. Using a high-contrast junction, this peak is reduced (b) and can only seen by magnifying the y-axis (c). The relative peak heights for a symmetric Y-junction (d) confirm an equal FH_{00}/FH_{10} mixture for both ports.

from small fabrication defects that may cause mode coupling. At these low levels, however, the performance of standard adiabatic taper designs is also questionable. Small amounts of higher-order modes may be launched through input structures that were originally designed to maximize TM_{00} mode coupling, not TM_{00} mode purity. Design tests for asymmetric Y-junctions, mode filters, and adiabatic tapers must integrated together as mode purity becomes increasingly important in OF mixers.

Interestingly, the 1541-nm peak in Figure 5.12a corresponds to another mixing process from the same "family" described in Section 5.3 (at the bottom of Table 5.1):

$$SH_{40} = \eta_{40} (FH_{20})^2. \tag{5.6}$$

At the 17-μm width, $(\eta_{40} : 4\eta_{10}) = (0.18 : 1.00)$. Monitoring this peak is useful in developing other integrated optical devices. In symmetric Y-junctions, adiabatic tapers, and small-radius bends, coupling to FH_{20} can be a hidden source of losses or interference.

5.6 Odd-Even Mode DFM

To demonstrate how mode multiplexing can solve the distinguishability and spatial separation problem, we fabricated and tested the odd-even mode integrated OF mixer shown in Figure 5.1. The two asymmetric Y-junctions used in this four-port device were based on provisional designs yielding 30-dB of contrast between the odd and even waveguide modes. A 1-mW signal at 1557.0 nm launched through the odd input port into a FH_{10} mode produces a wavelength-converted FH_{00}-mode output at 1555.5 nm by cascaded SFG and DFM (Section 2.2.6). Because of the second junction, the even output port contains most of this mixer output (the idler wave), while the odd output port contains most of the residual input signal. The black and gray traces in Figure 5.13 show the optical spectrum measured at both ports.

In this proof-of-principle device, the conversion efficiency was only -18.8 dB because of shortened (23-mm) QPM gratings, and consequently the even port contrast between mixer output and residual input was reduced to 12.5 dB. With full-length

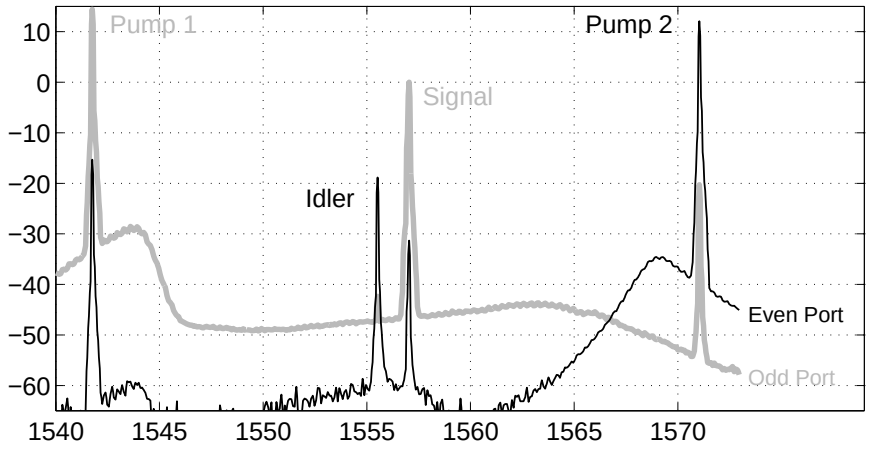

Figure 5.13: Measured output power versus wavelength for an odd-even mode wavelength converter. The odd port (gray) contains most of the residual signal (1557.0 nm) while the even port (black) contains 12.5 dB more mixer output (1555.8) than residual signal. Transmission of the residual pumps shows the full device contrast to be greater than 30 dB.

gratings, however, the conversion efficiency would be roughly 0 dB given the pump power used in this experiment ($\approx$ 100 mW at both ports), and the contrast would reach 30 dB – sufficient for optical signal processing applications. Note that the full 30-dB contrast is apparent in Figure 5.13 from the low level of cross-talk between the odd and even pump modes.

The three input waves (two pumps, one signal) are launched simultaneously into two input ports using a butt-coupled V-groove fiber array; Pump 1 and the signal are combined in fiber before launching. With careful alignment, we obtain coupling losses less than 15% (excluding Fresnel reflection losses) on each port for simultaneous two-port launching. These losses are the same as for coupling to a single waveguide. The ability to input- or output-couple multiple ports at the same time is becoming an increasingly important tool for integrated OF mixers [1].

Matching the 250-μm array spacing to the 20-μm branch separation requires 4-mm-long S-bend sections in the APE waveguides. With their minimum radius held above 24 mm, the bends add no extraneous losses or mode conversion. The conservative length of these bends and of the asymmetric Y-junctions contribute to the

short QPM gratings, along with the choice of 50-mm (rather than 62-mm) chips for fabrication and testing convenience. All of these lengths could optimized to increase efficiency in future mixers.

The cascaded SFG:DFM scheme makes this odd-even mode mixer suitable for spectral inversion or gated mixing without offset. As discussed in Sections 2.2.6 and 1.4, placing the pump wavelengths at the edges of the conversion bandwidth reserves its center for signal waves that may span the DFM degeneracy point. Pumping with both FH_{00} and FH_{10} is not only convenient (since both modes must be launched anyway), it is also more efficient than a comparable cascaded SHG:DFM scheme. The SH_{10} local oscillator is the obvious choice for an odd-even mode mixer since it generally has best best overlap with the product of FH_{00} and FH_{10}; Table 5.1 shows this for the 12-μm waveguide case. The odd/even mode mixing process is also the most efficient way of generating this local oscillator when compared to $(FH_{00})^2$ or $(FH_{10})^2$, particularly if the additional factor of 4 from SFG can be exploited. More seriously, either of these SHG processes could cause cross-talk and unwanted mixing products. Besides producing the local oscillator, the SHG process is equivalent to even-even (or odd-odd) mode DFM, which can create spurious idler outputs in the "wrong" mode if it occurs simultaneously with odd-even mode DFM. When distinguishability is not a concern, an alternative is to use even-even mode SHG to create the local oscillator and odd-odd mode DFM for wavelength conversion, e.g., using processes *b* and *h* from Table 5.1. Another possibility is to separate the cascaded processes into discrete steps, and introduce the signal only after the local oscillator has been generated.

One property of odd-even mode DFM that has yet to be explored experimentally is the conversion bandwidth. Because FH_{00} and FH_{10} have different dispersion, the conversion bandwidth is asymmetric about the degeneracy point and depends on the choice of signal and idler modes. Calculations in Figure 5.14 illustrate this feature. While a 5-cm-long, standard OF mixer has a 70-nm tuning range (dashed line), only half of this 3-dB bandwidth can be used at a time because of the distinguishability problem. A 5-cm-long odd-even mode mixer can convert a 73-nm-wide FH_{10} input (gray line) to a FH_{00} output (black line), except in this case the signal and idler bands

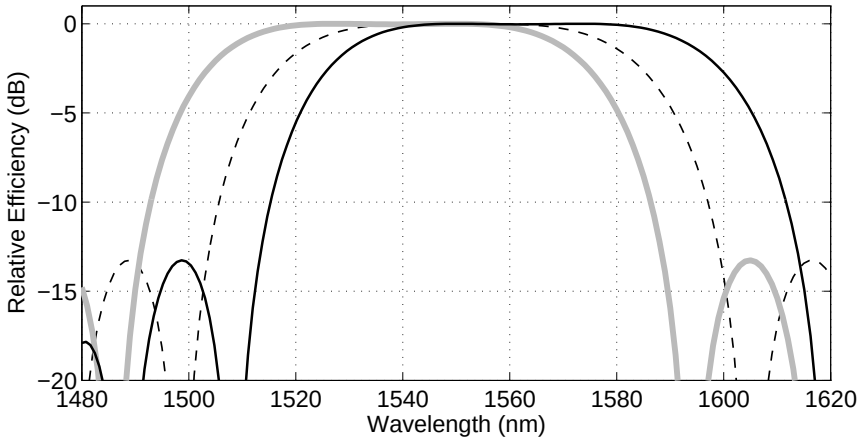

Figure 5.14: Calculations comparing the odd-even mode (gray and black lines) DFM bandwidth to that of standard devices (dashed line).

do not completely overlap. Note that FH_{10} shifts toward shorter wavelengths because it is slightly less dispersive than FH_{00}. This situation increases the maximum DFM tuning range to 103 nm, almost 50% larger than in standard devices. In the case of spectral inversion without offset, or strict bi-directional wavelength conversion, it is necessary to stay within the narrower central region of the odd-even mode DFM spectrum. Although the bandwidth for these functions – which cannot be performed with standard OF mixers – is only 51 nm, this still represents an increase over standard devices, which are restricted to a 35-nm span.

5.7 Future Work

This chapter has developed the basic tools needed for many mode multiplexing devices. Improving these tools will add many more device possibilities. Efforts have already been made to extend the use of asymmetric Y-junctions to a larger set of higher-order modes. Local normal mode calculations suggest it might be possible to convert between mode 1 and any other mode up to mode 9. Although the mode

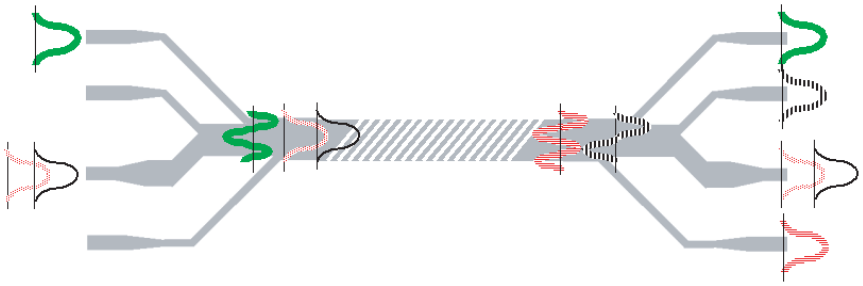

Figure 5.15: Cascaded asymmetric Y-junctions could multiplex additional higher-order modes, adding new possibilities for signal processing devices.

spacing, Δn_{eff}, decreases for higher-order modes, the overlap integral between higher-order modes also decreases; these effects may balance each other somewhat, preventing large increases in the coupling coefficient (5.2). Initial experiments yielding what appears to be a mode 1 to mode 4 converter are encouraging.

Cascading together higher-order-mode asymmetric Y-junctions could allow more complicated OF mixers in which a multiplicity of modes are launched through TM_{00} mode inputs and mixed in combinations determined by the K_g-vector(s) and the symmetry of the QPM grating (Figure 5.15). This arrangement would allow mode multiplexing to complement time-division and wavelength-division multiplexing techniques. Extending asymmetric Y-junction designs to other wavelengths (particularly the SH) would also be useful for many OF mixers, and should be straightforward using our waveguide model. Asymmetric Y-junctions may prove to be superior to directional couplers for combining or separating vastly different wavelengths like the FH and SH.

The same three mixing processes used in the mode content measurements could be used in optical logic, to perform simultaneous "AND" and "OR" functions, or in nonlinear phase discrimination. Odd-even mode DFM schemes for signal and idler wave separation/manipulation can be applied generally to optical parametric generation (OPG) or oscillation (OPO). OPG of FH_{00} and FH_{10} at 1550-nm from SH_{00}, combined with a mode sorter/converter, might prove to be an efficient source of correlated photons for quantum communications.

Chapter 6

QPM Physical Optics

While transversely patterned QPM gratings are critical in many integrated OF mixers, they also create new possibilities for non-waveguide devices. The fine grating features used in odd-even mode mixers or OF balanced mixers also lead to a multitude of bulk nonlinear optical devices based on familiar physical optics effects [112].

6.1 Transversely Patterned QPM Sources

Transverse patterning of QPM gratings has been used to increase the tuning range of devices [113], to shape the amplitude profile of an interacting beam [114], and to create two-dimensional periodic QPM structures [115, 116] for efficient noncollinear mixing. Devices with micron-scale transverse control of the position and width – as measured perpendicular to the k-vector – of individual grating segments can also be viewed as a programmable amplitude and phase mask for nonlinear mixing. Narrow stripes of precisely positioned grating can be treated as coherent optical line sources suitable for demonstrating a multitude of one-dimensional physical optics effects. In the far-field, these line sources can be treated as one-dimensional "slit" sources. This chapter presents some familiar effects from physical optics, including diffraction from single and multiple slits, that demonstrate spatial control of amplitude and phase using transversely patterned QPM.

The analogy between a transversely patterned QPM source and one-dimensional

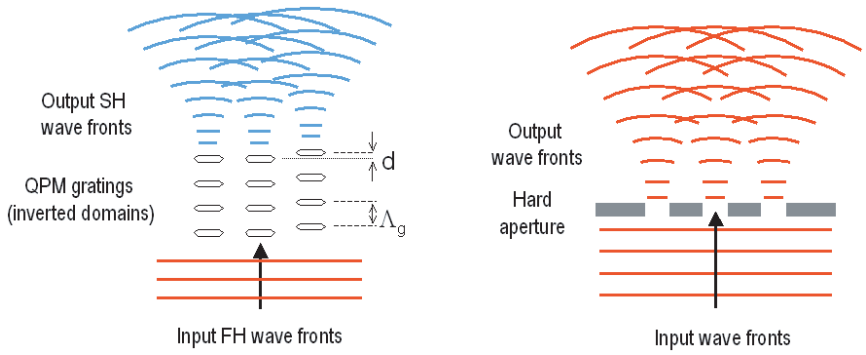

Figure 6.1: The analogy between a transversely patterned QPM source and 1-D diffraction at a hard aperture.

diffraction at a hard aperture is illustrated in Figure 6.1. With the proper arrangement of inverted domains, the QPM gratings form controllable slits for the second harmonic (SH) output. This analogy holds in the low conversion efficiency limit, and when diffraction for the FH within the device can be ignored. However, appropriate designs can compensate for – or even exploit – pump diffraction and depletion.

In devices with multiple slits, the relative phase of every slit can be independently adjusted with high precision from 0 to 2π radians by shifting the position of the entire grating stripe by a fraction of a QPM grating period, Λ_g. In Figure 6.1, a shift of distance d in the third grating adjusts its relative phase ($\phi = 2\pi d/\Lambda_g$) and modulates the position of intensity peaks in the far field. Using an array of phase-shifted grating stripes, it is possible to approximate an arbitrary phase profile across a beam in discrete steps that are limited by the minimum grating width and spacing. This technique enables the design and fabrication of more complicated structures such as QPM lenses. While continuously curved gratings might be preferable to arrays of discrete grating stripes in some beam-shaping applications, they are difficult to create. Electric-field poled domains in congruent lithium niobate tend to form hexagonal shapes with 60°-angled corners, following the crystalline symmetry.

The poling techniques described in Section 3.2 can be used to create single, double, and multiple slit devices. Figure 6.2 shows grating stripes and arrays (revealed by

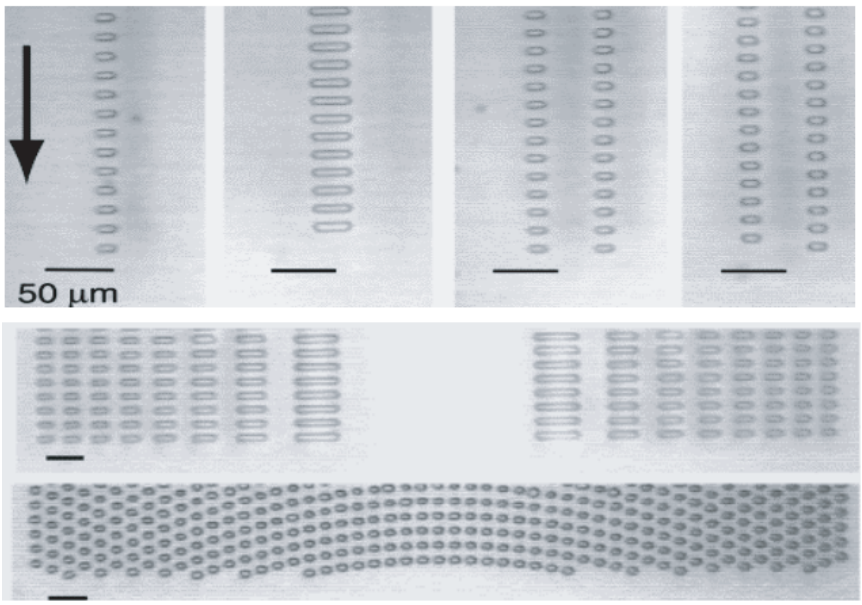

Figure 6.2: QPM optics structures revealed by etching. Top row: Single and double slit devices (10 μm and 25μm widths). Bottom: A Fresnel zone plate structure and a parabolic phase array of 8-μm-wide domains. The arrow indicates propagation direction.

etching in hydrofluoric acid) that range in width from 8 mm to 50 mm with an 18.6-μm period. In this figure, the accurate slit widths and Fresnel zone plate pattern reveal good transverse control over domain size and position, while the displaced slit pair and parabolic phase array demonstrate fine control over grating phase shifts. Fresnel phase plates, made from two complementary Fresnel amplitude plates with a π-phase shift, are also possible. As shown, the arrow indicates the beam propagation direction, and the scale bar indicates 50 μm in each image.

Arrays of inverted domains as small as 8 μm in size (with 8-μm edge-to-edge spacing) have been poled with few defects – typically less than 0.1% of the domains are missing or merged. As mentioned previously, smaller feature sizes enhance nucleation because of high fringing fields at the electrode edges, improving the pattern fidelity. The 60° corners on each inverted domain may slightly apodize the transverse patterning. Improvements to the periodic poling technique that reduce the minimum

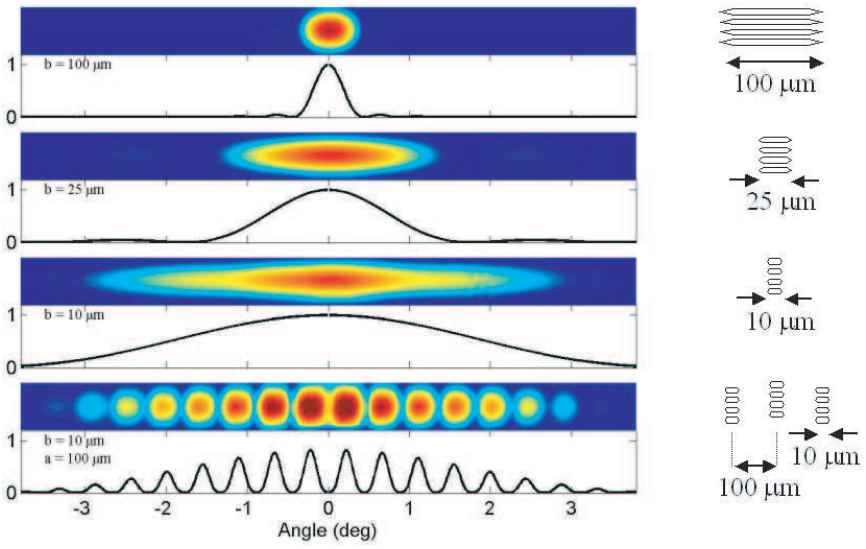

Figure 6.3: CCD images and calculations of far-field diffraction patterns from single slits and a triple-slit device (slit width b, center-to-center spacing a. The grating pattern for each device is shown schematically on the right. Note that in this image shading scheme, the highest and lowest intensity points appear black unless printed in color.

transverse grating period will help realize the full potential of QPM physical optics structures.

6.2 Single and Multiple Slit QPM Diffraction

To demonstrate classic Fraunhofer diffraction, we measured second-harmonic generation (SHG) of 1.55-μm light in various QPM physical optics devices. Devices were tested with 100 fs pulses from a synchronously-pumped optical parametric oscillator (OPO) system with 100 mW of average power (1.3 nJ pulses). To avoid any possibility of photorefractive damage, the devices were heated to 120° C before testing. With a loosely focused input beam (140-μm waist), the grating stripes served as one-dimensional hard apertures, producing SH output with familiar far-field diffraction patterns (Figure 6.3). Silicon CCD camera images comparing the measured and expected angular intensity distribution of the SH show excellent agreement for single

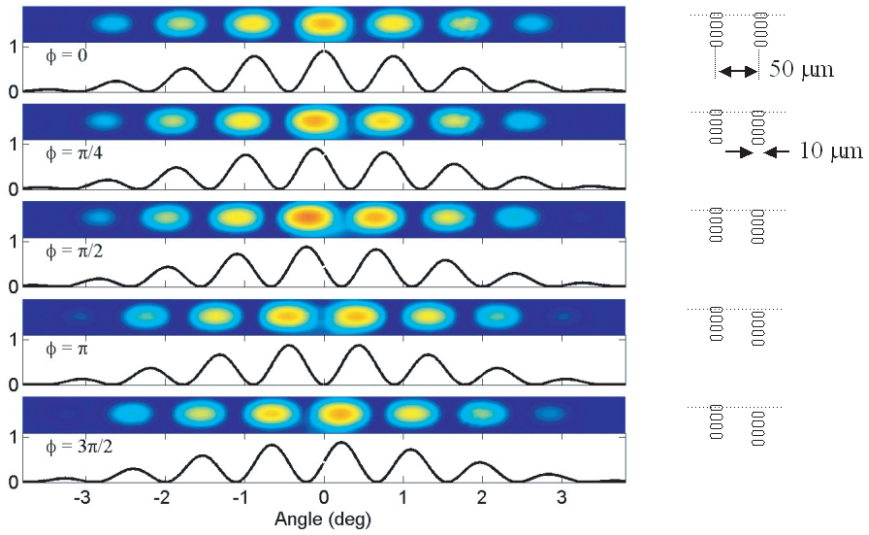

Figure 6.4: CCD images and calculated Fraunhofer diffraction from two slits with various relative phases. A relative displacement d between two gratings results in a relative phase $\phi = 2\pi d/\Lambda_g$.

slit devices (slit widths $b = 100$ μm, 25 μm, 10 μm), and a three-slit device (slit width $b = 10$ μm, center-to-center slit spacing a = 100 μm, π-phase shift on the central slit). The expected intensity distributions can be calculated analytically [117]. Note that in the shading scheme used for these CCD images, the highest and lowest intensity points appear black unless printed in color.

To investigate phase control between grating stripes, we tested a series of two-slit devices ($b = 10$ μm, $a = 50$ μm) with relative grating phases between 0 and $3\pi/2$. As shown in the calculated intensity distributions and their corresponding CCD images (Figure 6.4), adjusting the phase of one slit shifts the far-field (Fraunhofer) diffraction pattern. A π-phase shift produces a complementary distribution of intensity peaks, with a null in the center. Note that significant SH diffraction occurs within these 5-mm-long devices for the smallest grating widths. However, the effect of this finite device length on the far-field angular distribution – of primary interest here – was negligible.

As a simple multiple-slit device demonstration, we periodically poled linear phase

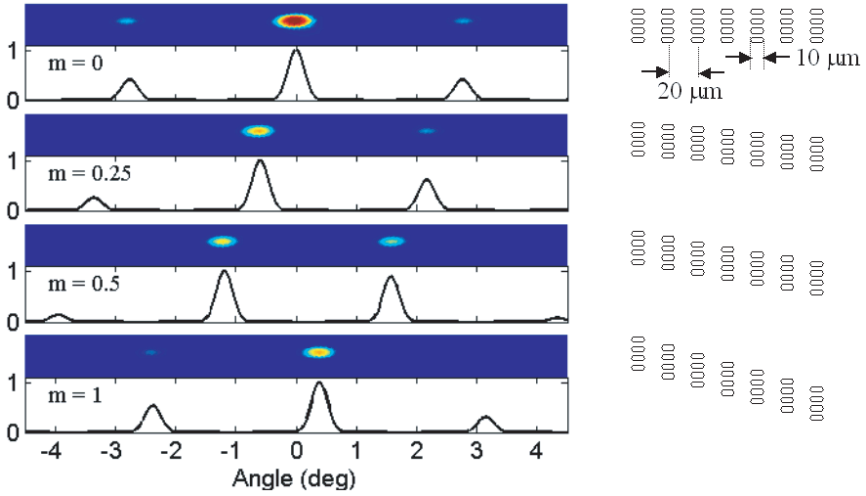

Figure 6.5: Measurements and predicted beam steering behavior for linear phase arrays of grating stripes with a variety of phase slopes m.

arrays of grating stripes for beam steering experiments. These arrays had transverse domain periods Λ_x of either 16 or 20 μm extending over 1 mm. A fixed offset d between each grating stripe in an array produced a stepwise approximation to a linearly increasing phase front across the SH output beam. In the course of mask fabrication, this constant phase slope was parameterized as a geometric slope m between domain centers; for example, with $\Lambda_x = 20$ μm, a slope $m = 0.5$ corresponded to a domain offset $d = 10$ μm. The phase slope (approximated in discrete steps set by Λ_x) for this case, $\phi/(20\mu\text{m}) = 0.054\pi/\mu\text{m}$, is representative of the rather large slopes that can be obtained by fine transverse patterning of QPM gratings. Devices with geometric phase slopes between 0 and 1 showed the expected beam steering behavior, along with multiple diffraction peaks due to the 16 μm transverse grating period (Figure 6.5). While measuring the SH output, some of the smaller peaks were obscured by the limited dynamic range of the CCD camera.

In a separate device, we poled a 17-mm-wide array with a linearly increasing phase slope (parabolic phase). Since the phase slope varied slowly enough to be treated as constant across the width of the FH beam, we were able to demonstrate a continuously tunable linear phase array by translating the device. As the phase slope was tuned,

the far field intensity peaks shifted in a cyclical fashion; the same intensity pattern appeared each time d increased by an integer multiple of Λ_g because a 2π-phase shift between grating stripes has no effect.

6.3 QPM Lenses

A transversely patterned array of QPM grating stripes with a parabolic phase profile forms a cylindrical lens for the SH output. The SH output focuses in one dimension only, since the transversely patterned gratings are uniform in depth. We fabricated 5-mm-long QPM lenses with focal lengths $f = 2$, 5, and 10 cm. For each lens the phase of the grating stripes were set by $\phi(r) = kr^2/2f$, where r is the stripe location relative to the lens center and k is the propagation constant (in air) at the SH wavelength. To keep the device compact, the displacements d needed to set these grating phases were taken modulo Λ_g, as seen in the lens in Figure 6.2. The lenses, 1-mm-wide, had $\Lambda_x = 20$ μm, yielding 50 individual grating stripes. With the FH beam expanded to a 600-μm waist, cylindrical focusing of the SH beam was clearly observed by translating a CCD camera along the propagation direction. Figure 6.6 shows the beam profile at various propagation distances referenced to the end face of a 5-cm-focal-length lens, confirming the expected waist minimum at 5 cm. Figure 6.7 provides the exact location and scale for each image. As in the linear phase gratings, multiple diffraction orders – which produce multiple foci – result from the periodicity of the transverse patterning. The 500-μm scale bar applies to all images.

Measurements of the beam waist versus propagation distance after the QPM lens, taken with a scanning knife-edge beam profiling system, showed nearly ideal focusing behavior. In Figure 6.8, data for 2, 5, and 10-cm focal length lenses (diamond, square, and circle markers) very closely matches the expected beam propagation, including the calculated minimum waist sizes and locations. The dashed and solid lines are calculations based on an ideal thin lens approximation, and a Green's function approach for the entire grating array [118], respectively. The Green's function calculation integrates the contribution to the nonlinear polarization from each inverted domain, for one output point at a time. Both QPM lens calculations rely only on

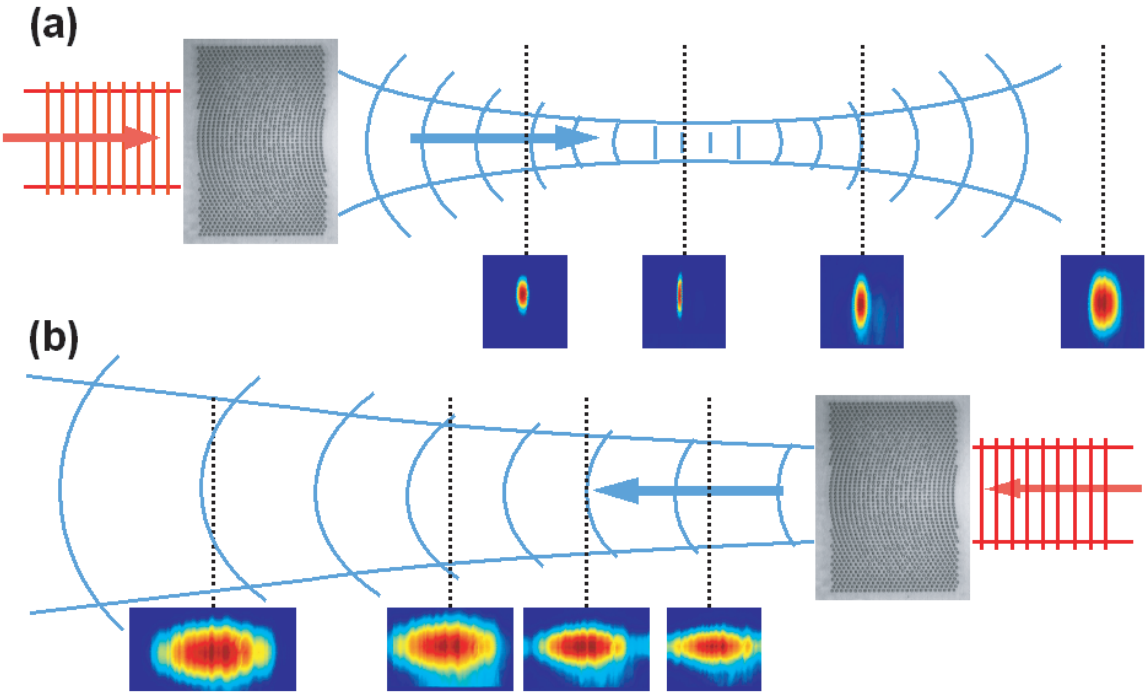

Figure 6.6: CCD images of the SH beam at various propagation distances for forward (a) and backward (b) transmission through an $f = 5$ cm QPM lens device. Reversing the propagation direction changes the sign of the focal length.

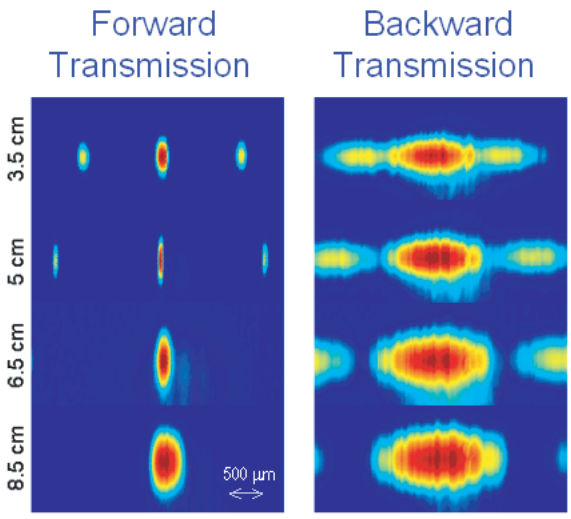

Figure 6.7: SH beam size versus propagation distance for the QPM lens measurements shown in Figure 6.6. The 500-μm scale bar applies to all images.

measurements of the beam profile in front of the sample and have no fitting parameters. Some of the ripples in the beam diameter measurement and calculation result from the slightly non-Gaussian SH beam profile formed by clipping of the expanded FH beam at the edges of the grating array. This clipping could be avoided by making larger QPM lenses, or by varying the grating length or duty cycle to apodize their amplitude profile across the FH beam. The diffracted orders complicate the near field beam measurements because they interfere with the central order; the proper choice of transverse grating pattern could steer these orders farther away, or rearrange their angular distribution more favorably.

The focusing limits of QPM lenses based on parabolic phase arrays are set by Λ_x, since the phase shift between two adjacent grating stripes must be smaller than 2π. This limit on the maximum phase slope means that while short-focal-length lenses can be fabricated with lithographic precision, the maximum lens diameter d shrinks in proportion to f. Writing out this relationship explicitly for a lens of radius $r = d/2$,

$$\left.\frac{d\phi(r)}{dr}\right|_{max} = \left.\frac{kr}{f}\right|_{r=d/2} \approx \frac{2\pi}{\Lambda_x}. \tag{6.1}$$

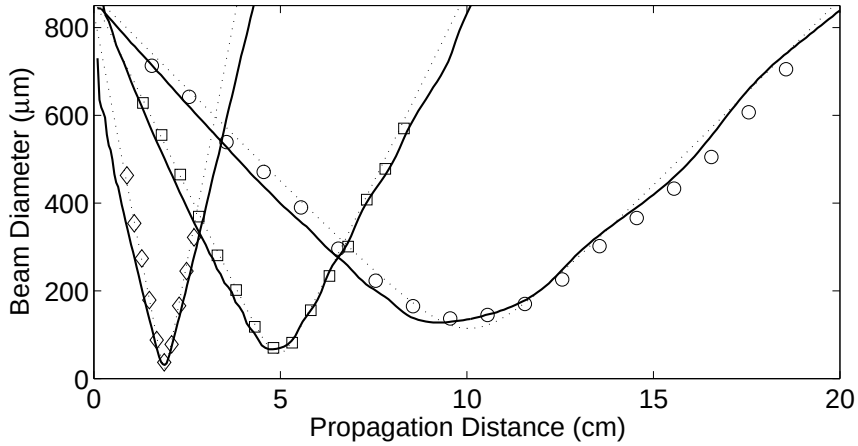

Figure 6.8: Measurements (markers) of beam waist versus propagation distance for an $f = 5$ cm QPM lens show good agreement with a thin lens approximation (dashed line), and a calculation using a Green's function approach (solid line).

Thus a QPM lens can focus a SH beam to a minimum spot size (in the x-dimension)

$$d_0 \approx \frac{f}{d}\lambda_{SH} \approx \frac{\Lambda_x}{2}. \tag{6.2}$$

This tight focusing regime has not yet been explored experimentally. In contrast to parabolic phase array design, it is challenging to produce *long* focal length QPM lenses using Fresnel amplitude and phase plates. Lithographic constraints on the minimum domain width and spacing generally limit f to less than 5 mm. Consequently, QPM Fresnel lenses must be thin, which reduces their (inherently low) efficiency and makes them difficult to characterize.

Although QPM lenses based on SHG are capable of focusing gaussian beams, they do not have the same imaging properties as conventional lenses because mixing between k-vectors in the object wavefront can cause image distortion. However, imaging should be possible with QPM lenses based on SFG or DFM, using a collimated pump that fills the lens aperture. SFG and DFM can provide the one-to-one mapping between input and output k-vectors needed for imaging.

The non-reciprocal focal length of QPM lenses is a remarkable feature. Viewed

from the opposite propagation direction, the phase curvature of a parabolic grating array changes sign so that a focal length f becomes -f. Turning the device around changes a converging lens into a diverging lens. The two halves of Figure 6.7 and Figure 6.6 clearly demonstrate this nonlinear effect, comparing the SH beam at selected distances for forward and backward transmission through a 5-cm focal length QPM lens. After backward transmission through the device, the diverging lens increases beam size. Careful examination of Figure 6.7 shows that the SH output contains additional diffracted orders for both forward and backward transmission. The center-to-center spacing of these orders can be used to reference pairs of CCD images taken at equivalent distances, since the angular separation of these orders (being set by Λ_x) is the same for both propagation directions.

Parabolic phase grating arrays and flat-phase grating arrays have the same SHG efficiency. This confirms that adding phase structure to grating arrays does not degrade their amplitude, so we can program arbitrary phase profiles. At the QPM lens output we measured 260 μW of SH output with 100 mW of FH ($\approx$ 0.21 %/nJ efficiency) – a good result given the 5-mm grating length, expanded beam, and 50% transverse grating duty cycle.

6.4 Future Work

Transverse patterning of QPM gratings provides a convenient tool for beam shaping, particularly when large phase shifts are required over small spatial scales. While a narrow grating stripe forms a nearly ideal one-dimensional slit source, phased arrays of grating stripes allow precise tailoring of the amplitude and phase profile of the SH beam. We have demonstrated single and multiple-slit gratings, linear phase arrays, and lenses. This general transverse patterning technique offers many possibilities for other devices, such as beam splitters and combiners. The overall efficiency of many QPM physical optics devices could be greatly increased in a planar waveguide configuration.

Active devices in which one beam modifies the spatial amplitude or phase profile of another – in a time-gated fashion, if desired – can be designed using SFG or DFM.

Chromatic dispersion (both spatial and temporal) can be engineered with multiple grating periods or aperiodic gratings in the transverse or longitudinal directions. QPM lenses might substitute for conventional lenses in some systems, and their nonreciprocal property could be used for separate manipulation of forward and backward waves in intracavity devices. QPM physical optics structures may both simplify and expand the use of nonlinear optical devices.

Chapter 7

Conclusion

7.1 Summary

This dissertation makes significant contributions to the development of integrated OF mixer devices, including advanced techniques for their fabrication. Using standard OF mixers as a starting point, this thesis has produced a complementary toolbox of well-characterized integrated-optic components. These components increase functionality while maintaining the high normalized efficiencies of standard "long doubler" devices (Section 3.3).

This work offers suitable designs for waveguide couplers, small-radius bends, and Y-junctions. It describes QPM gratings with micron-scale transverse patterning, and methods for aligning these gratings to waveguide components with high precision. Using these elements in an interferometer structure leads to an OF balanced mixer, which solves the distinguishability problem (Section 1.4), and enables bi-directional wavelength conversion or spectral inversion without offset. Progress is being made toward other integrated OF mixers, including a quasi-group velocity matching device.

Chapter 5 of this thesis introduces a new class of OF mixers that utilize higher-order waveguide modes for signal processing. Two additional components are developed in order to realize these mode-multiplexing devices: angled and staggered gratings for efficient odd-even mode mixing, and high-contrast (30 dB) waveguide mode sorters/converters based on asymmetric Y-junctions. These tools are used in a

variety of novel mixing devices, including an odd-to-even mode wavelength converter that provides another flexible solution to the distinguishability problem.

Annealed proton-exchanged (APE) PPLN waveguide fabrication has been adapted to the increasing complexity of OF mixers. Chapter 3 of this thesis documents advances at each fabrication step – from the lithography and periodic poling to the proton exchange and annealing – that lead to the higher precision and reproducibility required by integrated OF mixers. These refinements include a scalable, batch process that reduces processing time per wafer while improving uniformity. Better control over the electric-field poling process has also stimulated the invention of QPM physical optics devices. These bulk devices use fine transverse patterning of gratings to control the spatial amplitude and phase of the nonlinear output. Several beam steering and shaping devices are demonstrated using this technology, including QPM lenses, which have a focal length that depends on the direction of propagation.

7.2 Evolution of Integrated OF Mixers

Many new directions for integrated OF mixer development have been outlined in individual chapters of this dissertation. A larger challenge lies in extending this development to other material systems. While APE PPLN waveguide technology has many advantages, new OF mixer systems are always under development. The reverse proton exchange (RPE) process creates a more symmetric refractive index profile (in depth) that improves mixing efficiency and fiber coupling [4]. Other ferroelectrics such as MgO-doped $LiNbO_3$ and stoichiometric lithium tantalate (SLT) have greater photorefractive resistance [119, 120], allowing operation at higher powers, especially at visible wavelengths. Orientation-patterned semiconductors such as GaAs and GaN have higher nonlinear coefficients and no photorefractive effects, making them very attractive QPM materials [121, 122].

Integrated OF mixer development will be different in each of these systems. Like APE waveguides, RPE waveguides have smooth profiles conducive to making adiabatic tapers, junctions, and couplers. Better mode overlap and decreased index spacing (Δn_{eff}) in this system might make it easier to mix higher-order modes, but

harder to filter them with asymmetric Y-junctions. Early studies of APE waveguides in MgO:LN reveal a $H_xLi_{1-x}NbO_3$ phase structure that leads to step-like index profiles [71]. These profiles might be more suitable for devices with non-adiabatic junctions, such as multi-mode interference (MMI) devices [123]. Ridge waveguides in orientation-patterned semiconductors would have even sharper index steps and larger Δn values, which would make for tighter mode confinement and smaller radius bends. A completely different domain inversion process affects the prospects of making asymmetric QPM gratings and QPM physical optics devices in semiconductor materials. Semiconductor OF mixers can also support two polarizations, and may eventually be integrable with diode lasers.

For any material system, integrated OF mixers will always be the next evolutionary step once standard OF mixers have reached maturity. Although the desired devices may differ from those described in this dissertation, most of the considerations – efficiency, losses, component length, and mode purity – will be identical. Success will depend upon good waveguide modelling, intelligent designs, and precise fabrication.

Bibliography

[1] T. Ohara, H. Takara, I. Shake, K. Mori, S. Kawanishi, S. Mino, T. Yamada, M. Ishii, T. Kitoh, T. Kitagawa, K.R. Parameswaran, and M.M. Fejer, "160-Gb/s optical-time-division multiplexing with PPLN hybrid integrated planar lightwave circuit," *IEEE Photonics Technology Letters*, 15(2):302 – 4, February 2003.

[2] E.J. Lim, M.M. Fejer, R.L. Byer, and W.J. Kozlovsky, "Blue light generation by frequency doubling in periodically poled lithium niobate channel waveguide," *Electronics Letters*, 25(11):731 – 2, May 1989.

[3] E.J. Lim, M.M. Fejer, and R.L. Byer, "Second-harmonic generation of green light in periodically poled planar lithium niobate waveguide," *Electronics Letters*, 25(3):174 – 5, February 1989.

[4] K.R. Parameswaran, R.K. Route, J.R. Kurz, R.V. Roussev, M.M. Fejer, and M. Fujimura, "Highly efficient second-harmonic generation in buried waveguides formed by annealed and reverse proton exchange in periodically poled lithium niobate," *Optics Letters*, 27(3):179 – 81, February 2002.

[5] Y. Kitaoka, K. Mizuuchi, T. Yokoyama, K. Yamamoto, K. Narumi, and M. Kato, "Quasi-phase-matched second harmonic generation device in Mg-doped $LiNbO_3$ and its application to high-density optical disk system," *Bulletin of Materials Science*, 22(3):405 – 11, May 1999.

[6] K. Mizuuchi, A. Morikawa, T. Sugita, and K. Yamamoto, "Efficient second-harmonic generation of 340-nm light in a 1.4-μm periodically poled

bulk MgO:$LiNbO_3$," *Japanese Journal of Applied Physics, Part 2 (Letters)*, 42(2A):L90 – 1, February 2003.

[7] K.P. Petrov, A.P. Roth, T.L. Patterson, and D.J. Bamford, "Efficient channel waveguide device for difference-frequency mixing of diode lasers,", In *Technical Digest of the Conference on Lasers and Electro-Optics, 23-28 May 1999, Baltimore, MD, USA*.

[8] D. Mann, G. Schreiber, C. Haase, H. Herrmann, W. Grundktter, R. Ricken, and W. Sohler, "Quasi-phase-matched difference-frequency generation in periodically poled Ti:$LiNbO_3$ channel waveguides," *Optics Letters*, 24(13):896 – 8, July 1999.

[9] Ming-Hsien Chou, K.R. Parameswaran, M.M. Fejer, and I. Brener, "Optical signal processing and switching with second-order nonlinearities in waveguides," *IEICE Transactions on Electronics*, E83-C(6):869 – 74, June 2000.

[10] S.J.B. Yoo, "Wavelength conversion technologies for WDM network applications," *Journal of Lightwave Technology*, 14(6):955 – 66, June 1996.

[11] J.R. Kurz, K.R. Parameswaran, R.V. Roussev, M.M. Fejer, M.H. Chou, and I. Brener, "Optical frequency mixers for WDM and TDM applications," *Proceedings of the SPIE - The International Society for Optical Engineering*, 4532:127 – 38, 2001.

[12] R. Klein and A. Arie, "Observation of iodine transitions using the second and third harmonics of a 1.5-μm laser," *Applied Physics B (Lasers and Optics)*, B75(1):79 – 83, July 2002.

[13] K.R. Parameswaran, J.R. Kurz, R.V. Roussev, and M.M. Fejer, "Observation of 99% pump depletion in single-pass second-harmonic generation in a periodically poled lithium niobate waveguide," *Optics Letters*, 27(1):43 – 5, January 2002.

[14] R. Schiek, L. Friedrich, H. Fang, G.I. Stegeman, K.R. Parameswaran, M.-H. Chou, and M.M. Fejer, "Nonlinear directional coupler in periodically poled lithium niobate," *Optics Letters*, 24(22):1617 – 19, November 1999.

[15] Chen Xianfeng, Xia Yuxing, Xie Shenwu, Chen Yuping, and Chen Yingli, "Second and third harmonic generation in quasi-phase-matched annealed proton-exchanged lithium niobate waveguides," *Proceedings of the SPIE - The International Society for Optical Engineering*, 4223:55 – 60, 2000.

[16] A. Di Falco, G. Leo, and G. Assanto, "Novel spatial solitons in reverse proton exchanged lithium niobate waveguides,", In *LEOS 2002. 2002 IEEE/LEOS Annual Meeting Conference Proceedings. 15th Annual Meeting of the IEEE Lasers and Electro-Optics Society, 10-14 Nov. 2002, Glasgow, UK.*

[17] R. Schiek, Y. Baek, G.I. Stegeman, and W. Sohler, "One-dimensional quadratic walking solitons," *Optics Letters*, 24(2):83 – 5, January 1999.

[18] Z. Zheng, A.M. Weiner, K.R. Parameswaran, M.H. Chou, and M.M. Fejer, "Spectral phase correlator for coded waveform recognition using second harmonic generation,", In *Trends in Optics and Photonics. Twelfth International Conference on Ultrafast Phenomena Vol.43. Technical Digest. Postconference Edition, 9-13 July 2000, Charleston, SC, USA.*

[19] R. Schiek, W. Elflein, T. Pertsch, A. Tunnermann, K.R. Parameswaran, and M.M. Fejer, "Femtosecond all-optical switching in a lithium niobate directional coupler with cascaded nonlinearity,", In *Nonlinear Optics: Materials, Fundamentals, and Applications. Technical Digest. TOPS Vol.46, 6-10 Aug. 2000, Kaua'i-Lihue, HI, USA.*

[20] Zheng Zheng, A.M. Weiner, K.R. Parameswaran, Ming-Hsien Chou, and M.M. Fejer, "Femtosecond second-harmonic generation in periodically poled lithium niobate waveguides with simultaneous strong pump depletion and group-velocity walk-off," *Journal of the Optical Society of America B (Optical Physics)*, 19(4):839 – 48, April 2002.

[21] S. Tanzilli, W. Tittel, H. De Riedmatten, H. Zbinden, P. Baldi, M. De Micheli, D.B. Ostrowsky, and N. Gisin, "PPLN waveguide for quantum communication," *European Physical Journal D*, 18(2):155 – 60, February 2002.

[22] A. Yoshizawa, R. Kaji, and H. Tsuchida, "Generation of polarisation-entangled photon pairs at 1550 nm using two PPLN waveguides," *Electronics Letters*, 39(7):621 – 2, April 2003.

[23] J.A. Armstrong, N. Bloembergen, J. Ducuing, and P.S. Pershan, "Interactions between light waves in a nonlinear dielectric," *Physical Review*, 127:1918 – 39, 1962.

[24] P.A. Franken and J.F. Ward, "Optical harmonics and nonlinear phenomena," *Rev. Mod. Phys.*, 35:23 – 39, 1963.

[25] M.M. Fejer, G.A. Magel, D.H. Jundt, and R.L. Byer, "Quasi-phase-matched second harmonic generation: tuning and tolerances," *IEEE Journal of Quantum Electronics*, 28(11):2631 – 2654, November 1992.

[26] C.Q. Xu, H. Okayama, K. Shinozaki, K. Watanabe, and M. Kawahara, "Wavelength conversions $\approx$ 1.5 μm by difference frequency generation in periodically domain-inverted $LiNbO_3$ channel waveguides," *Applied Physics Letters*, 63(9):1170 – 2, August 1993.

[27] D. Hofmann, G. Schreiber, C. Haase, H. Herrmann, W. Grundkotter, R. Ricken, and W. Sohler, "Quasi-phase-matched difference-frequency generation in periodically poled Ti:$LiNbO_3$ channel waveguides," *Optics Letters*, 24(13):896 – 8, July 1999.

[28] M.H. Chou, I. Brener, M.M. Fejer, E.E. Chaban, and S.B. Christman, "1.5-μm-band wavelength conversion based on cascaded second-order nonlinearity in $LiNbO_3$ waveguides," *IEEE Photonics Technology Letters*, 11(6):653 – 5, June 1999.

[29] C.Q. Xu, H. Okayama, and M. Kawahara, "Wavelength conversions between the two silica fibre loss windows at 1.31 and 1.55 μm using difference frequency generation," *Electronics Letters*, 30(25):2168 – 9, December 1994.

[30] M.H. Chou, K.R. Parameswaran, M.A. Arbore, J. Hauden, and M.M. Fejer, "Bidirectional wavelength conversion between 1.3- and 1.5- μm telecommunication bands using difference frequency mixing in $LiNbO_3$ waveguides with integrated coupling structures," in *Technical Digest Summaries of papers presented at the Conference on Lasers and Electro-Optics*, paper CThZ2, May 1998.

[31] M.H. Chou, K.R. Parameswaran, M.M. Fejer, and I. Brener, "Multiple-channel wavelength conversion by use of engineered quasi-phase-matching structures in $LiNbO_3$ waveguides," *Optics Letters*, 24(16):1157 – 9, August 1999.

[32] I. Brener, B. Mikkelsen, G. Raybon, R. Harel, K. Parameswaran, J.R. Kurz, and M.M. Fejer, "160 Gbit/s wavelength shifting and phase conjugation using periodically poled $LiNbO_3$ waveguide parametric converter," *Electronics Letters*, 36(21):1788 – 90, October 2000.

[33] J. Yamawaku, H. Takara, T. Ohara, K. Sato, A. Takada, T. Morioka, O. Tadanaga, H. Miyazawa, and M. Asobe, "Simultaneous 25 GHz-spaced DWDM wavelength conversion of 1.03 Tbit/s (103 channels at 10 Gbit/s) signals in PPLN waveguide," *Electronics Letters*, 39(15):1144 – 5, July 2003.

[34] M.H. Chou, I. Brener, G. Lenz, R. Scotti, E.E. Chaban, J. Shmulovich, D. Philen, S. Kosinski, K.R. Parameswaran, and M.M. Fejer, "Efficient wideband and tunable midspan spectral inverter using cascaded nonlinearities in $LiNbO_3$ waveguides," *IEEE Photonics Technology Letters*, 12(1):82 – 4, January 2000.

[35] I. Brener, B. Mikkelsen, K. Rottwitt, W. Burkett, G. Raybon, J.B. Stark, K. Parameswaran, M.H. Chou, M.M. Fejer, E.E. Chaban, R. Harel, D.L. Philen, and A. Kosinski, "Cancellation of all Kerr nonlinearities in long fiber spans using a $LiNbO_3$ phase conjugator and Raman amplification,", In *Optical Fiber Communication Conference. Technical Digest Postconference Edition. Trends in Optics and Photonics Vol.37, 7-10 March 2000, Baltimore, MD, USA*.

[36] S. Kawanishi, T. Yamamoto, M. Nakazawa, and M.M. Fejer, "High sensitivity waveform measurement with optical sampling using quasi-phasematched mixing in $LiNbO_3$ waveguide," *Electronics Letters*, 37(13):842 – 4, June 2001.

[37] M.C. Cardakli, D. Gurkan, S.A. Havstad, A.E. Willner, K.R. Parameswaran, M.M. Fejer, and I. Brener, "Tunable all-optical time-slot-interchange and wavelength conversion using difference-frequency-generation and optical buffers," *IEEE Photonics Technology Letters*, 14(2):200 – 2, February 2002.

[38] D. Gurkan, M.C. Hauer, A.B. Sahin, Z. Pan, S. Lee, A.E. Willner, K.R. Parameswaran, and M.M. Fejer, "Demonstration of multi-wavelength all-optical header recognition using a PPLN and optical correlators,", In *27th European Conference on Optical Communication, 30 Sept.-4 Oct. 2001, Amsterdam, Netherlands.*

[39] Z. Zheng, A.M. Weiner, K.R. Parameswaran, M.H. Chou, and M.M. Fejer, "Low-power spectral phase correlator using periodically poled $LiNbO_3$ waveguides," *IEEE Photonics Technology Letters*, 13(4):376 – 8, April 2001.

[40] G.I. Stegeman, "$\chi^{(2)}$ cascading: nonlinear phase shifts," *Quantum and Semiclassical Optics*, 9(2):139 – 53, April 1997.

[41] K. Gallo, G. Assanto, and G.I. Stegeman, "Efficient wavelength shifting over the erbium amplifier bandwidth via cascaded second order processes in lithium niobate waveguides," *Applied Physics Letters*, 71(8):1020 – 2, August 1997.

[42] T. Tamir, editor, *Guided-Wave Optoelectronics*, Springer Series in Electronics and Photonics 26. Springer-Verlag, 2nd edition, 1990.

[43] R. Schiek, Y. Baek, G. Krijnen, G. I. Stegeman, I. Baumann, and W. Sohler, "All-optical switching in lithium niobate directional couplers with cascaded nonlinearity," *Optics Letters*, 21(13):940 – 2, July 1996.

[44] G.S. Kanter, P. Kumar, R.V. Roussev, J. Kurz, K.R. Parameswaran, and M.M. Fejer, "Squeezing in a $LiNbO_3$ integrated optical waveguide circuit," *Optics Express*, 10(3), February 2002.

[45] M.H. Chou, T. Hauden, M.A. Arbore, and M.M. Fejer, "1.5-μm-band wavelength conversion based on difference-frequency generation in $LiNbO_3$ waveguides with integrated coupling structures," *Optics Letters*, 23(13):1004 – 6, July 1998.

[46] C. Becker, T. Oesselke, J. Pandavenes, R. Ricken, K. Rochhausen, G. Schreiber, W. Sohler, H. Suche, R. Wessel, S. Balsamo, I. Montrosset, and D. Sciancalepore, "Advanced Ti:Er:$LiNbO_3$ waveguide lasers," *IEEE Journal of Selected Topics in Quantum Electronics*, 6(1):101 – 13, January 2000.

[47] G. Schreiber, H. Suche, Y.L. Lee, W. Grundkotter, V. Quiring, R. Ricken, and W. Sohler, "Efficient cascaded difference frequency conversion in periodically poled Ti:$LiNbO_3$ waveguides using pulsed and cw pumping," *Applied Physics B (Lasers and Optics)*, B73(5-6):501 – 4, October 2001.

[48] T. Suhara and H. Ishizuki, "Integrated QPM sum-frequency generation interferometer device for ultrafast optical switching," *IEEE Photonics Technology Letters*, 13(11):1203 – 5, November 2001.

[49] V. G. Dmitriev, G. G. Gurzadyan, and D. N. Nikogosyan, *Handbook of Nonlinear Optical Crystals*, volume 64 of *Springer Series in Optical Sciences*, Springer, Berlin, 2nd edition, 1997.

[50] A. Yariv, *Quantum Electronics*, John Wiley, New York, 3rd edition, 1989.

[51] R. Boyd, *Nonlinear Optics*, Academic Press, San Diego, 1992.

[52] A. Agrawal, *Nonlinear Fiber Optics*, Academic Press, San Diego, 1995.

[53] D. Marcuse, *Theory of Dielectric Optical Waveguides*, Academic Press, San Diego, 1974.

[54] E.L. Wooten, K.M. Kissa, A. Yi-Yan, E.J. Murphy, D.A. Lafaw, P.F. Hallemeier, D. Maack, D.V. Attanasio, D.J. Fritz, G.J. McBrien, and D.E. Bossi,

"A review of lithium niobate modulators for fiber-optic communications systems," *IEEE Journal of Selected Topics in Quantum Electronics*, 6(1):69 – 82, January 2000.

[55] C.K. Campbell, *Surface Acoustic Wave Devices for Mobile and Wireless Communications*, Academic Press, San Diego, 1998.

[56] S. Matsumoto, E.J. Lim, H.M. Hertz, and M.M. Fejer, "Quasiphase-matched second harmonic generation of blue light in electrically periodically-poled lithium tantalate waveguides," *Electronics Letters*, 27(22):2040 – 2, October 1991.

[57] M. Yamada, N. Nada, M. Saitoh, and K. Watanabe, "First-order quasi-phased matched $LiNbO_3$ waveguide periodically poled by applying an external field for efficient blue second-harmonic generation," *Applied Physics Letters*, 62(5):435 – 6, February 1993.

[58] J.L. Jackel, C.E. Rice, and J.J. Veselka, "Proton exchange for high-index waveguides in $LiNbO_3$," *Applied Physics Letters*, 41(7):607 – 8, October 1982.

[59] D.F. Clark, A.C.G. Nutt, K.K. Wong, P.J.R. Laybourn, and R.M. De La Rue, "Characterization of proton-exchange slab optical waveguides in z-cut $LiNbO_3$," *Journal of Applied Physics*, 54(11):6218 – 20, November 1983.

[60] M.L. Bortz and M.M. Fejer, "Annealed proton-exchanged $LiNbO_3$ waveguides," *Optics Letters*, 16(23):1844 – 6, December 1991.

[61] R. V. Roussev, X.P. Xie, K. R. Parameswaran, M. M. Fejer, and J. Tian, "Accurate Semi-Empirical Model for Annealed Proton Exchanged waveguides in z-cut Lithium Niobate,", In *Sixteenth Annual Lasers and Electro-Optics Society Meeting*, page TuS4, October 2003.

[62] L.E. Myers, R.C. Eckardt, M.M. Fejer, R.L. Byer, W.R. Bosenberg, and J.W. Pierce, "Quasi-phase-matched optical parametric oscillators in bulk periodically

poled $LiNbO_3$," *Journal of the Optical Society of America B (Optical Physics)*, 12(11):2102 – 16, November 1995.

[63] G.D. Miller, R.G. Batchko, M.M. Fejer, and R.L. Byer, "Visible quasi-phase-matched harmonic generation by electric-field-poled lithium niobate," *Proceedings of the SPIE*, 2700:34 – 45, 1996.

[64] V. Shur, E. Nikolaeva, E. Shishkin, D. Fursov, A. Chernykh, A. Shur, A. Lobov, K. Terabe, S. Kurimura, K. Kitamura, D. Hum, J. Kurz, and M. Fejer, "Domain Engineering Achievements in $LiNbO_3$ and $LiTaO_3$,", In *Tenth European Meeting on Ferroelectricity*, Cambridge, UK, August 2003.

[65] G.D. Miller, "Periodically-poled lithium niobate: modeling, fabrication, and nonlinear-optical performance," *Ph.D. Dissertation*, Department of Electrical Engineering, Stanford University, Stanford, CA, June 1998.

[66] Ming Hsien Chou, Optical Frequency Mixers Using Three-Wave Mixing for Optical Fiber Communications, *Ph.D. Dissertation*, Department of Applied Physics, Stanford University, Stanford, CA, June 1999.

[67] T. Akutsu, H. Seki, M. Maruyama, H. Nakajima, S. Kurimura, K. Kitamura, H. Ishizuki, and T. Taira, "Selective nucleation control in periodical poling for quasi-phase-matched wavelength converters,", In *Technical Digest of the Conference on Lasers and Electro-Optics. Conference Edition, 19-24 May 2002, Long Beach, CA,USA.*

[68] M. L. Bortz, Quasi-Phasematched Optical Frequency Conversion in Lithium Niobate Waveguides, *Ph.D. Dissertation*, Department of Applied Physics, Stanford University, Stanford, CA, December 1994.

[69] E.J. Lim, S. Matsumoto, and M.M. Fejer, "Noncritical phase matching for guided-wave frequency conversion," *Applied Physics Letters*, 57(22):2294 – 6, November 1990.

[70] M.L. Bortz, S.J. Field, M.M. Fejer, D.W. Nam, R.G. Waarts, and D.F. Welch, "Noncritical quasi-phase-matched second harmonic generation in an annealed proton-exchanged $LiNbO_3$ waveguide," *IEEE Journal of Quantum Electronics*, 30(12):2953 – 60, December 1994.

[71] R.V. Roussev, Personal communication 2002.

[72] P.K. Tien and R. Ulrich, "Theory of prism-film coupler and thin-film light guides," *Journal of the Optical Society of America*, 60(10):1325 – 37, October 1970.

[73] A. Loni, G. Hay, R.M. De La Rue, and J.M. Winfield, "Proton-exchanged $LiNbO_3$ waveguides: the effects of post-exchange annealing and buffered melts as determined by infrared spectroscopy optical waveguide measurements and hydrogen isotopic exchange reactions," *Journal of Lightwave Technology*, 7(6):911 – 19, June 1989.

[74] J.M. Cabrera, J. Olivares, M. Carrascosa, J. Rams, R. Muller, and E. Dieguez, "Hydrogen in lithium niobate," *Advances in Physics*, 45(5):349 – 92, September 1996.

[75] A. M. Prokhorov and I. U. S. Kuzminov, *Physics and Chemistry of Crystalline Lithium Niobate*, The Adam Hilger series on optics and optoelectronics. A. Hilger, New York, 1990.

[76] Carver A. Mead and Lynn A. Conway, *Introduction to VLSI Systems*, Addison-Wesley, Reading, Massachusetts, 1980.

[77] N. Nishihara, M. Haruna, and T. Suhara, *Optical Integrated Circuits*, McGraw-Hill, New York, 1989.

[78] Keh-Yi Lee, Gao-Deh Chang, Hseng-Tsong Wang, and Yih-Jyh Lin, "Beam propagation analysis of ridge-type Ti:$LiNbO_3$ Y-junction waveguides," *Journal of Optical Communications*, 21(4):125 – 30, August 2000.

[79] Shyh-Lin Tsao and Chun-Yi Lu, "BPM simulation and comparison of 1 * 2 directional waveguide coupling and Y-junction coupling silicon-on-insulator optical couplers," *Fiber and Integrated Optics*, 21(6):417 – 33, 2002.

[80] Jae-Wook Kang, Eunkyoung Kim, Mi-Jeong Kim, Dong Yu Kim, and Jang-Joo Kim, "All-optical polymer waveguide devices," *Proceedings of the SPIE - The International Society for Optical Engineering*, 4905:108 – 17, 2002.

[81] J.J.G.M. van der Tol, J.W. Pedersen, E.G. Metaal, Y.S. Oei, F.H. Green, and P. Demeester, "Sharp vertices in asymmetric Y-junctions by double masking," *IEEE Photonics Technology Letters*, 6(2):249 – 51, February 1994.

[82] X. P. Xie, Personal communication 2002.

[83] A.W. Snyder and J.D. Love, *Optical waveguide theory*, London, UK : Chapman & Hall, 1983.

[84] D. Marcuse, editor, *Integrated Optics*, IEEE Press, New York, 1973.

[85] M. Heiblum and J.H. Harris, "Analysis of curved optical waveguides by conformal transformation," *IEEE Journal of Quantum Electronics*, QE-11(2):75 – 83, February 1975.

[86] K.T. Koai and P.-L. Liu, "Modeling of Ti:$LiNbO_3$ waveguide devices II. S-shaped channel waveguide bends," *Journal of Lightwave Technology*, 7(7):1016 – 22, July 1989.

[87] J.R. Kurz, K.R. Parameswaran, R.V. Roussev, and M.M. Fejer, "Optical-frequency balanced mixer," *Optics Letters*, 26(16):1283 – 5, August 2001.

[88] A. Chowdhury, S.C. Hagness, and L. McCaughan, "Simultaneous optical wavelength interchange with a two-dimensional second-order nonlinear photonic crystal," *Optics Letters*, 25(11):832 – 4, June 2000.

[89] O. Tadanaga, M. Asobe, H. Miyazawa, Y. Nishida, and H. Suzuki, "1 THz multi-channel optical frequency shifter using quasi-phase-matched $LiNbO_3$ wavelength converters," *Electronics Letters*, 38(23):1456 – 7, November 2002.

[90] K. Mori, T. Morioka, and M. Saruwatari, "Optical parametric loop mirror," *Optics Letters*, 20(12):1424 – 6, June 1995.

[91] David M. Pozar, *Microwave Engineering*, John Wiley, New York, 2nd edition, 1998.

[92] G. Imeshev, M.A. Arbore, M.M. Fejer, A. Galvanauskas, M. Fermann, and D. Harter, "Ultrashort-pulse second-harmonic generation with longitudinally nonuniform quasi-phase-matching gratings: pulse compression and shaping," *Journal of the Optical Society of America B (Optical Physics)*, 17(2):304 – 18, February 2000.

[93] G. Imeshev, M.M. Fejer, A. Galvanauskas, and D. Harter, "Pulse shaping by difference-frequency mixing with quasi-phase-matching gratings," *Journal of the Optical Society of America B (Optical Physics)*, 18(4):534 – 9, April 2001.

[94] Yan-Qing Lu, Jian-Jun Zheng, Ya-Lin Lu, Nai-Ben Ming, and Zu-Yan Xu, "Frequency tuning of optical parametric generator in periodically poled optical superlattice $LiNbO_3$ by electro-optic effect," *Applied Physics Letters*, 74(1):123 – 5, January 1999.

[95] N. O'Brien, M. Missey, P. Powers, V. Dominic, and K.L. Schepler, "Electro-optic spectral tuning in a continuous-wave asymmetric-duty-cycle periodically poled $LiNbO_3$ optical parametric oscillator," *Optics Letters*, 24(23):1750 – 2, December 1999.

[96] M. Asobe, O. Tadanaga, H. Miyazawa, Y. Nishida, and H. Suzuki, "Multiple quasi-phase-matched LiNbOsub 3 wavelength converter with a continuously phase-modulated domain structure," *Optics Letters*, 28(7):558 – 60, April 2003.

[97] J. R. Kurz, J. Huang, X.P. Xie, T. Saida, and M.M. Fejer, "Mode Multiplexing in Optical Frequency Mixers," *Optics Letters*, accepted for publication, 2003.

[98] G.I. Stegeman and C.T. Seaton, "Nonlinear integrated optics," *Journal of Applied Physics*, 58(12):R57 – 78, December 1985.

[99] H. Ito and H. Inaba, "Efficient phase-matched second-harmonic generation method in four-layered optical-waveguide structure," *Optics Letters*, 2(6):139 – 41, June 1978.

[100] J.R. Kurz, X.P. Xie, and M.M. Fejer, Odd waveguide mode quasi-phase matching with angled and staggered gratings. *Optics Letters*, 27(16):1445 – 7, August 2002.

[101] D. Yang, J.B. Khurgin, and Y.J. Ding, "Cascaded waveguide phase-matching arrangement," *Optics Letters*, 25(7):496 – 8, April 2000.

[102] M.L. Bortz, L.A. Eyres, and M.M. Fejer, "Depth profiling of the d_{33} nonlinear coefficient in annealed proton exchanged $LiNbO_3$ waveguides," *Applied Physics Letters*, 62(17):2012 – 14, April 1993.

[103] K. Mizuuchi, H. Ohta, K. Yamamoto, and M. Kato, "Second-harmonic generation with a high-index-clad waveguide," *Optics Letters*, 22(16):1217 – 19, August 1997.

[104] A. Galvanauskas, K.K. Wong, K. El Hadi, M. Hofer, M.E. Fermann, D. Harter, M.H. Chou, and M.M. Fejer, "Amplification in 1.2-1.7μm communication window using OPA in PPLN waveguides," *Electronics Letters*, 35(9):731 – 3, April 1999.

[105] H. Yajima, "Dielectric thin-film optical branching waveguide," *Applied Physics Letters*, 22(12):647 – 9, June 1973.

[106] W.K. Burns and A.F. Milton, "Mode conversion in planar-dielectric separating waveguides," *IEEE Journal of Quantum Electronics*, QE-11(1):32 – 9, January 1975.

[107] N. Keil, H.H. Yao, and C. Zawadzki, "(2*2) digital optical switch realised by low cost polymer waveguide technology," *Electronics Letters*, 32(16):1470 – 1, August 1996.

[108] R. Krahenbuhl, M.M. Howerton, J. Dubinger, A.S. Greenblatt, and S.T. Vohra, "Reflective digital optical switch (RDOS) for DWDM optical network applications," *IEEE Photonics Technology Letters*, 13(1):34 – 6, January 2001.

[109] Y. Silberberg, P. Perlmutter, and J.E. Baran, "Digital optical switch," *Applied Physics Letters*, 51(16):1230 – 2, October 1987.

[110] B.H. Bransden and C.J. Joachain, *Introduction to Quantum Mechanics*, Longman Scientific and Technical, Essex, England, 1992.

[111] C. Cohen-Tannoudji, B. Diu, and F. Laloe, *Quantum Mechanics*, John Wiley, New York, 1977.

[112] J.R. Kurz, A.M. Schober, D.S. Hum, A.J. Saltzman, and M.M. Fejer, "Nonlinear physical optics with transversely patterned quasi-phase-matching gratings," *IEEE Journal of Selected Topics in Quantum Electronics*, 8(3):660 – 664, May/June 2002.

[113] Y. Ishigame, T. Suhara, and H. Nishihara, "$LiNbO_3$ waveguide second-harmonic-generation device phase matched with a fan-out domain-inverted grating," *Optics Letters*, 16(6):375 – 7, March 1991.

[114] G. Imeshev, M. Proctor, and M.M. Fejer, "Lateral patterning of nonlinear frequency conversion with transversely varying quasi-phase-matching gratings," *Optics Letters*, 23(9):673 – 5, May 1998.

[115] V. Berger, "Nonlinear photonic crystals," *Physical Review Letters*, 81(19):4136 – 9, November 1998.

[116] N.G.R. Broderick, G.W. Ross, H.L. Offerhaus, D.J. Richardson, and D.C. Hanna, "Hexagonally poled lithium niobate: a two-dimensional nonlinear photonic crystal," *Physical Review Letters*, 84(19):4345 – 8, May 2000.

[117] E. Hecht, *Optics*, Addison-Wesley, Reading, Massachusetts, 1990.

[118] G.D. Boyd and D.A. Kleinman, "Parametric interaction of focused gaussian light beams," *Jour. App. Phys.*, 39(8):3597 – 3639, July 1968.

[119] Y. Furukawa, K. Kitamura, S. Takekawa, A. Alesandrovski, G. Foulon, R.K. Route, and M.M. Fejer, "Elimination of photorefraction and green-induced-infrared-absorption in MgO-doped near-stoichiometric $LiNbO_3$," *Topical Meeting on Advanced Solid-State Lasers (ASSL)*, February 2000.

[120] P. Bernasconi, G. Montemezzani, P. Gunter, Y. Furukawa, and K. Kitamura, "Stoichiometric $LiTaO_3$ for ultraviolet photorefraction," *Ferroelectrics*, 223(1-4):373 – 9, 1999.

[121] L.A. Eyres, P.J. Tourreau, T.J. Pinguet, C.B. Ebert, J.S. Harris, M.M. Fejer, L. Becouarn, B. Gerard, and E. Lallier, "All-epitaxial fabrication of thick orientation-patterned GaAs films for nonlinear optical frequency conversion," *Applied Physics Letters*, 79(7):904 – 6, August 2001.

[122] A. Chowdhury, H.M. Ng, M. Bhardwaj, and N.G. Weimann, "Second-harmonic generation in periodically poled GaN," *Applied Physics Letters*, 83(6):1077 – 9, August 2003.

[123] J. Leuthold, J. Eckner, E. Gamper, P.A. Besse, and H. Melchior, "Multimode interference couplers for the conversion and combining of zero- and first-order modes," *Journal of Lightwave Technology*, 16(7):1228 – 39, July 1998.